Universität Bonn

Physikalisches Institut

Development and Analysis of Simplified Models in the Search for Supersymmetry with Tau Leptons in the Final State at the ATLAS Experiment

Oliver Ricken

This thesis presents studies on a new approach in the search for Supersymmetry (SUSY) using Simplified Models. While regular SUSY searches look for the signature of full SUSY models, Simplified Models exploit rare event topologies with exotic kinematics that can be part of many different SUSY scenarios. Once such a Simplified Model signature has been discovered, the construction of a full SUSY model around it is possible. This thesis starts out with the development of Simplified Models motivated by the physics accessible at LHC experiments like ATLAS with a special focus on final state tau leptons. As a primary model the strong production of squark pairs decaying via charginos and stau sleptons is studied. Furthermore, as auxilliary models, the direct electroweak pair production of charginos decaying into stau sleptons and the direct electroweak production of stau slepton pairs are studied. The two auxilliary models are developed to study and evaluate the influence of so-called hidden parameters of the primary model. For the model of chargino pair production as well as for the primary model exclusion limits on the model parameters or the model's production cross sections are calculated. Finally the obtained results are interpreted in the context of the search for SUSY and proposals for future developments are discussed.

Physikalisches Institut der
Universität Bonn
Nussallee 12
D-53115 Bonn

BONN-IB-2013-03
November 2013

Universität Bonn

Physikalisches Institut

Development and Analysis of Simplified Models in the Search for Supersymmetry with Tau Leptons in the Final State at the ATLAS Experiment

Oliver Ricken

Dieser Forschungsbericht wurde als Masterarbeit von der Mathematisch-Naturwissenschaftlichen Fakultät der Universität Bonn angenommen.

Angenommen am:	27.09.2013
1. Gutachter:	Prof. Dr. Klaus Desch
2. Gutachter:	Prof. Dr. Norbert Wermes

Contents

CHAPTER 1

Introduction

In the ever ongoing search for the origin of the universe and everything in it, the discipline of particle physics investigates the microscopic end of both a universal time and length scale[1]: by performing experiments at ever higher energies the smallest spatial objects can be resolved and scenarios temporarily close to the big bang can be studied. While the study of the fundamental building blocks of matter leads to increasing comprehension of the structure of everything in the universe, the investigation of scenarios temporarily close the big bang provides insight into the origin of the universe.
A useful tool in understanding the phenomena of particle physics is the Standard Model of Particle Physics (SM). This theoretical concept has proven very reliable since its development in the 1960s for several reasons that qualify a good model: it is able to explain most observations in current particle physics, it has been able to predict observations before they were made and it has been tested to very high precision. However, the Standard Model cannot be the ultimate formula to explain the microcosmos since it only includes three of the four known fundamental forces, does not explain the experimentally confirmed observations of baryogenesis [1–3] and dark matter [2, 4]. Nevertheless, there are promising extensions to the Standard Model which could well cure its weaknesses. One of them is Supersymmetry (SUSY) – an extension which would be a prerequisite to fix the Standard Model's inability to describe, for example, dark matter (c. f. section 2.1.2), but which has not been established yet by experimental evidence.
Due to the fact that Supersymmetry has been searched for since its proposal only 10 years after the development of the Standard Model [5–13] and has not been observed yet, new approaches beyond the trodden paths of hitherto searches for SUSY are being developed. One of these approaches is motivated by simple inversion of the ansatz: instead of searching for a signal that matches a particular model, a rare signal that could match as many models as possible is looked for. Once such a signal has been observed, it can be studied in more detail and a theoretical model can be constructed around it. This is the approach pursued in this thesis – the approach of Simplified Models in the search for Supersymmetry.
Due to the structure of SUSY, heavy particles like third generation SM fermions are preferably produced in SUSY events. The signatures studied in this thesis are characterised by the presence of tau leptons. Since these heavy fermions are expected to be produced in rather high abundances in several SUSY scenarios their presence in an event can be an indicator for a SUSY signal. However, tau leptons are rather hard to detect and tend to be hard to distinguish from other signatures that look similar to them but are different. Hence, analyses involving tau leptons are both promising and challenging at the same

[1] Astro physics is the discipline covering the macroscopic ends

time.
It has already been mentioned that one goal of particle physics is accessing ever higher energies to push its boundaries beyond the current limits. To make the next step in this direction the Large Hadron Collider (LHC) has been designed and built – the worlds largest particle accelerator. The LHC provides high energy hadron-hadron collisions for a number of experiments. One of these experiments is ATLAS, a particle physics detector designed for a vast number of purposes, one of them being the search for SUSY.
Combining all of the information above the goal of this thesis is to develop and analyse promising Simplified Models for the search for Supersymmetry. This goal is pursued in several steps:

- By performing a pre-study on simulated SUSY events of an already existing SUSY search [14] and by obeying arguments of simplicity and practicability the decision for a primary Simplified Model is made.
- Additional Simplified Models being devised as sub-models or auxiliary models, respectively, to the primary Simplified Model are developed in order to study possible hidden parameters[2] of the primary model.
- An analysis strategy is developed that is able to separate a possible SUSY signature as good as possible from the (typically huge) SM backgrounds. Since the development of a perfectly tailored background suppressing event selection is too time-consuming, the selection criteria for the study of the Simplified Models in this thesis are adopted from similar ATLAS analysis [14, 15].
- Based on statistical methods the significance of the obtained results is calculated. If the results do not exceed the SM expectation a limit setting procedure is applied that derives 95% CL exclusion limits on the model parameters.
- In the case of hidden parameter studies for a particular model the influence of such parameters on the analyses is evaluated. Furthermore it is discussed to which degree the parameters are actually to be called 'hidden'.
- The obtained results are interpreted in terms of their expressiveness. Judging from this, future developments and prospects are proposed and discussed.

After all of the developed Simplified Models have been analysed and their results interpreted, a summarising overview is provided and conclusions regarding future developments are briefly drawn.

[2] This thesis distinguishes between parameters that actually define a Simplified Model and so-called 'hidden' parameters which are not part of the parameter space defining the model frame but can influence the analysis. Only parameters that do not influence an analysis are truly hidden.

CHAPTER 2

The Standard Model and its Supersymmetric Extensions

2.1 The Standard Model of Elementary Particle Physics

The Standard Model of elementary particle physics (SM) is a theoretical concept which is able to describe the fundamental constituents of matter and their interactions. Since its development in the 1960s [16–18] it has been able to predict several discoveries before they were actually made (e. g. the existence of gluons, the charm and the top quark, the weak gauge bosons W and Z and the Higgs boson). This and the fact that the Standard Model has been tested to a great extend without measuring significant deviations make it an attractive theory of elementary particle physics.

2.1.1 The Standard Model in a Nutshell

The way the Standard Model describes nature is quantum field theory. While matter is described by fermion fields, interactions are mediated by vector bosons. The masses of the fundamental particles are a result of the Higgs mechanism [19].
The fundamental fermions can be subdivided into leptons and quarks. For the leptons one distinguishes charged leptons (e, μ, τ) carrying an electromagnetic charge of (-1) and neutral neutrinos (ν_e, ν_μ, ν_τ). The quarks can be divided into up-type quarks carrying an electromagnetic charge of $+2/3$ and down-type quarks (electromagnetic charge $-1/3$). Besides this, all quarks carry colour charge which enables them to interact strongly. Furthermore all fermions interact weakly while only the electromagnetically charged ones interact electromagnetically (leptons are 'colourless' and thus do not couple to the strong force).
The fundamental fermions can be arranged in three families or generations, respectively. Each generation consists of a charged/neutral doublet of leptons (e. g. (e, ν_e)) and an up-type/down-type quark doublet (e. g. (u, d)). The generations are labelled such that with increasing index the physical masses of the particles contained rise. The overall mass scale of the SM fundamental fermions ranges from 511 keV[1] for the electron to 173 GeV for the top quark [20]. A graphical overview of the fundamental

[1] Within this thesis so-called 'natural units' are used to measure observables of particle physics. In the system of natural units the relation $\hbar = 1 = c$ holds which implies that masses and momenta are no longer given in units of E/c^2 and E/c, respectively, but that both quantities are measured in units of energy.

particles and their ordering in the SM is depicted in fig. 2.1. An illustration of the corresponding antiparticles[2] is not displayed.

The SM bosons are mediators of the three forces which the SM is able to describe: the electromag-

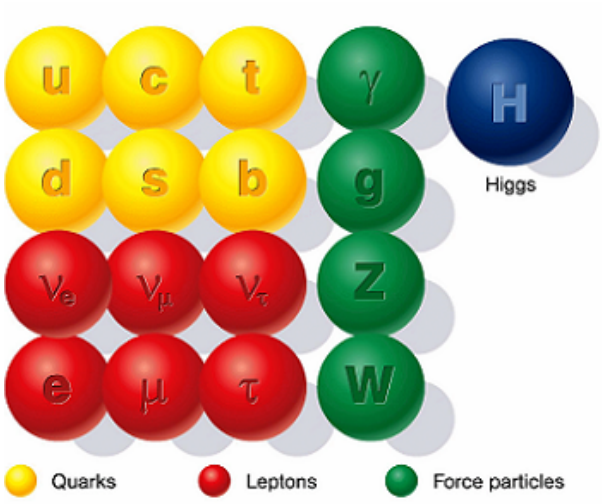

Figure 2.1: Schematic of the Standard Model of elementary particle physics, taken from http://www.coepp.org.au/files/coepp/images/susyparticles_sm.png

netic, the weak and the strong force – the gravitational force is not described by the SM. The photon of the electromagnetic and the gluons of the strong interaction are massless while the weak gauge bosons $W^{\pm}, Z^0$ are massive. An explanation for this fact as well as for the unification of the electromagnetic force and the weak force at a certain energy scale—namely the phenomenon of electroweak symmetry breaking—can be found in [18].

The basis of the SM is a relativistic quantum field theory formulated within a Lagrangian formalism [19]. Its fundamental concept is the consideration of different symmetries and its invariance under local gauge transformation. The latter can be achieved by including gauge fields into the Lagrangian energy density (abbreviated by 'Lagrangian'). The field quanta of these gauge fields are the gauge bosons of which a total of twelve exist in the SM (eight gluons and one photon, $W^{\pm}$, Z^0, respectively). From a group theory point of view the SM can be described with a $U(1)_Y \times SU(2)_L \times SU(3)_C$ symmetry group. The $U(1)_Y \times SU(2)_L$ symmetry describes the electroweak interaction. Below a certain energy scale it is broken into the symmetry groups $U(1)_{\text{e.m.}}$ and $SU(2)_{\text{weak}}$. The $U(1)_{\text{e.m.}}$ group describes quantum electrodynamics [21, 22]. Its only gauge field is the electromagnetic field mediate by its field quantum, the photon. The $SU(2)_{\text{weak}}$ group describes the weak interaction [16, 23] via three gauge bosons, $W^{\pm}$ and Z^0. The strong interaction is governed by the $SU(3)_C$ group and its eight gauge bosons, the gluons.

2.1.2 Unresolved Issues of the Standard Model

Although the SM has proven to be a reliable source of predictions, there are observations which it does not explain and topics not covered by it. Some of these issues are mentioned below:

[2] Arising from quantum field theory, antiparticles are 'mirror images' of the corresponding particles: their additive quantum numbers (e. g. electric charge, lepton number, etc.) have inverted sign with respect to the particles while their non-additive quantum numbers (e. g. mass, spin and lifetime) are identical. From a field theoretical point of view antiparticles are the CP-conjugate of particles. When all additive quantum numbers of a particle are zero it is its own antiparticle (e. g. π^0, γ or Z^0).

The hierarchy problem is an unresolved issue of the Higgs mechanism of the SM which gives mass to the fundamental particles of the SM. The mass of the physical field quantum of the Higgs field, the Higgs boson, receives large corrections from virtual effects of every particle coupling (directly or indirectly) to the Higgs field [24–27]. A Dirac fermion f coupling to the Higgs field would yield a correction to the Higgs boson mass of

$$\Delta m_H^2 = -\frac{\left|\lambda_f\right|^2}{8\pi^2}\Lambda_{\mathrm{UV}}^2 + \ldots, \tag{2.1}$$

where λ_f denotes the coupling constant of the fermion to the field and Λ_{UV} denotes the ultraviolet momentum cutoff [28] which is needed to regulate the loop integral and which provides the energy scale at which new physics beyond the SM enters [19].
A possible solution to this so-called hierarchy problem is the existence of a heavy complex scalar particle S with mass m_S coupling to the Higgs field with a Lagrangian contribution of $-\lambda_S |H|^2 |S|^2$ (H denotes the Higgs field, S the field of the new particle and λ_S its coupling strength to the Higgs field). This would lead to a new correction of the Higgs boson mass [28]:

$$\Delta m_H^2 = \frac{|\lambda_S|^2}{16\pi^2}\left[\Lambda_{\mathrm{UV}}^2 - 2m_S^2 \ln\left(\Lambda_{\mathrm{UV}}/m_S\right) + \ldots\right]. \tag{2.2}$$

In this form the contribution from Λ_{UV}^2 would cancel completely if each SM fermion (leptons and quarks alike) would be accompanied by a pair of complex scalar particles with the same mass and $\lambda_S = |\lambda_f|^2$ [28]. Further problems arising from higher order terms neglected in these formulae would also be solved by introducing such new particles [29–34].
Dark matter is a topic not covered by the SM but part of the well established model of cosmology [35] and supported by observations[3]. This model states a composition of the known universe of 4.4% baryonic matter, 22% dark matter and 73% dark energy. The SM is only able to describe the rather small part of baryonic matter. Since dark matter does not interact electromagnetically but only gravitationally it can only be detected indirectly by observing its gravitational effects in the universe [19]. Dark energy is a concept introduced to explain the accelerated expansion of the universe. Some supersymmetric extensions of the SM introduce dark matter to the model and thus are able to enhance the prediction power of the SM enormously [37, 38].
The unification of forces in a so-called Grand Unified Theory (GUT) is an aim pursued to reduce the number of parameters of the SM. Up to now with only the electroweak unification, the SM has 19 free parameters: the masses of the nine charged fermions [20], the three mixing angles and the CP-violating phase of the Cabibbo-Kobayashi-Maskawa matrix[4] [39, 40], the three gauge couplings of the three symmetry groups, the vacuum angle of quantum chromo dynamics (QCD), the Higgs field vacuum expectation value and the Higgs boson mass. To reduce this rather large number of free parameters one could embed the SM symmetry group into another symmetry group e. g. $SU(5)$. Analogously to electroweak symmetry breaking beneath a certain energy scale, the current SM couplings would exists as usual while above this certain scale all couplings could be replaced by one single $SU(5)$ gauge coupling. As fig. 2.2 shows the SM gauge couplings (black dashed lines) fail to cross at the same energy scale whereas the desired unification can be achieved in different scenarios of SUSY (c. f. [28]).

Further unresolved issues of the SM are the asymmetry between matter and anti-matter in the universe, its lack of including gravity as a fourth force and the fact that neutrinos are considered massless

[3] A detailled overview of dark matter and searches for it is provided in [36]
[4] The CKM matrix describes the composition of the physical mass eigenstates of the Standard Model quarks of the electroweak eigenstates.

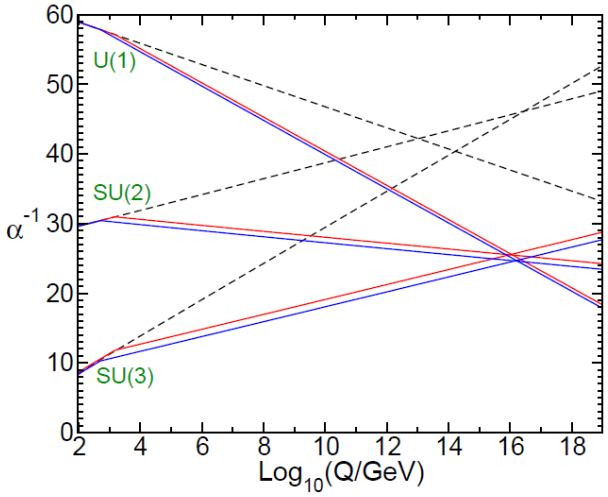

Figure 2.2: Displayed are the inverse gauge couplings of the different SM interaction labelled by their corresponding symmetry groups ($SU(3)$ for the strong force, $SU(2)$ for the weak force and $U(1)$ for the electromagnetic force) varying with the momentum transfer Q. The Standard Model couplings (black dashed lines) fail to cross all in one point while for SUSY scenarios (solid blue and red lines) a unification of forces can be achieved at a certain energy scale or momentum transfer, respectively. Further detailed information can be found in [28]. The image is taken from ibid..

whereas proof of non-vanishing neutrino masses has been furnished.

2.2 Supersymmetry – a Promising Extension of the Standard Model

Looking at the hierarchy problem described in section 2.1.2, the construction of a model with a symmetry between fermions and bosons appears to be a promising approach. This is the basic concept of Supersymmetry [5–13]. Particles related in such a way are called superpartners and are arranged in supermultiplets. Due to the supersymmetric algebra the particles in one supermultiplet have same electric charge, mass, weak isospin, and colour degrees of freedom. Furthermore the number of fermion and boson degrees of freedom has to be the same: $n_F = n_B$. As a consequence a single Weyl fermion with two helicity degrees of freedom is combined with a two real scalar particles to form a supermultiplet. In a similar way the sector of the SM gauge boson is supersymmetrised.
In contrast to the SM, gravity can be included in supersymmetric models by combining the spin-2 graviton (two helicity states, $n_B = 2$) with a spin-$^3/_2$ superpartner. In the case of unbroken symmetry the superpartner—the so-called gravitino—is massless hence having two helicity states ($n_F = 2$).
If SUSY was an exact symmetry, the superparticles would have the same masses as their SM partners and thus SUSY would have been discovered by now. Since this is not the case SUSY has to be a broken symmetry. In order to still fix the hierarchy problem of the SM the Lagrangian contribution of Supersymmetry is split into two parts one of them being a 'soft' symmetry breaking term:

$$\mathcal{L} = \mathcal{L}_{\mathrm{SUSY}} + \mathcal{L}_{\mathrm{soft}}. \tag{2.3}$$

The first part of eq. (2.3) contains all gauge and Yukawa couplings and preserves supersymmetry invariance while the second part violates SUSY but contains only terms with positive mass dimension hence fixing the hierarchy problem [19].

With the basic idea of (broken) Supersymmetry being an extension to the Standard Model of particle physics outlined, the following section introduces the Minimal Supersymmetric Standard Model (MSSM) and briefly describes an additional constrained model of SUSY.

2.2.1 Models of Supersymmetry

All the considerations regarding supersymmetry in the section above can be used to construct supersymmetric models. The model considered in the framewrok of this thesis is the so-called Minimal Supersymmetric Standard Model (MSSM) [29, 41–46].
Since the full MSSM is described by approximately 120 parameters (regard the 19 parameters of the Standard Model!) several constrained models have been developed of which one is briefly introduced afterwards.

The Minimal Supersymmetric Standard Model – MSSM

As its name already suggests, the basic idea of the MSSM is to supersymmetrise the SM in a minimal way. This process begins by considering the SM being a theory of chirality: the particle eigentstates relevant for the interactions are chirality eigenstates while the physical mass eigenstates are superpositions of different chirality eigenstates. Adopting this principle the superpartners of the SM particles in the MSSM are arranged in chirality supermultiplets. For each SM fermion a doublet of left- and right-chiral sfermions (scalar particles!) is introduced. For the tau lepton, for example, a left- and right-chrial stau sparticle $\tilde{\tau}_{\mathrm{L}}$, $\tilde{\tau}_{\mathrm{R}}$, respectively, is introduced. While the superpartners of the SM leptons are called sleptons the superpartners of quarks are called squarks.
The gauge interactions of the sparticles are identical to those of the corresponding SM particles i. e. only left-handed spaticles couple to the W- boson etc. [19].
The theory of supersymmetry requires the SM scalar Higgs boson to be resided into two Higgs supermultiplets in order to avoid a gauge anomaly [19]. These two Higgs doublets differ in their electroweak hypercharge Y. One doublet ($Y = 1/2$) gives mass to the up-type quarks (referred to as H_u) while the other one ($Y = -1/2$, H_d) gives mass to the down-type quarks and charged leptons. Both doublets consist of a charged and a neutral weak isospin component. The existence of two neutral Higgs fields introduces two vacuum expectation values (VEV) and their ratio $\tan\beta$:

$$v_u = \langle H_u^0 \rangle \tag{2.4}$$

$$v_d = \langle H_d^0 \rangle \tag{2.5}$$

$$\tan\beta \equiv \frac{v_u}{v_d}. \tag{2.6}$$

The gauge boson sector of the SM is supersymmetrised by transforming the spin-1 gauge bosons (W^+, W^0, W^-, B^0) into spin-1/2 gauginos ($\tilde{W}^+, \tilde{W}^0, \tilde{W}^-, \tilde{B}^0$).
The full particle content of the MSSM is summarised in table 2.1.
Implementing the most general gauge-invariant renormalisable superpotential into the Lagrangian yields terms which either violate the baryon number (B) or the lepton number (L). Since both of these quantities are conserved within the SM and neither L- nor B-violation has been observed in nature yet[5], a new

[5] the search for B-violating processes includes the measurement of the proton lifetime; so far, no proton decay has been measured yielding a lower limit of the proton mean lifetime of $21. \times 10^{28}$ years [20]

symmetry is introduced to cancel out the L- and B-violating terms: R-parity:

$$P_R = (-1)^{3B+L+2s}. \tag{2.7}$$

In this notation s denotes the particle's spin. R-parity is defined as a multiplicative conserved quantum number [19]. Putting in the corresponding quantum numbers, SM particles and the Higgs bosons take $P_R = +1$ while all SUSY particles alike take $P_R = -1$. With R-parity being conserved no mixing of SM and SUSY particles is allowed while only even numbers of SUSY sparticles are allowed to interact at one vertex. The latter requirement yields some important implications:

- The lightest SUSY particle (LSP) must be stable. Since it is expected to only interact weakly with regular matter the LSP is a candidate for dark matter and is only detectable in experiments via missing energy.
- Every sparticle heavier than the LSP must decay via a cascade down to the LSP. Such a decay cascade usually produces a SM particle at each vertex hence leaving many SM particles to be detected in the search for SUSY signatures.
- Collider experiments can produce sparticles only in pairs yielding two LSPs to escape the detector.

As already mentioned in the introductory part of section 2.2 the physical mass eigenstates of the sfermions are superpositions of the chirality eigenstates. The amount of mixing of the chirality eigenstates into the mass eigenstates is proportional to the Yukawa coupling of the particle and $\tan\beta$ and hence proportional to the mass of the corresponding SM superpartner. As a consequence the first and second generation squarks and sleptons are degenerate in mass leaving them to be classified as the chirality eigenstates. However, the third generation squarks and the stau slepton show significant mixing resulting in two different mass eigenstates labelled $\tilde{\tau}_1$ and $\tilde{\tau}_2$ for the stau sparitcle, respectively, with the subscript 1 indicating the lighter eigenstate and the subscript 2 indicating the heavier one.
Similar effects occur for the chargino and neutralino mass eigenstates which mix from the gauge eigenstates. The gluino cannot mix with other MSSM sparticles. Much more detailed information summarised in a neat overview can be found in [28].
Having introduced only a small part of the MSSM concept the complexity of it can be inferred. The full MSSM model can be described by a set of approximately 120 parameters making it a hard to test model. Imposing several constraints on the MSSM and making some realistic assumptions, several simpler but constrained models can be constructed. One of them is called GMSB – gauge-mediated supersymmetry breaking. A brief introduction to the GMSB model is the subject of the next section.

Gauge-mediated Supersymmetry Breaking – GMSB

As already mentioned SUSY has to be a broken symmetry which means that a breaking mechanism must exist. Due to the structure of the MSSM theory the process of symmetry breaking has to happen in a hidden sector which does not have direct couplings to the so-called visible sector of the MSSM (i. e. the MSSM soft breaking terms have to arise indirectly or radiatively [19]). One out of several breaking mechanisms is the so-called 'gauge-mediated supersymmetry breaking' (GMSB). In this SUSY breaking scenario the breaking is mediated from the hidden to the visible sector by messenger particles which interact with the particles from the visible sector in loops via the ordinary gauge interactions (i. e. electroweakly and strongly).
This breaking scenario requires the existence of a massless Weyl fermion, the so-called goldstino. In order to include gravitation into the model the spin-2 graviton from the SM gets a spin-$^3/_2$ superpartner,

Name	Spin	P_R	Gauge eigenstate	Mass eigenstate
Higgs bosons	0	+1	$H_u^0, H_d^0, H_u^+, H_d^-$	$h^0, H^0, A^0, H^\pm$
Squarks	0	-1	$\tilde{u}_L, \tilde{u}_R, \tilde{d}_L, \tilde{d}_R$	(same)
	0	-1	$\tilde{c}_L, \tilde{c}_R, \tilde{s}_L, \tilde{s}_R$	(same)
	0	-1	$\tilde{t}_L, \tilde{t}_R, \tilde{b}_L, \tilde{b}_R$	$\tilde{t}_1, \tilde{t}_2, \tilde{b}_1, \tilde{b}_2$
Sleptons	0	-1	$\tilde{e}_L, \tilde{e}_R, \tilde{\nu}_e$	(same)
	0	-1	$\tilde{\mu}_L, \tilde{\mu}_R, \tilde{\nu}_\mu$	(same)
	0	-1	$\tilde{\tau}_L, \tilde{\tau}_R, \tilde{\nu}_\tau$	$\tilde{\tau}_1, \tilde{\tau}_2, \tilde{\nu}_\tau$
Neutralinos	1/2	-1	$\tilde{B}^0, \tilde{W}^0, \tilde{H}_u^0, \tilde{H}_d^0$	$\tilde{\chi}_1^0, \tilde{\chi}_2^0, \tilde{\chi}_3^0, \tilde{\chi}_4^0$
Charginos	1/2	-1	$\tilde{W}^\pm, \tilde{H}_u^+, \tilde{H}_d^-$	$\tilde{\chi}_1^\pm, \tilde{\chi}_2^\pm$
Gluino	1/2	-1	$\tilde{g}$	(same)
Goldstino (Gravitino)	1/2 (3/2)	-1	$\tilde{G}$	(same)

Table 2.1: The particle content of the MSSM. The table displays all properties of sparticles contained in the MSSM distinguishing between mass and gauge eigenstates if necessary [28].

the gravitino, which both are massless as long as SUSY is unbroken. After the process of spontaneous symmetry breaking the gravitino absorbs the goldstino and hence accquires mass which also induces longitudinal helicity states to the gravitino. Due to the model structure of GMSB the gravitino is much lighter than all other sparticles ($O(m(\tilde{G})) = 1\,\text{keV}$) which yields the gravitino being the LSP [19]. Furthermore this facts leads to the relation that only the next-to-lightest sparticle (NLSP) can decay into the LSP. This again results in the experimental signature of the GMSB being dominated by the presence of the SM partners of the NLSP.
The MSSM with the GMSB mechanism can be described by a total of only six parameters: the SUSY breaking scale Λ which is typically of the order of 10 TeV to 100 TeV, the mass of the messenger sparticle $M_{\text{mes.}}$, the number of messenger fields in the symmetry group $SU(5)$ of GMSB N_5, the ratio of the VEVs $\tan\beta$, the sign of the Higgsino mass term $\text{sgn}(\mu)$ appearing in the gaugino sector of the MSSM and fiannly the scale factor of the Goldstino coupling $C_{\text{grav.}}$ which determines the NSLP lifetime [19]. Further additional and more detailed information on the MSSM, its different breaking scenarios and GMSB in particular can be found in [28].
In order to get a feeling for the sparticle masses which are to be expected in GMSB, an exemplary mass spectrum is depicted in fig. 2.3. Typical for GMSB are the high masses of the strongly interacting sparticles with respect to those of the gauginos and sleptons often leaving the stau to be the LSP.

2.2.2 Simplified Models of Supersymmetry

The last sections have outlined how prosperous of an extension to the Standard Model Supersymmetry is. However, the 120 parameters of the MSSM make it very elaborate to design physics that can be searched for at an experiment which is why this approach is not pursued in the search for SUSY.
The approach chosen in most SUSY searches at the ATLAS experiment is to look for the signature of a particular constrained model like GMSB. In these searches the supersymmetric physics processes are simulated for different sets of the model parameters (e. g. fixing all parameters but Λ and $\tan\beta$). Since only a finite amount of parameter sets can be produced, the spacing between adjacent points in

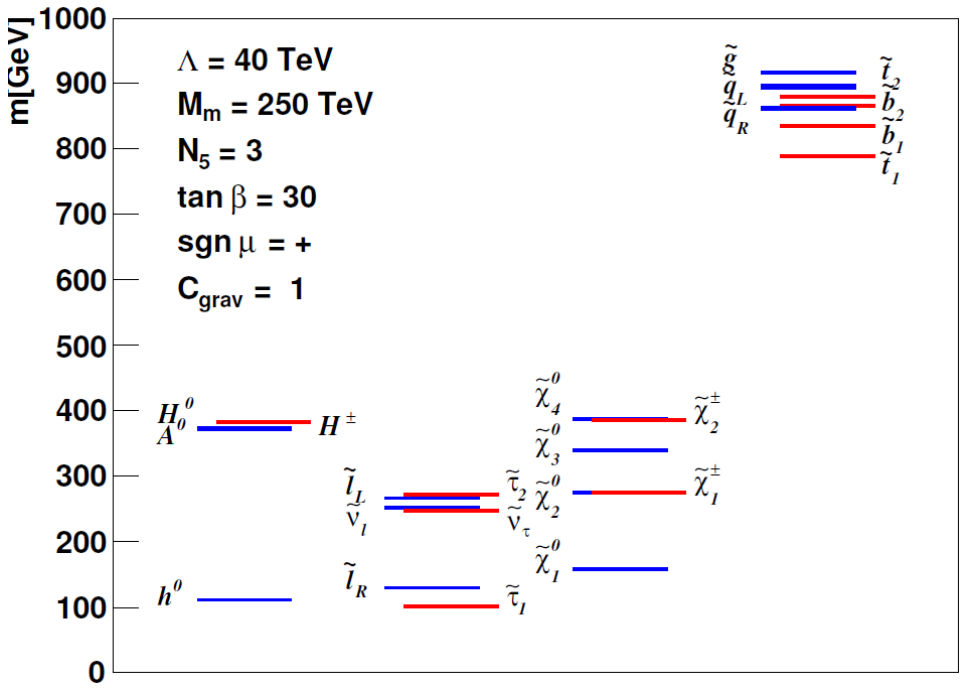

Figure 2.3: An exemplary mass spectrum for a GMSB SUSY model with parameters $\Lambda = 40\,\text{TeV}$ and $\tan\beta = 30$. Clearly visible are the strongly interacting sparticles at the upper end of the spectrum while the stau is the NSLP. The very light gravitino LSP is not displayed [47].

parameter space is finite defining a so-called grid structure (e. g. spanned up by Λ and $\tan\beta$) referred to as grid.
Searching for SUSY with this technique comes with several advantages and drawbacks at the same time:

- **Pro**: By searching for a full model like GMSB exclusions of the theoretical model parameters can be made. This provides large exclusion power for one particular model.
- **Con**: By searching for just one particular model only this model can be (partly) excluded. A search like this cannot make any statement on other models. This point is crucial since there is no evidence for any particular SUSY breaking scenario that is realised in nature – all SUSY scenarios are equally likely or unlikely to be realised.
- **Pro**: By parametrising the model with theory parameters all aspects of the model like branching fractions, decay widths, coupling strengths, etc. are covered.

The key question in this context is 'Why should there be any distinguished SUSY scenario?'. Another approach in the search for Supersymmetry is aiming towards a model-independent search: the search with Simplified Models.
The basic idea of searching for SUSY with so-called Simplified Models is to not look for a particular SUSY scenario but to look for SUSY signatures that can be produced by (almost) every underlying scenario. This approach is motivated by the flexibility it offers: by not setting limits on the parameters of one particular scenario but on pseudo-observables like sparticle masses, the results of a Simplified Model study can be used to set limits on any SUSY scenario containing the studied physics signature. This approach can be particularly interesting for theorists developing new SUSY scenarios who want to

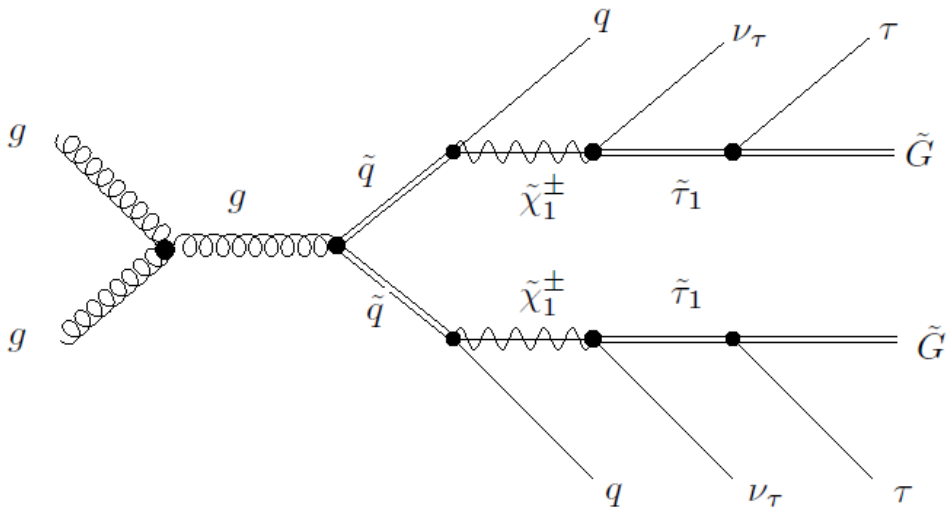

Figure 2.4: Event topology of an exemplary Simplified Model. Every sparticle can only decay into a designated set of daughter particles fixing the overall event topology to the one displayed. A Simplified Model like this could be parametrised by the masses of the involved sparticles yielding a four-dimensional parameter space.

test their specific model – given that it involves the studied signature.
In contrast to the full model searches the parameter grids in searches with Simplified Models are not spanned up by theory parameters but by pseudo-observables such as sparticle masses. Furthermore most Simplified Models consist of one supersymmetric topology only fixing all branching ratios of the involved particles and their decay widths. The whole design of a Simplified Model and its differences with respect to a regular model can be illustrated by an exemplary event topology as depicted in fig. 2.4.
In this simplified model only squarks are produced in the primary interaction – in this example via an *s*-channel diagram. The squarks then always decay via a charged gaugino into another quark of different charge leaving one SM quark to be detected. The chargino then decays into the NLSP and the corresponding SM particle that is required to conserve charge and baryon/lepton number – in this case a stau and a tau neutrino. Finally the stau NLSP decays into the LSP,a gravitino in this case, and its Standard Model partner the tau lepton.
While a supersymmetric decay chain like this could emerge from several SUSY scenarios the physics of this model is constrained to exactly this process. In contrast to a regular SUSY model where the branching ratios would depend on the theory parameters all of them are fixed to 1 for the decay displayed above. The model could be well parametrised by the masses of the four sparticles involved yielding a four-dimensional parameter space to span up a grid. However, there are aspects which are not covered by such a parametrisation e. g. the amount of *s*- and *t*-channel contribution to the production process or the chirality content of the $\tilde{\tau}_1$ mass eigenstate which mixes from the chirality doublet $(\tilde{\tau}_L, \tilde{\tau}_R)$. While such aspects are intrinsically covered by full model studies due to their dependence on the theory parameters, they are so-called 'hidden parameters' in the case of a Simplified Model.
While Simplified Model studies aiming towards the setting of limits on pseudo-observables are no novelty within the ATLAS collaboration, the investigation of the influence of hidden parameters on the analyses is a novelty that is pursued for the first time in this thesis.
The idea of Simplified Model searches for SUSY can be summed up:

- **Pro**: Simplified Models provide model-independent exclusion limits on pseudo-observables which can be interpreted and used in easy ways.

- **Con**: The exclusion power of Simplified Models is limited to the pseudo-observables used to parametrise the model under the made assumptions (e. g. the choice of fixed branching ratios). Furthermore exclusion limits on theory parameters cannot be directly inferred from the limits on pseudo-observables.

Overall, the approach for searching for SUSY by using Simplified Models is not the key to find SUSY. However, since no glimpse of SUSY has been caught yet searching for SUSY-like topologies appears to be a promising approach to find something. Once a sign of SUSY has been seen the detailed studies of which breaking scenario is realised and how the model parameters look like can be performed. But first something SUSY-like has to be observed which is why Simplified Models are a prosperous new approach.

CHAPTER 3

The ATLAS Experiment at the LHC

ATLAS—an acronym for *A Toroidal LHC Apparatus*—refers to both the particle detector and the scientific collaboration working at it. In the following sections an introduction to the experimental setup of the ATLAS detector [48] and the LHC [49] is provided. This will be restricted to the aspects needed to understand the technical features of the analyses presented in this thesis.

3.1 The Large Hadron Collider

The Large Hadron Collider (LHC) is the world's largest (27 km in circumference, source) and—regarding the collision energy it provides—the most powerful particle accelerator. It is housed approximately 100 m underground the Swiss-French border in the tunnel of its predecessor LEP (Large Electron Positron Collider) and maintained by CERN, the European Organisation for Nucelar Research. The LHC can accelerate protons as well as lead ions and collide them at the locations of the four major experiments (c. f. fig. 3.1). From 2010 to 2011 it was operated at a beam energy of 3.5 TeV while in 2012 the beams had energies of 4 TeV each. After a period of upgrade and maintenance works from 2013 to 2015 it will start up again and run at its design energy of 7 TeV per beam.
Besides the ATLAS experiment the LHC provides particle collisions for a number of other experiments such as CMS, LHCb or ALICE. While ATLAS's sister experiment CMS is a multi-purpose detector like ATLAS, LHCb and ALICE aim towards more specialised fields of science i. e. physics of B-Mesons (LHCb) and nuclear physics (ALICE). Figure 3.1 displays the overall layout of the LHC, its infrastructure and the experiments mentioned. In order to observe the rare events containing physics beyond the Standard Model a high production rate of particle collisions is needed. The rate at which particular events are produced by an accelerator such as the LHC is given by

$$N_{\text{event}} = \mathcal{L} \cdot \sigma_{\text{event}}. \tag{3.1}$$

Here σ_{event} is the production cross section of the particular event which can both me measured and calculated from theory. $\mathcal{L}$ is the luminosity of the accelerator which depends on beam parameters only:

$$\mathcal{L} = \frac{N_{\text{b}}^2 n_{\text{B}} f_{\text{rev}} \gamma_{\text{r}}}{4\pi \epsilon_{\text{n}} \beta^*} \cdot F. \tag{3.2}$$

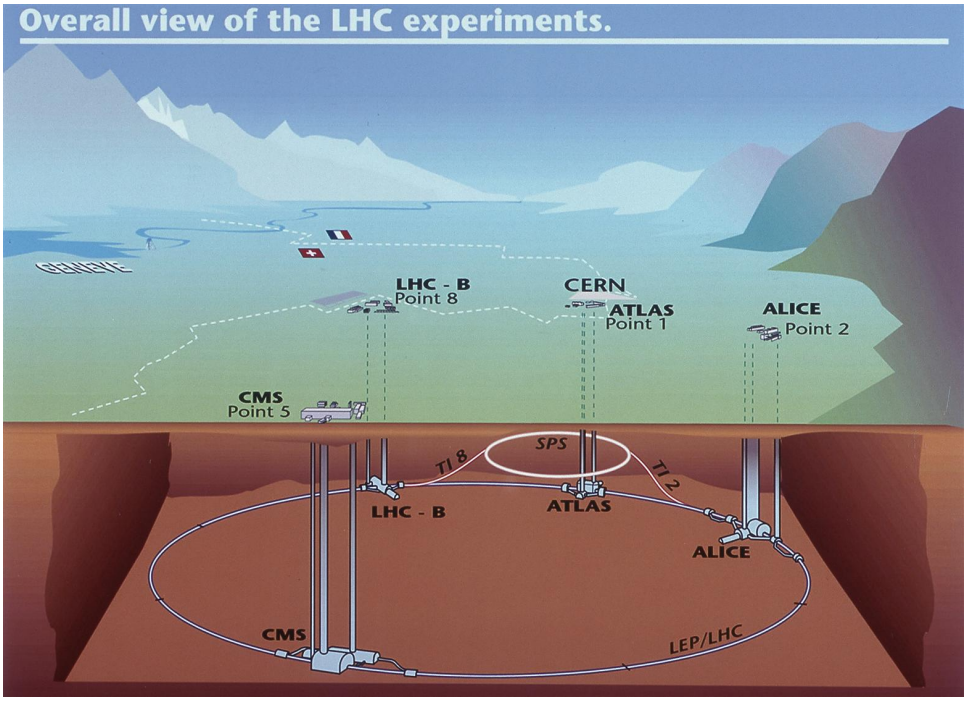

Figure 3.1: Sketch of the LHC ring, the position of the experiments and the surrounding countryside. The four major LHC experiments are indicated. The location of the injection lines and the pre-accelerator SPS are shown as well. Picture taken from [50], ATLAS Experiment ©2013 CERN

In this notation N_b^2 denotes the number of particles per bunch, n_B the number of bunches per beam, f_{rev} the revolution frequency, γ_r the relativistic gamma factor, ϵ_n the normalised transverse beam emittance, β^* the beta function of the collision point and F the geometric luminosity reduction factor due to the angle of the beam crossing at the interaction point [19].

3.1.1 Pile-up

A phenomenon arising at particle accelerators like the LHC is known as pile-up. Due to the fact that not single particles but bunches of particles are accelerated and collided at the LHC it is possible that more than one designated interaction can occur during one collision or one bunch crossing, respectively. This phenomenon is known as pile-up and such events are referred to as pile-up events. Usually pile-up is a problem to the experiment and the analyses performed due to pile-up events contaminating the signature of the interesting primary event. Since pile-up depends on the same beam parameters as luminosity it strongly scales with the latter and thus becomes a more and more severe problem the higher the luminosity of an accelerator gets.
Figure 3.2 illustrates the behaviour of pile-up, in terms of the average number of interactions per beam crossing, for the three data taking periods of the ATLAS experiment (c. f. section 3.2.5). To be considered is the increase of pile-up from 2010 to 2011 due to an increase in the accelerator's luminosity and from 2011 to 2012 due to both, an increase in the LHC's luminosity and centre-of-mass energy.

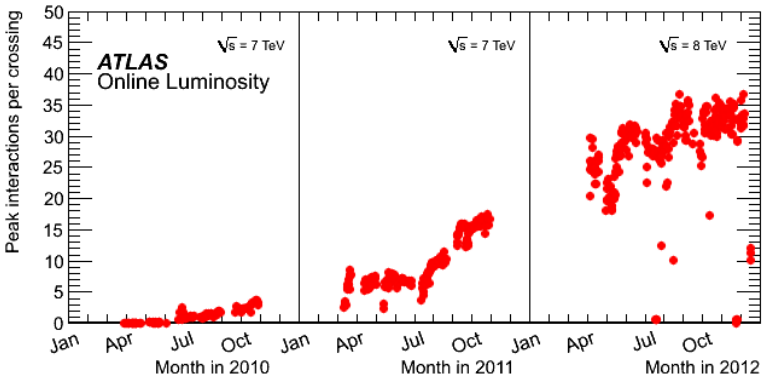

Figure 3.2: The maximum mean number of events per beam crossing versus day during the p-p runs of 2010,2011 and 2012. This version shows the average value for all bunch crossings in a lumi-block. Image taken from https://twiki.cern.ch/twiki/bin/view/AtlasPublic/LuminosityPublicResults#Publications_and_Conference_Resu.

3.2 The ATLAS Experiment

The ATLAS experiment is, besides CMS, one of the two multi-purpose experiments at the LHC. It is designed to enable the search for very different topics of particle physics. The topic relevant for this thesis is the search for Supersymmetry. Since each of these aspects requires the detector to support different technical features ATLAS's design is rather complex. Subsequently the most relevant detector features for SUSY searches are presented: As many other scenarios of BSM physics SUSY predicts large amounts of missing transverse energy. This can be measured best by a calorimeter system with large η-ϕ coverage. Furthermore several SUSY scenarios contain τ-leptons in larger abundances. To identify τ-leptons several requirements have to be met. A good overall calorimeter system with high jet resolution is also required to distinguish hadronically decaying tau leptons from jets. In order to separate τ-leptons from prompt light leptons (leptonic τ decay to e or μ) both a good electromagnetic calorimeter (electron and photon identification) and a system to resolve secondary vertices are required. In addition to those features an efficient trigger system with high background suppression is needed to filter out interesting events.

Due to its geometry the description of ATLAS and the events it records is easier when using a special coordinate system. Starting from cylindrical coordinates with the z-axis being the beam axis and the origin lying in the interaction point, the ATLAS coordinate system can be defined: the azimuthal angle ϕ is defined around the z-axis covering a range from $[-\pi \dots \pi]$. Instead of using the z-coordinate one uses the polar angle θ measured from the beam axis and transforms it to the pseudo-rapidity $\eta = -\ln\left(\tan\frac{\theta}{2}\right)$. With these parameters defined the distance between two objects in the η-ϕ-plane can be computed via $\Delta R = \sqrt{\Delta\eta^2 + \Delta\phi^2}$. Furthermore kinematic observables like a particle's momentum are measured as transverse observables e. g. $p_{\mathrm{T}} = \sqrt{p_x^2 + p_y^2}$.

To enable the measurement of a charged particle's momentum and the determination of its charge sign a magnet system is installed inside the detector. As a charged particle's trajectory is bent when being exposed to a magnetic field, one can compute the particle transverse momentum by measuring its trajectory's curvature. This yields the following approximation [48]:

$$p_{\mathrm{T}}[\mathrm{GeV}] \approx 0.3 \cdot B[\mathrm{T}] \cdot R[\mathrm{m}]. \tag{3.3}$$

Here B denotes the applied magnetic field measured in Tesla and R the radius of curvature measured in metres. The magnetic system of the ATLAS detector consists of four parts: one solenoid and one toroid in the barrel and two toroids in the endcaps[1]. The solenoid which is built into the calorimeter system provides an axial magnetic field of 2 T bending tracks of charged particles in ϕ-direction. The barrel toroid delivers a 0.5 T field while the endcap toroids yield fields of 1.5 T. Both toroid systems are designed to bend muon tracks in η-direction.
The following sections describe the different parts of the detector going from the inside to the outside.

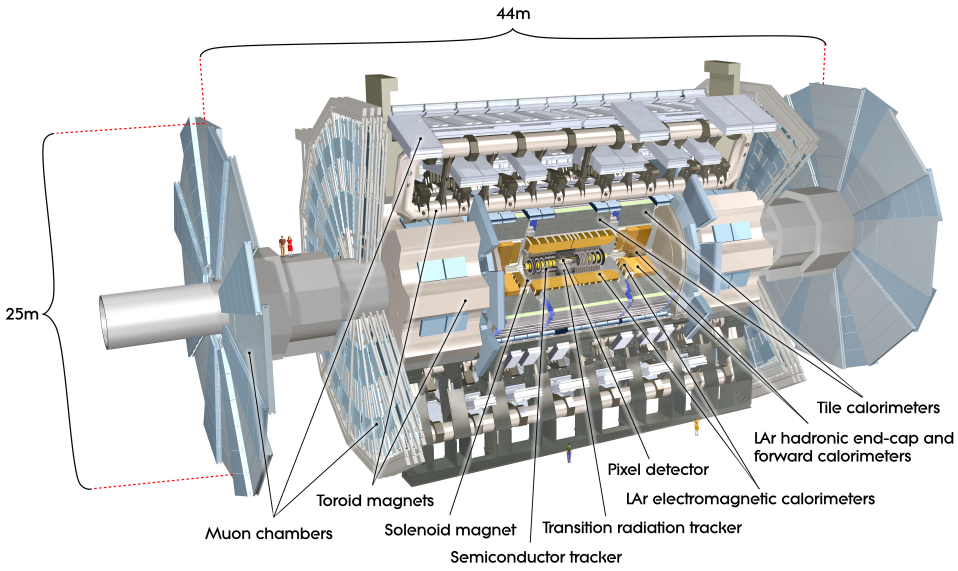

Figure 3.3: Sketch of the full ATLAS detector showing its different components. Picture taken from [50], ATLAS Experiment ©2013 CERN

3.2.1 The Inner Detector

The innermost subsystem of the ATLAS detector is the inner detector (ID) which directly encases the beam pipe around the interaction point. It is supposed to reconstruct the tracks of charged particles, measure their transverse momentum (c. f. eq. (3.3)) and determine the sign of their charge. In addition it is possible to resolve secondary vertices from the decays of long-lived particles such as τ-leptons with the ID.
To supply a large enough number of space points for the desired resolution of track reconstruction high granularity of the detector elements is required. In order to achieve this the ID is divided into three sub-components each structured such that its granularity-to-covered-surface ratio meets the desired requirements (c. f. [48]).
The innermost part of the ID is the pixel detector. It consists of three layers of semiconducting pixel sensors and is located close to the beam axis (50.5 mm for the first layer [48]). In the ideal case it provides information on three traversed pixels for a passing charged particle with a resolution of 10 µm in the R-ϕ-plane both in the barrel and the end cap region [48]. The high granularity of the pixel detector

[1] For reasons of constructability the detector is divided into a so-called barrel part which encases the beam pipe around the interaction point and two endcap parts installed at the upper and lower end of the detector z-axis

(layer thickness 1% of the radiation length [48]) requires a large number of readout channels. With 80.4 million readout channels the pixel detector takes up ≈ 90% of the all readout channels of the ATLAS detector [48].
The next-to-innermost layer of the ID is the semiconductor tracker (SCT). It consists of eight strip layers and is structured in a coarser way than the pixel detector. Its accuracy in the barrel region is 17 µm in the R-ϕ-plane while two adjacent tracks can be separated as long as their spacing is larger than 200 µm [48].
The third and outermost layer of the ID is the transition radiation tracker (TRT). It is a drift chamber made out of approximately 370000 gas-filled straw tubes. The TRT provides information on tracks of charged particles in the R-ϕ-plane with a spatial resolution of 130 µm per straw [48]. In addition to working as a drift chamber the TRT also gathers information via detection of transition radiation which is used to identify particles e. g. distinguish electrons from charged pions. Transition radiation is caused by particles crossing boundaries between materials with different permittivities (realised through interleaved polymeric fibres and foils inside the TRT) and leads to signals characteristic for every particle.

3.2.2 The Calorimeter System

The next large sub-component of the onion-like ATLAS layout is the calorimeter system. While the inner detector is primarily designed to reconstruct tracks of charged particles and thus absorb as little of a particle's energy as possible the calorimeter system's main task is a different one. It is supposed to fully stop both charged and neutral particles and thereby measure their energy. As a consequence the calorimeter system is much more bulky than the inner detector and several radiation lengths thick. In case of the ATLAS detector the calorimeter system is designed as a sampling calorimeter which means it consists of different layers of active and passive absorber material. The dense passive parts causes traversing particles to create characteristic showers which can help to identify the specific particle. In contrast to this the active calorimeter parts measure the amount of energy deposited by a particle. To detect both electromagnetically and hadronically interacting particles the ATLAS detector contains an electromagnetic calorimeter (ECAL) followed by an hadronic calorimeter (HCAL) [19].

The Electromagnetic Calorimeter

The ATLAS ECAL is built from lead as passive absorber material and liquid argon as active material. Just like the sub-components of the ID the ECAL is separated into barrel and endcap parts to cover a range of $|\eta| < 3.2$. The whole ECAL is segmented into three layers of which the first one is very fine grained in η to distinguish photons from neutral pions but rather coarse grained in ϕ. This ability is important to separate single photons from electrons [19]. The second layer is much thicker (16 radiation lengths [48]) and equally fine grained in both η and ϕ to determine the ϕ-component of a signal. The last layer is thin again (two radiation lengths [48]). It is designed to determine the leakage into the HCAL. Both the ECAL and HCAL response can be calculated via an empiric formula determined in test beam experiments [51]:

$$\frac{\sigma(E)}{E} = \frac{a}{\sqrt{E[GeV]}} \oplus b. \tag{3.4}$$

In this notation a is a stochastic term ($a = 10\%$ for the ECAL) whereas $b = 0.17\%$ (for the ECAL) is a constant term.

The Hadronic Calorimeter

Following the ECAL the next layer of the ATLAS detector is the HCAL. It is designed to measure energy deposition of hadronically interacting particles namely jets and hadronically decaying τ-leptons. Furthermore the missing transverse energy $\not{E}_{\mathrm{T}}$—a crucial variable for SUSY searches—is calculated from both the ECAL and HCAL energy measurements which is why also in the HCAL a good η-ϕ-coverage is needed. The HCAL is again separated into different parts.
The tile calorimeter is directly encasing the barrel ECAL. It is designed as a sampling calorimeter with steel as passive absorber and scintillator tiles as active material. The light produced in the scintillators is coupled to photo multipliers which generate the read-out signal via wavelength shifting fibres. The three-dimensional structure of the tile calorimeter is defined by the fibres being grouped together to provide a cell structure.
The hadronic endcap calorimeter is installed behind the ECAL endcaps and is composed of copper as passive absorption material and liquid argon as an active medium. The latter is due to reasons of radiation exposure and corresponding hardness.
Furthermore the HCAL is extended by a forward calorimeter part in the endcap region covering the parts close to the beam axis. The forward calorimeter extensions use copper and tungsten, respectively, as a passive absorber material.
More detailed information on the calorimeter system and its performance can be found in [48].

3.2.3 The Muon System

The outermost part of the ATLAS detector is the muon system. It is designed to detect particles that interact weakly and pass the calorimeter system such das muons or BSM particles. The muon system consists of four parts which are all gaseous detectors monitored drift tubes (MDT), cathode strip chambers (CSC), resistive plate chambers (RPC) and thin-gap chambers (TGC). While the first two subsystems are for precision measurements of particles the latter two are less precise but fast in data acquisition in order to be used as part of the trigger system.
The MDTs are aluminium drift tubes filled with Ar-CO_2 which detect the position of traversing muons by the drift time of electrons to the anode wires that are produced by ionising muons. This measurement can be performed with a resolution of 80 µm per tube and about 35 µm per chamber (three to eight rubes grouped together) [52].
The forward region is covered by the CSCs. Those are multi-wire proportional chambers with cathode planes segmented into strips in orthogonal directions [19]. The used gas is an Ar-CO_2-CF_4 mixture. Track coordinates can be measured by distributions of induced charge on the cathode strip. The achieved resolution is approximately 40 µm in the bending plane and approximately 5 mm in the transverse plane.
The part of the muon system which is used as part of the ATLAS trigger system separates into two parts as well. In the barrel region the RPCs are installed. These are gaseous detectors which do not use anode wires but resistive plates with a distance of 2 mm providing an electric field of 4.9 kV mm^{-1} enabling the measurement of ionising electrons. This RPCs provide a time resolution of 1.05 ns. In the endcap region the TGCs are installed. They are similar to the CDCs multi-wire proportional chambers but with lower anode-cathode distance and different gas mixture in order to provide a better time resolution of 4 ns. Furthermore a measurement of the azimuthal coordinate of a muon track is possible by using the TGCs.

3.2.4 The Trigger System

The LHC provides particle bunches with a rate of up to 40 MHz while each bunch crossing produces approximately 25 interactions. In total this amounts to an event rate of approximately 1 GHz that has to be detected and stored by the ATLAS detector. Since the possible disc storage rate ist just about 200 Hz a fast and efficient trigger system has been designed to filter out only interesting events that are stored for further analyses.
The ATLAS trigger system is divided into three parts: the Level 1 (L1) trigger, the Level 2 (L2) trigger and the Event Filter (EF) [53, 54]. Each of these levels reduces the amount of produced data the earlier trigger stage provided. For the decision making of the L1 trigger the incoming detector signals are buffered. The L1 trigger is implemented in a fast customs electronics directly on hardware level using only a very limited amount of event information [19]. Since it runs on every bunch crossing it has 2.5 µs to decide whether to take an event or discard it thus reducing the rate to < 75 kHz.
The combination of L2 trigger and EF is known as High Level Trigger (HLT) with both elements being software based. The data provided by the L1 trigger is transferred to a computer farm where the L2 trigger performs further analyses. Using fast customs algorithms the L2 trigger has approximately 40 ms for making a decision which reduces the event rate to < 3.5 kHz.
When an event passes the L2 trigger it is fully reconstructed to provide information for the Event Filter. The EF then takes approximately 4 s to make a decision reducing the overall event rate to $\approx$ 200 Hz. Examples for EF-level triggers which are used in the analyses of chapter 7 can be found ibid.. The relatively long time of decision making gets reasonable considering that the first of two exemplary trigger items requires the full reconstruction of two hadronically decaying tau leptons and their multivariate discrimination against various backgrounds as described in section 3.3.3.

3.2.5 ATLAS Data Taking

Now that the design and setup of both the LHC and the ATLAS experiment are introduced, the ATLAS data taking system can be briefly described. While the LHC provides particle collisions for all experiments, the number of events recorded by each experiment can vary. In case of the ATLAS experiment, technical properties of the detector require the system to start up slowly once the LHC is delivering stable beams. The high-voltage supply of the ATLAS tracking system, for example, needs to be raised to its working point slowly. Hence, not all luminosity delivered by the LHC is recorded by the ATLAS experiment since it is not necessarily fully functional the full time. For the data taking period of 2012, the data which is studied in the framework of this thesis, both the amount of delivered and recorded luminosity (for the ATLAS experiment) is illustrated in fig. 3.4.
However, not all recorded data by ATLAS is qualified as 'good' data. Due to detector components of ATLAS not working properly during data taking, parts of the recorded data can be labelled 'flawed' or even 'bad' instead of 'good' by the ATLAS data quality infrastructure [55]. To keep an overview of the status of data, so-called 'GoodRunLists' (GRLs) are maintained. The GRLs keep track of runs (nominally and LHC run) and luminosity blocks (LBs, discrete periods of ATLAS data taking of 60-120 s in length) labelled 'good'.
As already outlined in section 3.2.4, only events that pass the ATLAS trigger system are recorded as data. These events are directly reconstructed at the computing centre at CERN. The data is processed in

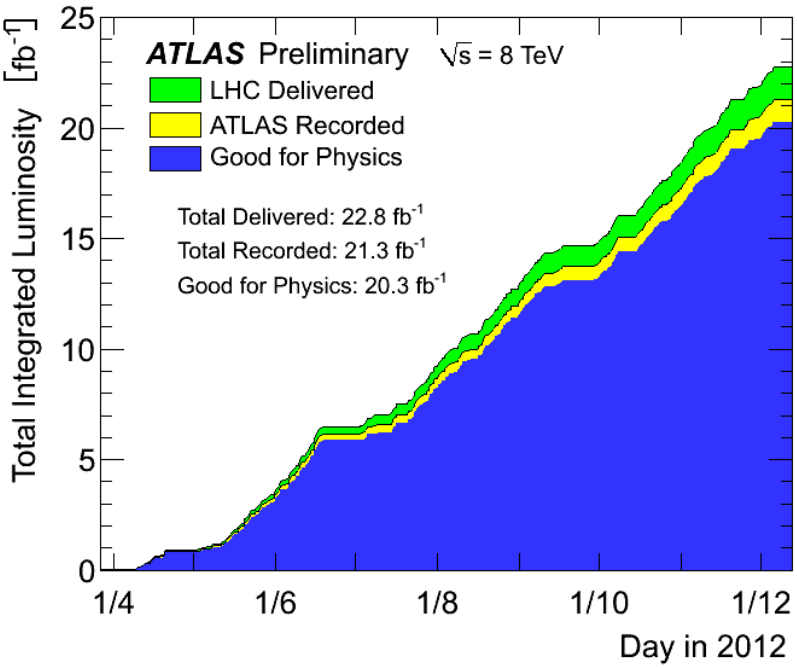

Figure 3.4: Cumulative luminosity versus time delivered to (green), recorded by ATLAS (yellow), and certified to be good quality data (blue) during stable beams and for pp collisions at 8 TeV centre-of-mass energy in 2012. Image taken from https://twiki.cern.ch/twiki/bin/view/AtlasPublic/LuminosityPublicResults#Publications_and_Conference_Resu.

so-called 'trigger-streams': the 'express stream'[2], the 'calibration stream'[3] and four 'physics streams'[4]. Figure 3.4 also illustrates the fraction of data taken by the ALTAS experiment in 2012 that is labelled 'good' and hence usable for analyses like the those performed here.

The data considered in the analysis of the Simplified Model of electroweak direct chargino pair production (c. f. chapter 7) has been taken between April 12th and December 6th in proton-proton colisions at a center-of-mass energy of $\sqrt{s} = 8\,\text{TeV}$ [15]. The trigger stream ('physics stream') used is the 'JetTauETMiss' stream that selects events with one high-p_T jet and a high value of $\not{E}_\text{T}$.

The data considered in the analysis of the strong direct squark production Simplified Model has been recorded during the same time of LHC operation and selected by the same trigger stream. The total amount of data recorded amounts to $\mathcal{L} = 21.4\,\text{fb}^{-1}$ which is reduced to $\mathcal{L} = 20.7\,\text{fb}^{-1}$ of used data due to the GRL requirements (in total 3.3% of data are lost by the requirements of the GRL). The used GRL (DetStatus-v58-pro14-01_DQDefects-00-00-33_PHYS_StandardGRL_All_Good.xml) is provided by the official ATLAS Data Preparation Group: http://atlasdqm.web.cern.ch/atlasdqm/grlgen/Susy/Susy_v01/.

[2] The express stream contains approximately 10% of a run's data and is used for calibration and data quality information.
[3] The calibration streams do not contain full event information but partial information from particular detector sub-systems that is used to calibrate those.
[4] The physics streams contain the actual data that is fully reconstructed using the information on the re-calibrated detector sub-systems.

3.3 Object and Event Reconstruction with the ATLAS Exeperiment

With all the experimental setup lined out in section 3.2 the reconstruction of particle physics events with the ATLAS detector system can be described. Since for this analysis tau leptons, jets and missing transverse energy are the objects of interest this section is restricted to explanations concerning those objects. Information on electron identification and reconstruction can be found in [56] while information on muons is provided in [57].

3.3.1 Jet Reconstruction

For the studies described in chapter 8 detailled information on objects called 'jets' is required. Jets are collimated bunches of strongly interacting particles. On parton level jets consist of quarks and gluons while on reconstruction level they are formed by charged and neutral hadrons.Since particles carrying colour charge like gluons or quarks cannot exist in free form due to the confinement of the strong interaction they 'colour-reconnect' when being separated to be colour-neutral again in the overall physics event. This can be illustrated by an example: a pair of $q\bar{q}$ changes via the weak interaction to another pair of quarks $q\prime\bar{q}\prime$. The two final state quarks will not necessarily recombine to a neutral hadron but have enough energy to escape in different directions. Due to the confinement each quark will create (colourless) pairs of $q\bar{q}$ from the vacuum and/or radiate off gluons which then again interact with other coloured particles in similar ways. Overall a bunch of coloured particles is created aligned along the path of flight of the initial particle. Colour-neutrality is conserved over the whole event by coloured particles connecting all jets.
To reconstruct a jet as a physics object three steps are run consecutively at ATLAS. In the first step calorimeter objects are grouped together from energy depositions in the calorimeter system [58]. Afterwards a jet-finder algorithm (here: 'AntiKt4Topo') is run on the calorimeter objects to form calorimeter jets [59]. In the last reconstruction step those objects are corrected to get their real energy and momentum by unfolding detector effects.
Step 1 – Calorimeter reconstruction using topological clustering: The goal of this first reconstruction step is to provide three dimensional calorimeter clusters. As seeds for the algorithm calorimeter cells with a large signal-to-noise ratio (SNR, typically $|E_{\text{cell}}| > 4\sigma_{\text{noise}}$). Here the SNR is the ratio of deposited energy in the cell over the RMS of the energy measured in random events (boehlerm). After seeding the cluster adjacent cells with $|E_{\text{cell}}| > 2\sigma_{\text{noise}}$ are added to the cluster. As a last step all neighbouring cells are added without any SNR requirement. The objects which are built in such a way are called topoclusters. Since the jet-finder algorithm needs four-momenta as an input the topoclusters are transformed into massless pseudo-particles whose energy is the sum of all cell energies of the cluster and whose spatial coordinates are given by a vector pointing from the centre of the ATLAS coordinate system to the centre of the topocluster[5][19].
Step 2 – Jet-finding using the Anti-k$_T$ algorithm: The Anti-k$_T$ algorithm tries to combine jet objects from the topoclusters provided in Step 1. The decision which objects are combined to form a jet is made by analysing the given four-momenta of the topoclusters. For every combination of two topoclusters i and j the relative squared four-momentum is derived:

$$d_{ij} = \max\left\{k_{T,i}^2, k_{T,j}^2\right\} \frac{R^2}{\Delta R_{ij}^2} \tag{3.5}$$

$$d_i = k_{T,i}^2. \tag{3.6}$$

[5] the centre is located by energy-weighting the coordinates of all cells of the cluster

In this notation $k^2_{T,i,j}$ denotes the squared four-momentum of the calorimeter object i and j, respectively, while $\Delta R^2_{i,j}$ denotes the squared distance between the objects i and j and R is the radius of the cone in which a jet is reconstructed. R is an input parameter of the algorithm and takes the values $R = 0.4$ or $R = 0.6$ in the ATLAS jet reconstruction. When all d_{ij} and d_i are computed their minimum is looked for. In case of a d_i being the minimum the calorimeter object i is labelled a calorimeter jet, it is removed from the list of input objects of the algorithm and the algorithm is run again. If a weighted combination d_{ij} is the minimum the objects i and j are combined into one new object by adding their four-momenta which replaces both objects in the input list of the algorithm – the algorithm is run again. Once all objects are removed from the input list the algorithm has combined all calorimeter objects into jets.
Since the energies of the calorimeter objects are calculated at the energy scale of the ECAL system they have to be calibrated to the hadronic scale. Furthermore corrections of the jet energy scale due to pile-up, noise and algorithm effects are performed in Step 3.
Step3 – jet energy scale calibration: This step is needed to recalculate the calorimeter jets' energies and momenta by extrapolating these properties from the electromagnetic scale on which they have been measured and reconstructed to the hadronic scale on which they are supposed to be. Furthermore detector effects like dead calorimeter cells, leakage of the calorimeter material or simply partial measurement of energy deposition have to be corrected for in the recalibration process. The calibration process according to the 'EM+JES calibration' scheme [60, 61] applies the following three steps in a jet-by-jet calibration: subtraction of energy due to pile-up (performed at the EM scale), correction of the jet position such that it originates from the event's primary vertex (which is not necessarily in the origin of the ALTAS coordinate system) and finally correcting the jet energy by comparing reconstructed and truth jet kinematics. Since this step makes several assumptions which are not necessarily true for all jets in all events (e. g. the jet is assumed to have zero mass, the modelling of calorimeter noise required for the seeding of the topoclusters is assumed to be correct in MC with respect to data, etc.) the calibration of the jets to the hadronic scale introduces systematic uncertainties (c. f. section 7.2) that have to be taken into account.

3.3.2 Missing Transverse Energy Reconstruction

a crucial variable for analyses like those performed in this thesis is the so-called missing transverse energy $\not{E}_{\mathrm{T}}$. It is defined as the imbalance of momentum in the transverse plane of the ATLAS detector. Since conservation of momentum in this plane is expected, contributions to a physics event containing particles that escape the detector unrecognised (e. g. neutrinos) can be measured by calculating $\not{E}_{\mathrm{T}}$. For searches of BSM physics $\not{E}_{\mathrm{T}}$ is an important observable due to its sensitivity to for example massive neutral particles escaping the detector that can be observed indirectly.
In principle $\not{E}_{\mathrm{T}}$ is calculated by the negative vector sum of all detected particles' four-momenta. Since in most analyses more than one undetected (so-called invisible) particle is present the spatial direction of $\not{E}_{\mathrm{T}}$ has not much informative value thus only its absolute value is of interest. This quantity is calculated in the following way:

$$E^{\mathrm{miss}}_{x,y} = E^{\mathrm{miss,\,calo}}_{x,y} + E^{\mathrm{miss,\,muon}}_{x,y} \tag{3.7}$$

$$E^{\mathrm{miss}}_{\mathrm{T}} \equiv \not{E}_{\mathrm{T}} = \sqrt{\left(E^{\mathrm{miss}}_{x}\right)^2 + \left(E^{\mathrm{miss}}_{y}\right)^2}. \tag{3.8}$$

The contributions of the x- and y-components of the missing energy are calculated from the corresponding calorimeter and muon system contributions. The calorimeter contribution is composed of several

sub-components:

$$E_{x,y}^{\text{miss, calo}} = E_{x,y}^{\text{miss, e}} + E_{x,y}^{\text{miss, }\gamma} + E_{x,y}^{\text{miss,}\tau} + E_{x,y}^{\text{miss, jets}} + E_{x,y}^{\text{miss, softjets}} + E_{x,y}^{\text{miss, calo, }\mu} + E_{x,y}^{\text{miss, CellOut}}. \quad (3.9)$$

In this formulation $E_{x,y}^{\text{miss, e}}$, $E_{x,y}^{\text{miss, }\gamma}$ and $E_{x,y}^{\text{miss, }\tau}$ denote the contributions of the electron, photon and tau reconstruction, respectively, to the calorimeter missing energy. The jet contribution is separated into two parts which distinguish between jets with transverse momenta $p_{\text{T}} > 20\,\text{GeV}$ ($E_{x,y}^{\text{miss, jets}}$) and $7\,\text{GeV} < p_{\text{T}} < 20\,\text{GeV}$ ($E_{x,y}^{\text{miss, softjets}}$). Whether contributions from muon reconstruction are considered in the calorimeter ($E_{x,y}^{\text{miss, calo, }\mu}$) or in the actual muon contribution ($E_{x,y}^{\text{miss, muon}}$) depends on their isolation from each other and other objects. Finally the $E_{x,y}^{\text{miss, CellOut}}$ contribution accounts for calorimeter cells associated to clusters but which are not matched to any physics object. All contributions are calculated and their proper energy scales i. e. $E_{x,y}^{\text{miss, e}}$ at the EM scale and $E_{x,y}^{\text{miss, jets}}$ at the hadronic scale. Each term is calculated from the negative sum of all calibrated physics objects:

$$E_x^{\text{miss}} = -\sum_{i=1}^{N_{\text{cell}}^{\text{term}}} E_i \sin\theta_i \cos\phi_i \quad (3.10)$$

$$E_y^{\text{miss}} = -\sum_{i=1}^{N_{\text{cell}}^{\text{term}}} E_i \sin\theta_i \sin\phi_i \quad (3.11)$$

with E_i being the scaled cell energy, θ_i the azimuthal angle and ϕ_i and the polar angle of cell i. All cells which are considered in this summation are within $|\eta| < 4.5$

Since the calculation of $\not{E}_{\text{T}}$ depends on the reconstruction and identification of all other physics object it is subject to systematic uncertainties like its overall calibration scale and its overall resolution. In order to avoid double-counting of systematic uncertainties only the contribution from $E^{\text{miss, CellOut}}$ is considered a $\not{E}_{\text{T}}$ systematic uncertainty while all the others are accounted for in the corresponding sources of systematic uncertainties i. e. $E^{\text{miss, }e}$ is taken into account in the systematics of electron reconstruction.

3.3.3 Tau Lepton Reconstruction

Since tau leptons are the essential property of the simplified model studies performed in this thesis their way of reconstruction and identification with the ATLAS detector is described in more detail. As a source of information the current status report of the tau reconstruction group is considered [62].

Tau leptons are the heaviest of the three charged leptons of the SM ($m(\tau) = 1.777\,\text{GeV}$ [20]) and also the most short lived ones ($\tau_\tau = 0.291\,\text{ps}$ [20]). Their mean life time corresponds to a proper decay length of $c\tau_\tau = 87.18\,\mu\text{m}$ which means they decay before they can reach the innermost layer of ATLAS detector (c. f. section 3.2.1). As a consequence, tau leptons at ATLAS can be only be identified and reconstructed by studying their decay products. Due to their high mass tau leptons are the only leptons that can decay both leptonically and hadronically. In the first case – which accounts for 35% of all tau decays [20] – the tau decays via emission of two neutrinos into a lighter lepton (e. g. $\tau^- \to \nu_\tau + \mu^- + \bar{\nu}_\mu$). Since electrons and muons are easier to detect and are reconstructed/identified in a more efficient way tau leptons decaying leptonically will always be reconstructed as muons or electrons, respectively.

Currently the only way tau leptons are reconstructed at ATLAS is in the hadronic decay channels – the remaining 65% of all tau decays [20]. In this type of decays the neutrino emitted by the tau is predominantly accompanied by one or more charged and neutral pions. Since the neutrino remains undetected the reconstruction of the visible hadronic part of the tau decay is the only way to identify

tau leptons. Due to the fact that the hadrons are reconstructed as jets it is very hard to discriminate hadrnonically decaying tau leptons from quark- or gluon-initiated jets. A possibility to distinguish hadronic tau decays from other jets is their rather narrow shower shape and the distinct number of charged tracks they leave in the detector. Taus leaving one charged track are referred to as 1-prong taus while taus leaving three charged tracks are labelled 3-prong. Currently the number of neutral pions involved in the decay is not further considered but is rather a prospect persuaded by the tau substructure group.

Reconstructing Hadronic Tau Candidates

As already described the input for the reconstruction of hadronically decaying taus—whose visible part will be referred to as $\tau_{\text{had-vis}}$—is provided by the calorimeter jets whose reconstruction is described in section 3.3.1. The input for the algorithm that constructs $\tau_{\text{had-vis}}$ candidates is seeded with those jets which have been reconstructed using the anti-k_T jet-finder algorithm (seeded with topoclusters and $R = 0.4$) and that fulfil $p_{\text{T}} \geq 10\,\text{GeV}$ and $|\eta| \leq 2.5$. The last requirement ensures that jets lie within the coverage of the ATLAS tracking system.
Since the primary vertex of the event is not necessarily the vertex the tau lepton originates from – e. g. a $Z \rightarrow \tau\tau$ event from pile-up would have a vertex rather displaced with respect to the event's primary vertex – a dedicated vertex association tool is run to find the best vertex for the $\tau_{\text{had-vis}}$ candidate. Detailed information on this Tau Jet Vertex Association tool can be found in [63].
As a next step in reconstructing the $\tau_{\text{had-vis}}$ candidates, their axes and four-momenta are calculated. In a first step a barycentre is formed for each $\tau_{\text{had-vis}}$ seed by summing up all four-vectors of its constituent clusters assuming zero mass for every cluster. Afterwards the $\tau_{\text{had-vis}}$ detector axis is calculated by taking clusters within $\Delta R < 0.2$ around the barycentre, recalculating their four-vectors in the tau vertex coordiante system and summing them up. The resulting axis defines the $\tau_{\text{had-vis}}$ direction in the $\eta - \phi$ space and is referred to as intermediate axis.
Since hadronic tau decays can contain different numbers of charged tracks the $\tau_{\text{had-vis}}$ candidates' energies are recalculated independently of the jet energy scale using a dedicated simulation based procedure described in [64]. After all these steps are performed the η position of every $\tau_{\text{had-vis}}$ candidate is recalculated to account for effects like clusters reconstructed in poorly instrumented calorimeter regions [62].
After reconstructing the calorimeter cluster of the $\tau_{\text{had-vis}}$ candidate the tracks associated to it are determined by requiring several quality criteria:

- lie within $\Delta R \leq 0.2$ around the intermediate axis(the so-called 'core cone'),
- $p_{\text{T}} \geq 1\,\text{GeV}$,
- number of hits in the pixel detector ≥ 2,
- number of hits in the pixel detector and the SCT detector ≥ 7,
- $|d_0| \leq 1.0\,\text{mm}$,
- $|z_0 \cdot \sin\theta| \leq 1.5\,\text{mm}$.

In this notation d_0 denotes the distance of the closest approach of the track to the tau vertex while z_0 describes the distance of the closest longitudinal approach. For further discrimination purposes all $\tau_{\text{had-vis}}$ candidates are classified according to their number of tracks in the core cone N_{track} as either single-prong or multi-prong. Furthermore so-called isolated tracks—i. e. tracks fulfilling the quality criteria from above and lying within $0.2 < \Delta R \leq 0.4$— are considered in the later variable calculations.

Discrimination against Jet Background

Jets initiated by quarks or gluons have a signature very similar to that of hadronically decaying tau leptons. Since such jets are produced in very high abundances at the LHC, they make up the main source of background to hadronically decaying tau leptons. In order to foster the discrimination of the desired tau leptons against the background jets a set of multivariate techniques utilising several discriminating variables is applied which is referred to as 'tauID'. At ATLAS two multivariate procedures are used – a projective likelihood method and boosted decision trees of which the latter is described here while the first is explained detailedly in [62]. Furthermore rejection against electron and muon background is improved by applying again multivariate techniques (against electrons) and a cut-based approach (against muons). Details on those methods can be found ibid..
The variables utilised in the boosted decision tree (BDT) method are numerous. For sake of simplicity at this point only few of these variables are introduced while the full set can be found ibid..
Since on average a quark-/gluon-initiated jet is wider for a given momentum than an hadronic tau shower calorimeter and tracking variables probing the shower shape are viable for discrimination purposes. Furthermore the number of tracks reconstructed around the $\tau_{\text{had-vis}}$ candidate provides separation power. One of the calorimeter variables probing the shower shape if $f_{\text{core}}^{\text{corr}}$ which is the fraction of the total tau energy contained in the centremost cone around its axis ($\Delta R < 0.1$). One of the tracking variables used is R_{track} – the average p_{T}-weighted track distance from the tau axis while in multi-prong decays additionally ΔR_{max} – the distance to the track furthest from the tau axis – is considered. Although the already mentioned short proper decay length of $c\tau_\tau = 87.18\,\mu\text{m}$ is not sufficient – not even when boosted to $\beta\gamma c\tau_\tau$ – for the tau to reach the innermost detector layer secondary vertices of the tau decay can be measured. A measurement like this is possible in the 3-prong decay case and provides the secondary vertex significance $S_{\text{T}}^{\text{flight}}$ as an additional discrimination variable. Exemplary distributions of these four variables as they are measured by the ATLAS tau combined performance group are depicted in fig. 3.5 where the good discrimination power is clearly visible since the distributions for real taus strongly differ from those for background-like jets.
Pile-up is not only an issue for jet reconstruction but also for the reconstruction of hadronically decaying tau leptons. While tracking related observables are relatively pile-up robust calorimeter variables suffer from pile-up effects to a greater extent [62]. Effects that can influence tau reconstruction are additional cells being added to clusters which are from pile-up event or additional energy deposition being added to existing clusters. Since those effects cannot be avoided they are corrected for. To achieve this the dependence of pile-up-sensitive variables on pile-up characteristics like the number of vertices in the event N_{vtx} and the average number of interactions per bunch crossing $\langle\mu\rangle$ is studied on MC level. The tau reconstruction variables are then corrected for their average change in MC simulations with respect to those two pile-up observables.
Both tauID algorithms use simulated $Z- \rightarrow \tau\tau$, $W \rightarrow \tau\nu$ and $Z' \rightarrow \tau\tau$[6] events to provide $\tau_{\text{had-vis}}$ signal candidates. The reconstruction and identification efficiency for signal events is defined as the ratio of the number of reconstructed truth-matched[7] $\tau_{\text{had-vis}}$ candidates to the number of true hadronically decaying tau leptons.
For the BDT method three working points referred to as 'loose', 'medium' and 'tight' are defined which correspond to signal efficiencies of 70%, 60% and 40% for 1-prong and 65%, 55% and 35% for multi-prong $\tau_{\text{had-vis}}$ candidates. For each working point a BDT yielding the corresponding signal efficiency is trained in order to provide the optimal selection criteria to reconstruct hadronic decays of tau leptons.

[6] The Z' events are generated to get high-p_{T} tau leptons beyond the typical p_{T} spectrum of $Z \rightarrow \tau\tau$ decays; $m(Z') \in \{250, 500, 750, 1000, 1250\}$ GeV
[7] truth-matched means the $\tau_{\text{had-vis}}$ candidate lies within $\Delta R < 0.2$ of a true 1- or 3-prong tau

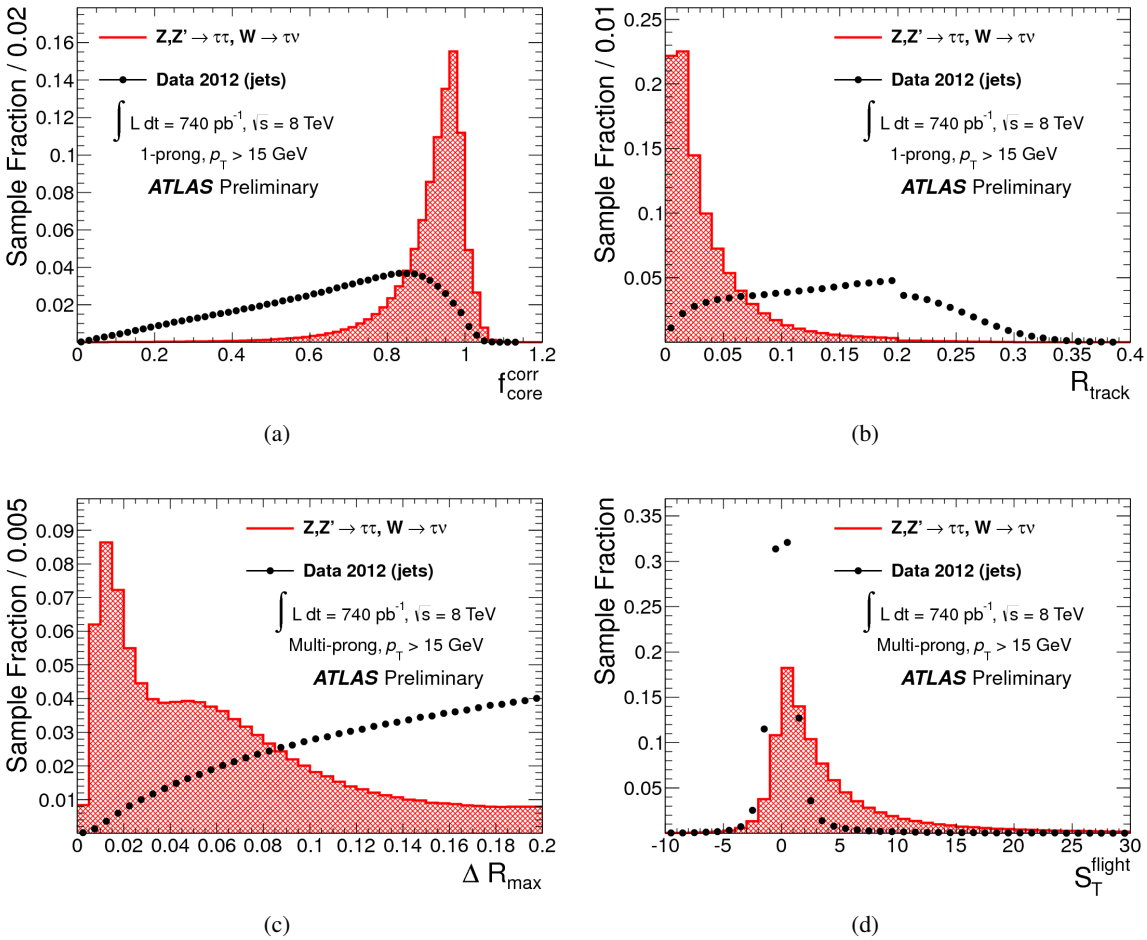

Figure 3.5: Distributions of the four discriminating variables $f_{\text{core}}^{\text{corr}}$, R_{track}, ΔR_{max} and $S_{\text{T}}^{\text{flight}}$ for simulated $z, Z' \to \tau\tau$ and $W \to \tau\nu_\tau$ signal samples and a jet background sample selected from 2012 ATLAS data. The distributions are normalised to unity. Detailed descriptions of the variables can be found in [62]; figures taken from ibid..

In order to ensure that the reconstruction of $\tau_{\text{had-vis}}$ candidates works in the same way in both data and simulation the behaviour of the reconstruction efficiency in both cases is studied. By measuring the reconstruction efficiency directly in data and comparing it to the performance figures for MC scale factors are derived to account for deviations [62]. By applying these scale factors to the simulated events the hadronic tau decays of a particular analysis are ensured to be modelled in the best possible way. The systematic uncertainties introduced due to these scaling factors of the tauID are referred to tauID systematics while the recalibration of the tau energy scale (c. f. section 3.3.3) is a source of systematic uncertainties itself.

Recalibration of Energy and Momentum

Since the reconstruction of hadronically decaying tau leptons is seeded from already fully reconstructed and calibrated calorimeter jets a certain energy calibration—the Local Hadron Calibration (LC) as it is applied for calorimeter jets—is already applied to the reconstructed tau leptons. The LC accounts for effects on the topological clusters reconstructed at the EM scale but not for effects like energy loss before the calorimeter or pile-up contributions. To correct the tau energy for these effects a designated tau energy scale (TES) recalibration is performed. Information on this topic used here is taken from [64]. Additional and more detailed information can be found ibid..
The momentum of hadronically decaying tau leptons is recalibrated by comparing truth-level and reco.-level hadronic tau decays in simulated $W \to \tau\nu$, $Z \to \tau\tau$ and $Z' \to \tau\tau$ events. After imposing several conditions on the selected tau candidates and matching the reconstructed ones to truth-level taus the tau response is calculated. The tau response is defined as the ratio of reconstructed tau p_{T} under LC to the true visible tau transverse momentum. The arising distribution is binned in the true visible transverse momentum and the reconstructed pseudo-rapidity. After fitting a Gaussian to the distribution for every tau in every event—depending on its visible transverse momentum and reconstructed pseudo-rapidity—a correction factor is derived by determining the offset of the Gaussian's means from one. Exemplary response curves are depicted in figs. 3.6 and 3.7. This way it is possible to calibrate the tau visible energy to its true value.

In addition to the recalibration of the tau visible energy the tau pseudo-rapidity is corrected for mis-measurements like effects arising from poorly instrumented regions of the ATLAS calorimeter like the transition between barrel and endcap parts. Since clusters in these regions tend to have underestimated energies the introduced bias is corrected for by recalculating $|\eta^{\tau}| = \left|\eta^{\tau}_{\text{reco.}}\right| - \eta_{\text{bias}}$ with $\eta_{\text{bias}} = \langle\left|\eta^{\tau}_{\text{reco.}}\right| - \left|\eta^{\tau}_{\text{true}}\right|\rangle$. After applying these two calibration steps the reconstructed tau momentum and the transverse momentum agree with their true values within 1% on average for 1-prong taus and 2% on average for multi-prong taus. However, the tau response remains a function of pile-up. To account for pile-up effects the tau properties are recalibrated once more by comparing the average number of vertices in a sample to the number of reconstructed vertices in each event. Detailed information on this procedure is provided in [64].
Since all measurements used in the tau reconstruction process suffer from finite resolution, the combined tau momentum resolution is calculated from the difference between the final calibrated momentum p^{τ}_{F} and the true visible momentum $p^{\tau}_{\text{vis., true}}$. The resolution is obtained by fitting a Gaussian and dividing its σ by the mean value of the $p^{\tau}_{\text{vis., true}}$ distribution [64]. The relative momentum resolution approximately scales as

$$\frac{\sigma}{p} = \frac{a}{\sqrt{p}} \oplus b, \tag{3.12}$$

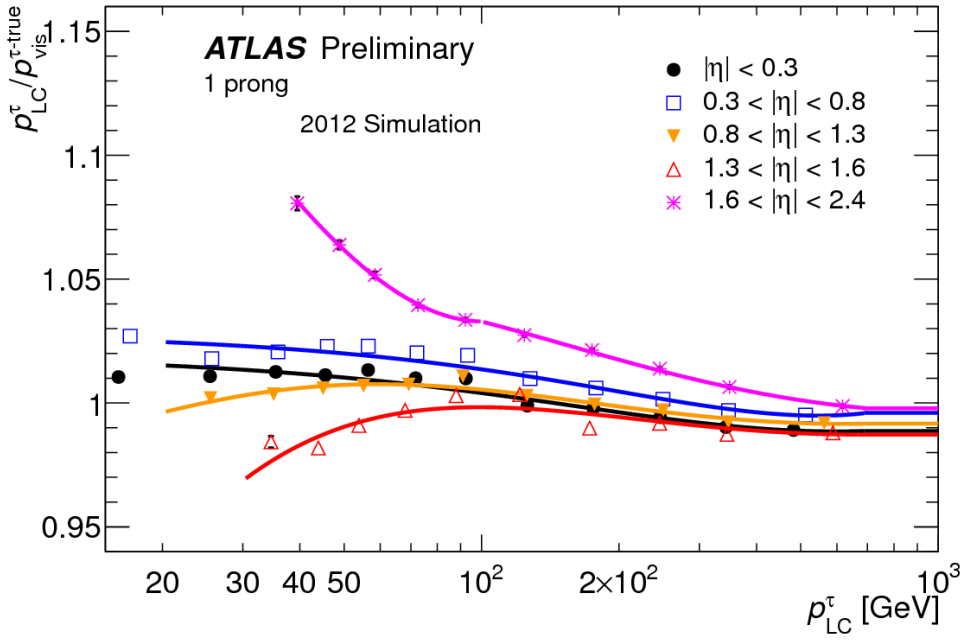

Figure 3.6: Reponse curves as a function of the reconstructed $\tau_{\text{had-vis}}$ momentum at LC scale in bins of $|\eta^{\tau}_{\text{reco.}}|$ for 1-prong taus. The uncertainties are smaller than the markers in most bins [64].

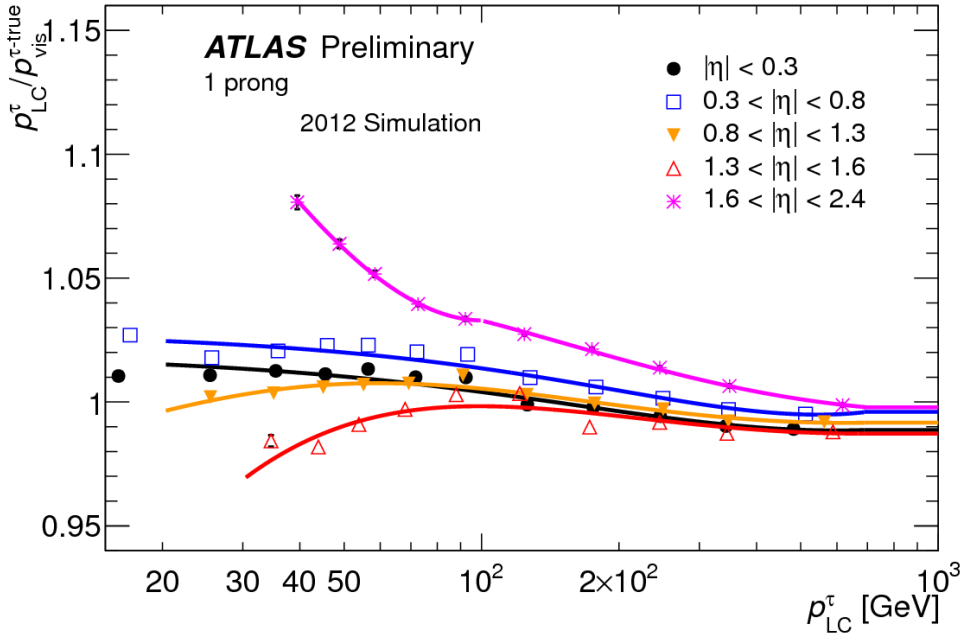

Figure 3.7: Response curves as a function of the reconstructed $\tau_{\text{had-vis}}$ momentum at LC scale in bins of $|\eta^{\tau}_{\text{reco.}}|$ for multi-prong taus. The uncertainties are smaller than the markers in most bins [64].

where the parameters a and b are obtained from fitting the functional form to the resolution distributions defined above.
How the systematic uncertainties that the tau energy scale recalibration and the finite momentum resolution introduce are estimated is described in [64].

CHAPTER 4

Monte Carlo Simulations and Statistics

This chapter is dedicated to the introduction of two rather technical but yet important topics which are both necessary in order to understand the analyses performed in the framework of this thesis.
The first section briefly describes how (new) physics events are simulated in order to later interpret the results obtained from studying data while the second section introduces the statistical tools that are used to set limits on model parameters given the amount of observed events.

4.1 Monte Carlo Simulations

In order to be able to interpret the results of particle physics experiment the simulation of physics events and their interactions with the detector are an important tool [19]. The process of simulating a complete particle physics event is performed in two steps which are described in the following: the event generator level where the actual physics process is simulated and the virtual detector level where the response of the physics inside the ATLAS detector is simulated. Furthermore this section introduces an alternative version of the detector simulation which is used in the generation of the MC samples used in this thesis: the fast simulation tool AFII.

4.1.1 Event Generator

It is known from quantum mechanics that the outcome of an experiment can only be predicted with a certain probability. Utilising event generators with pseudo random numbers many particle physics events can be simulated. According to the probability density functions (pdf) provided by theory the expected distributions become accessible. By comparing those distributions to data the results of an experiment can be interpreted. This step of generating so-called truth or truth-level events, respectively, is split into several steps which are illustrated in fig. 4.1:

1. **Hard scattering**: The primary interaction of colliding protons is the hard scattering process (c. f. fig. 4.1 a) [19]. Its outcome is determined by calculating the matrix elements of perturbation theory. For this step the parton distribution function of the proton has to be known. Depending on the generator used tree-level or higher order matrix elements are taken into account.

2. **Initial and Final State Radiation**: QCD and electroweak theory impose radiative corrections to a process which are considered by initial and final state radiation. These corrections can be

calculated by the amplitudes of the corresponding matrix elements [19]. Those amplitudes can be calculated for up to eight final state partons providing accurate information. The approach chosen to model these effects is the parton shower approach described in [65]. Initial state radiation can be modelled as spacelike parton showers (c. f. fig. 4.1 b) while final state radiation as timelike parton showers (c. f. fig. 4.1 c).

3. **Multiple Interactions**: Since protons are composite particles made out of partons the assumption that only one parton-parton interaction (hard scattering) occurs during a proton-proton collision is not necessarily true. In the case of multiple parton interactions (c. f. fig. 4.1 d) proton remnants carrying a part of the total energy are colour-connected to rest of the interaction (c. f. fig. 4.1 e).

4. **Hadronisation**: While perturbative QCD is well able to describe gluon radiation and interaction of colour-charged particles it breaks down once confinement becomes dominant – the hadronisation of coloured particles into colourless hadrons takes place (c. f. fig. 4.1 f). This process has to be described by phenomenological models whose implementation differs for different event generators. The decay of hadrons via hadronic showers or their direct interaction with the detector is not modelled on generator but on detector simulation level [19].

The event generator used to simulate the truth-level physics of the Simplified Models analysed in the framework of this thesis is Herwig [66]. It is a general purpose event generator designed for high-energy processes with particular emphasis on QCD parton showers. Additionally Herwig is rather well-suited for simulating SUSY physics since it can directly process the output of various SUSY spectrum calculators.
Once all physics on generator i. e. truth-level is simulated it is put into the detector simulation in order to mimic its appearance as 'data'.

4.1.2 Virtual Detector

The virtual ATLAS detector used for simulating the signature of MC events in the detector is modelled by the 'GEometry ANd Tracking' (GEANT4) tool-kit [67]. This tool simulates the passing of particles through matter [19]. In case of the ATLAS experiment the final state hadrons and long-lived particles like muons and electrons generated by the event generator traverse the detector and interact with its different active and passive components (c. f. section 3.2). The position of every interaction of a generated particle in the simulated detector is recorded and stored as a so-called 'hit'. Once this is done for all particles the hits are transferred into digital signals corresponding to the actual output of the individual detector readout system [19]. After this step is carried out a MC event looks like a data event and can be reconstructed in the same way (c. f. section 3.3).
Due to the fact that the process of event generation starting with the hard scattering process and ending with the fully reconstructed event consumes approximately 10 to 15 minutes of computing time per event a speed-up of the simulation chain is desired. Within ATLAS this achieved by substituting the detector response step of the calorimeter system with the fast simulation tool 'AFII'. While typically the calorimeter response is calculated by considering the signal induced by every single shower particle, AFII takes template showers given the particle properties and calorimeter component. Due to time constraints in the framework of this thesis the generated MC samples are reconstructed by using AFII. However, the quality of the Fast Simulation samples has been validated by comparing tau-specific variables in AFII and Full Simulation samples. For the grid point $m(\tilde{\chi}_1^{\pm}) = 520\,\text{GeV}$, $m(\tilde{\tau}_1) = 510\,\text{GeV}$ of the electroweak direct chargino pair production Simplified Model a Full Simulation sample containing the same number of events as the AFII samples (20,000) has been generated. Figures A.1, A.1 and A.3

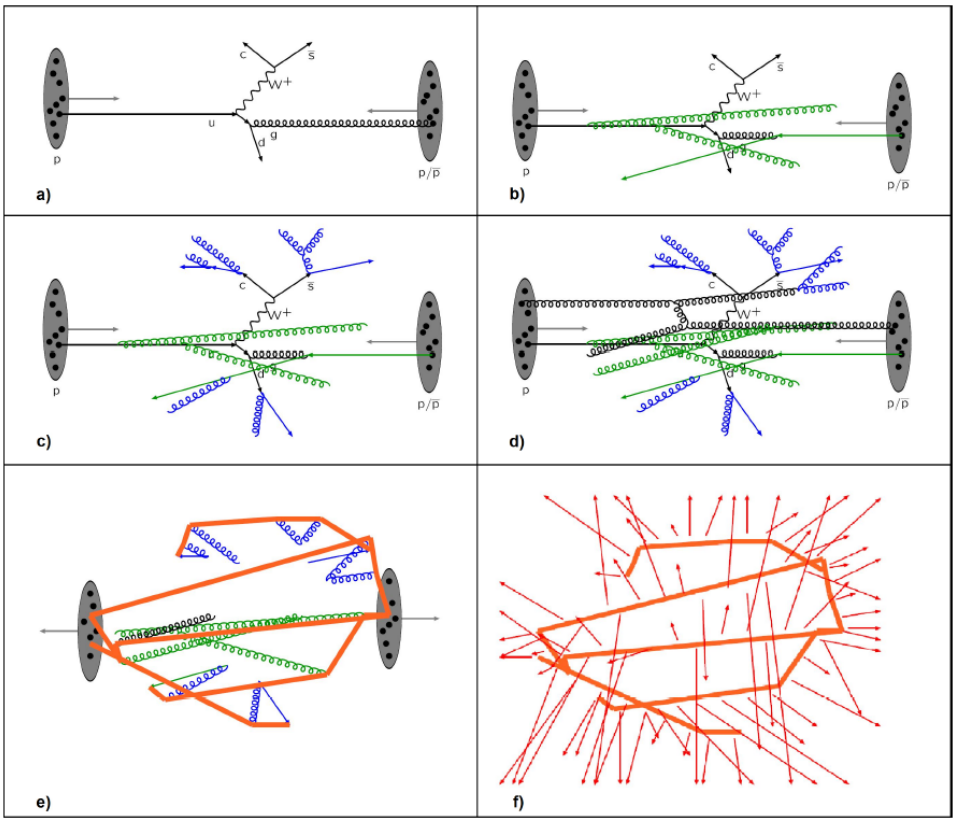

Figure 4.1: Schematic of the sub-processes considered during truth-level event generation: (a) illustrates the hard scattering process on parton level which can be described by matrix elements. (b) Initial state radiation can be described as spacelike parton showers (gluon radiation in green). (c) Final state radiation can be described as timelike parton showers (blue). (d) Multiple interactions occurring due the composite structure of the proton are illustrated in black, ISR in green and FSR in blue again. (e) The colour connection of all coloured particles and proton (and beam) remnants is illustrated. (f) shows the formation and decay of final state hadrons arising from the hadronisation phase [19].

in appendix A depict the distributions of the tau transverse momentum, the tau pseudo-rapidity and the score of BDT trained to separate hadronically decaying tau leptons from jets. For all three distributions a (qualitatively) good agreement can be observed. This good agreement justifies the use of AFII generated MC samples instead of fully simulated MC samples. However, the application of AFII and its differences with respect to the full simulation are still under more detailed investigation within the ATLAS collaboration.

4.2 Setting of Exclusion Limits

The search for new physics beyond the Standard Model is strongly correlated with the question when to claim a discovery (and how to quantify it if possible) or how to set exclusion limits on parameters of tested models of new physics. This chapter introduces the fundamental statistical tools and procedures that are required for both scenarios taking its information from [68].
One method to claim the discovery of a new model or to exclude it to some degree is based on a frequentist significance test which uses a likelihood ratio as a test statistic[1] [68]. In general the signal and background models used in this test will be described by parameters such as the model's cross section and nuisance parameters. While the first are a priori known e. g. given by the used physics generator, the latter have to be determined by a fit to data. In order for this approach to work the model is assumed to be sufficiently flexible so that for a particular set of parameters is can be regarded as true. Systematic uncertainties can be taken into account by introducing additional parameters.
For the line of argumentation to start assume for each event the measurement of a variable x which is written into a histogram $\mathbf{n} = (n_1, n_2, \ldots, n_N)$. The expectation value for the ith bin of the histogram can then be written as

$$E[n_i] = \mu s_i + b_i \tag{4.1}$$

$$s_i = s_{\text{tot}} \int_{\text{bin}i} f_s(x; \theta_s) \mathrm{d}x \tag{4.2}$$

$$b_i = b_{\text{tot}} \int_{\text{bin}i} f_b(x; \theta_b) \mathrm{d}x. \tag{4.3}$$

In this nomenclature s_i and b_i denote the mean number of entries in the ith bin from signal and background, respectively, while μ denotes the signal strength. Hence, $\mu = 0$ corresponds to the background-only hypothesis while $\mu = 1$ represents the nominal signal hypothesis. s_{tot} and b_{tot} denote the total mean numbers of signal and background event. With $f_s(x; \theta_s)$ ($f_b(x; \theta_b)$) being the probability density function (pdfs) of the variable x for signal (background) and θ_s (θ_b) representing parameters that characterise the shape of the pdf the integrals yield the probabilities to find an event in bin i. While s_{tot} is fixed to the value predicted by the nominal signal model b_{tot} is a nuisance parameter which can be merged into one variable denoting a vector of all nuisance parameters $\theta = (\theta_s, \theta_b, b_{\text{tot}})$.
In order to constrain the nuisance parameters additional measurements can be made. An example for such a procedure is the selection of control regions where mainly background events are expected with respect to the actual signal region. A histogram of e. g. a kinematic variable in such a control region $\mathbf{m} = (m_1, m_2, \ldots, m_M)$ then has an expectation value

$$E[m_i] = u_i(\theta). \tag{4.4}$$

[1] Using a likelihood ratio is suggested by the Neyman-Pearson lemma (c. f. [69])

Here, u_i denotes calculable quantities depending on the nuisance parameters θ. Also in principle possible is the construction of such a measurement in order to provide information on b_{tot} and the signal and background shape parameters.
The likelihood function now has the form of Poisson probabilities for every bin of the histograms:

$$L(\mu, \theta) = \prod_{j=1}^{N} \frac{(\mu s_j + b_j)^{n_j}}{n_j!} e^{-(\mu s_j + b_j)} \prod_{k=1}^{M} \frac{u_k^{m_k}}{m_k!} e^{-u_k} \tag{4.5}$$

In order to test a hypothesised value of μ the profile likelihood ratio

$$\lambda(\mu) = \frac{L(\mu, \hat{\hat{\theta}})}{L(\hat{\mu}, \hat{\theta})}, \tag{4.6}$$

where $\hat{\hat{\theta}}$ denotes the value of θ that maximises L for a specified μ i. e. is the conditional maxium-likelihood estimator of θ. $\hat{\theta}$ and $\hat{\mu}$ are conditional maximum-likelihood estimators maximising the denominator.
By considering this profile likelihood ratio the hypothesis in the numerator is tested against the 'best fit' hypothesis in the denominator. For the ratio $0 \leq \lambda \leq 1$ holds while λ near 1 implies good agreement between the data and the hypothesised value of μ. As a consequence a test statistic as the basis of a statistical test can look like

$$t_\mu = -2 \ln \lambda(\mu). \tag{4.7}$$

Higher values of t_μ then correspond to worse agreement between the two hypotheses. The level of disagreement can be quantified by means of a so-called p-value:

$$p_\mu = \int_{t_\mu,\text{obs.}}^{\infty} f(t_\mu|\mu) \mathrm{d}t_\mu. \tag{4.8}$$

In this notation t_μ, obs. is the value of t_μ observed from data and $f(t_\mu|\mu)$ the pdf of T_μ under the assumption of the signal strength μ. The relation between the obtained p-value, t_μ, obs. and $f(t_\mu|\mu)$ is illustrated in fig. 4.2. A common criterion when to reject a tested hypothesis is when its test yields $p < 0.05$ which corresponds to a probability of less than 5% to find data that describes the tested hypothesis properly or worse. Typically a signal strength value μ corresponding to such an 95% CL exclusion can be derived by sampling $f(t_\mu|\mu)$ until $p = 0.05$ is found. This value of μ can be transferred into 95% CL limits on basically any variable e. g. numbers of events or cross sections.
Finally the way $f(t_\mu|\mu)$ is computed needs to be explained in more detail. The computing time consuming way is to calculate t_μ for varying data input i. e. the number of observed events in data is varied around its true value and for every so-called 'toy experiment' t_μ is computed. The challenge of this approach lies within the sampling rate and range with which this artificial function is approximated. A less time-consuming approach has been proposed in [68]: it is possible to asymptotically approximate the profile likelihood ratio which saves a lot of the computing time which is needed to test the large number of parameter sets in order to maximise each likelihood.
Applying this procedure of hypothesis tests new physics discoveries can be claimed or—more likely to occur—exclusion limits on parameters of new physics models can be derived.

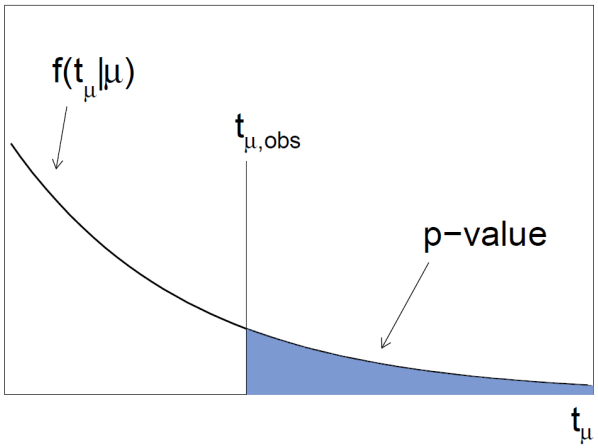

Figure 4.2: Illustration of the relation between the p-value obtained from an observed value of the test statistic t_μ and the pdf $f(t_\mu|\mu)$ [68].

CHAPTER 5

Development of Simplified Models

After developing the basic idea of SUSY searches with Simplified Model this chapter motivates and describes the development of the Simplified Models analysed in the framework of this thesis.

5.1 Model Selection

The process of deciding on particular models is driven by several criteria:

- This thesis is aiming for SUSY searches with final state tau leptons. Hence a model producing tau leptons is needed. This can be achieved by requiring the stau sparticle to be the NSLP.
- Since this thesis is studying physics events recorded with the ATLAS experiment at the LHC, initial processes which are of high abundance at the LHC are desired. As a consequence the main goal is the analysis of a strongly produced simplified model.
- What are potential hidden parameters of a Simplified Model and how can they be investigated?

In order to cover the aspect of the presence of final state tau leptons inspiration for Simplified Models can be found by studying the phase space of GMSB models. Since the stau slepton is often the NSLP in GMSB scenarios (c. f. the GMSB mass spectrum depicted in fig. 2.3 in section 2.2.1) and conservation of R-parity is assumed a tau-rich phase space is expected.
By studying GMSB MC samples produced for the ATLAS collaboration at a LHC centre-of-mass energy of $\sqrt{s} = 7$ TeV prosperous supersymmetric process fulfilling the requirements mentioned above are looked for. For several points on the GMSB signal grid parametrised by the SUSY breaking scale parameter Λ and the VEV ratio $\tan\beta$ the abundance of different supersymmetric decay chains is evaluated. Table 5.1 summarises the obtained results. Since the overall goal is to construct a strongly produced Simplified Model table 5.1 distinguishes between strongly and electroweakly produced supersymmetric decay chains. In this notation 'strong' refers to a decay chain which starts with a strongly interacting particle and 'electroweak' denotes decay chains starting with particles that only interact electroweakly. Furthermore all abundances given are as absolute values taken from MC samples with 10,000 events and hence—due to R-parity conservation—a total of 20,000 supersymmetric decay chains. Having a more detailed look at table 5.1 several observations can be made: for low values of Λ charginos are predominantly produced in the electroweak column while for higher values of Λ direct production of sleptons is dominating. This again is replaced by direct stau production once $\tan\beta$ reaches higher values

Λ / TeV	$\tan\beta$	most abundant elw. chain	abundance	most abundant strong chain	abundance
30	30	$\tilde{\chi}^+ \to \tilde{\tau}_1 \to \tilde{G}$	2130	$\tilde{q}_R \to \tilde{\chi}^0 \to \tilde{\tau}_1 \to \tilde{G}$	2246
35	30	$\tilde{\chi}^+ \to \tilde{\tau}_1 \to \tilde{G}$	2198	$\tilde{g} \to \tilde{q}_R \to \tilde{\chi}^0 \to \tilde{\tau}_1 \to \tilde{G}$	1648
40	30	$\tilde{\chi}^+ \to \tilde{\tau}_1 \to \tilde{G}$	2195	$\tilde{q}_R \to \tilde{\chi}^0 \to \tilde{\tau}_1 \to \tilde{G}$	1236
45	30	$\tilde{\chi}^+ \to \tilde{\tau}_1 \to \tilde{G}$	2152	$\tilde{q}_R \to \tilde{\chi}^0 \to \tilde{\tau}_1 \to \tilde{G}$	932
50	30	$\tilde{l}_R \to \tilde{\tau}_1 \to \tilde{G}$	2193	$\tilde{q}_R \to \tilde{\chi}^0 \to \tilde{\tau}_1 \to \tilde{G}$	688
60	2	$\tilde{l}_R \to \tilde{G}$	4824	$\tilde{q}_R \to \tilde{\chi}^0 \to \tilde{l}_R \to \tilde{G}$	719
60	5	$\tilde{l}_R \to \tilde{G}$	3570	$\tilde{q}_R \to \tilde{\chi}^0 \to \tilde{l}_R \to \tilde{G}$	622
60	10	$\tilde{l}_R \to \tilde{G}$	3416	$\tilde{q}_R \to \tilde{\chi}^0 \to \tilde{l}_R \to \tilde{G}$	54
60	15	$\tilde{l}_R \to \tilde{G}$	3325	$\tilde{q}_R \to \tilde{\chi}^0 \to \tilde{l}_R \to \tilde{G}$	490
60	20	$\tilde{l}_R \to \tilde{\tau}_1 \to \tilde{G}$	2863	$\tilde{q}_R \to \tilde{\chi}^0 \to \tilde{l}_R \to \tilde{\tau}_1 \to \tilde{G}$	397
60	30	$\tilde{l}_R \to \tilde{\tau}_1 \to \tilde{G}$	3282	$\tilde{q}_R \to \tilde{\chi}^0 \to \tilde{l}_R \to \tilde{\tau}_1 \to \tilde{G}$	384
60	40	$\tilde{\tau}_1 \to \tilde{G}$	4018	$\tilde{q}_R \to \tilde{\chi}^0 \to \tilde{\tau}_1 \to \tilde{G}$	392
60	50	$\tilde{\tau}_1 \to \tilde{G}$	8040	$\tilde{q}_R \to \tilde{\chi}^0 \to \tilde{\tau}_1 \to \tilde{G}$	367
60	55	$\tilde{\tau}_1 \to \tilde{G}$	12137	$\tilde{g} \to \tilde{q}_R \to \tilde{\chi}^0 \to \tilde{\tau}_1 \to \tilde{G}$	217
70	30	$\tilde{l}_R \to \tilde{\tau}_1 \to \tilde{G}$	3956	$\tilde{q}_R \to \tilde{\chi}^0 \to \tilde{l}_R \to \tilde{\tau}_1 \to \tilde{G}$	212
80	30	$\tilde{l}_R \to \tilde{\tau}_1 \to \tilde{G}$	4664	$\tilde{q}_R \to \tilde{\chi}^0 \to \tilde{l}_R \to \tilde{\tau}_1 \to \tilde{G}$	94

Table 5.1: Absolute abundances of electroweak (i. e. starting with a $\tilde{l}$ or a $\tilde{\chi}$) and strong (i. e. starting with a $\tilde{q}$ or a $\tilde{g}$) decay chains for different points in the GMSB parameter space. In total each MC sample contains 10.000 events i. e. a total of 20.000 supersymmetric decay chains is present. The notation $\tilde{q}_{L,R}$ denotes only first and second generation squarks—sbottom and stop are explicitly excluded in this nomenclature—while $\tilde{l}_{L,R}$ denotes left- and right-handed light sleptons, respectively.

(for a fixed value of Λ). On the other hand, the distribution of strongly produced decay chains does not change much. However, a clear decrease in the abundance can be observed for increasing values of Λ. These observations can be explained:
The enhanced production of charginos for lower values of Λ can be explained by the fact that Λ defines an overall mass scale for all SUSY particles which are thus lighter for lower values of Λ. Furthermore chargino production is possible with an s- and a t-channel diagram (c. f. fig. 5.3) while stau production is only possible via an s-channel diagram (c. f. fig. 5.1).
The overall low abundance of decay chains labelled 'strong' is due to the fact that by construction strongly interacting particles in GMSB scenarios are much heavier than sleptons and gauginos. Thus their production probability is only high at low values of Λ. Furthermore only the most abundant strong chain of each MC sample is displayed. There can be strong chains of similar abundance which are not explicitly named but which would contribute to a much higher overall abundance of strong chains (e. g. for $\Lambda = 30\,\text{TeV}$, $\tan\beta = 30$: $\tilde{g} \to \tilde{q}_R \to \tilde{\chi}_1^0 \to \tilde{\tau}_1 \to \tilde{G}$ appears 2211 times and $\tilde{q}_L \to \tilde{\chi}_1^\pm \to \tilde{\tau}_1 \to \tilde{G}$ appears 1174 times)
Since the elements of the matrices mixing the $\tilde{\tau}$ mass eigenstates from the chirality eigenstates are proportional to β and to the masses of the corresponding SM superpartner τ the mass splitting between $\tilde{\tau}_1$ and $\tilde{\tau}_2$ also depends on β and thus on $\tan\beta$. On the other hand the same effect—distinguishing between the two mass eigenstates for each of the light sleptons $\tilde{e}$ and $\tilde{\mu}$—can be neglected as the mass splitting is too small to be relevant. This is why one only distinguishes between chirality eigenstates of light sleptons and not between mass eigenstates as for the third generation sleptons. By construction the chirality eigenstates of light sleptons are degenerate ($m(\tilde{e}) = m(\tilde{\mu})$ for both left and right chiral eigenstates) in GMSB. As a result varying $\tan\beta$ for a given value of Λ (e. g. $\Lambda = 60\,\text{TeV}$) does not influence the light

slepton mass but increase the $\tilde{\tau}$ mass splitting and drives the lower $\tilde{\tau}_1$ mass more down until it is lighter than the light sleptons. While at some points in the parameter space ($\Lambda = 60\,\text{TeV}$, $\tan\beta \in \{20, 30\}$) direct production of light sleptons with a $\tilde{\tau}_1$ being part of the decay chain is still favoured due to the fact that the production is blind in terms of slepton flavour, at points of higher $\tan\beta$ ($\tan\beta \in \{40, 50, 55\}$) the $\tilde{\tau}$ is so light that is the particle which is most likely to be produced.
Judging from table 5.1 the direct production of squarks which decay via a gaugino to a stau NSLP is the candidate to construct a strongly produced Simplified Model from. Considering the presence of gauginos in such a model, investigating the hidden sector of gaugino mixing is an interesting pre-study. A Simplified Model to study gaugino properties would be for example the pair production of decay chains like $\tilde{\chi}_1^{\pm} \rightarrow \tilde{\tau}_1^{\pm} \rightarrow \tilde{G}$. Finally a pre-study regarding the hidden sector of stau sleptons is of major interest since the stau is present in all Simplified Models relevant for this thesis. Such a model could be constructed from the direct stau pair production case where the stau decays into a gravitino and a tau lepton.
Last but not least the question of the LSP has to be considered. Since some SUSY scenarios propose the lightest neutralino $\tilde{\chi}_1^0$ as the LSP a gravitino LSP is in principle restricted to GMSB scenarios. However, since the differences between a neutralino LSP and a gravitino LSP can be investigated in terms of hidden parameter studies the gravitino can be considered the LSP without much loss of generality.
The following sections introduce the Simplified Models which are designed and studied in the framework of this thesis.

5.2 Electroweak Direct Stau Pair Production

The first simplified model presented in this thesis is designed both to cover the part of the parameter space where direct $\tilde{\tau}_1$ production is dominant and to study the hidden sector of the final strong production model that is due to the stau slepton. The only contributing leading order diagram is shown in fig. 5.1.

As the production cross section for electroweak processes is rather low at the LHC this model is

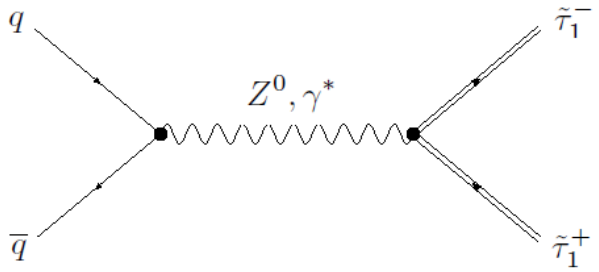

Figure 5.1: s-channel diagram for direct stau pair production. Stau sparticles are only produced via annihilation of a $q\bar{q}$-pair into either a Z^0 or a γ which then produce a pair of stau sparticles electroweakly.

not of much importance for actual searches for SUSY but rather well-suited for other studies. As a consequence there are is no designated signal point grid designed for this model in terms of varying sparticle masses but a study on an interesting hidden parameter is performed.
The hidden parameter of this simplified model is the mixing angle in the 2×2 unitary matrix which forms the physical mass eigenstates of the $\tilde{\tau}$-doublet from the chirality eigenstates.

$$\begin{pmatrix} \tilde{\tau}_1 \\ \tilde{\tau}_2 \end{pmatrix} = \begin{pmatrix} \cos\Theta_{\tilde{\tau}} & \sin\Theta_{\tilde{\tau}} \\ -\sin\Theta_{\tilde{\tau}} & \cos\Theta_{\tilde{\tau}} \end{pmatrix} \begin{pmatrix} \tilde{\tau}_L \\ \tilde{\tau}_R \end{pmatrix}$$

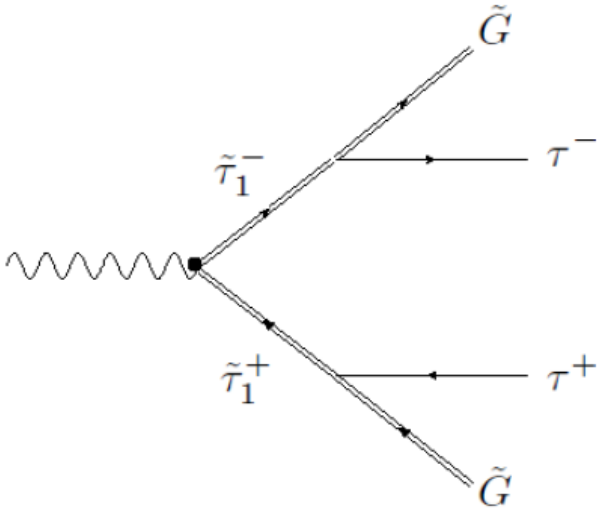

Figure 5.2: Decay topology of events of the Simplified Model of electroweak direct stau pair production. The topology is characterised by the presence of two oppositely charged tau leptons and missing energy due to the LSPs escaping detection.

In this context it should be kept in mind that $\tilde{\tau}$-sleptons are scalar particles i. e. they have spin 0. As a result chirality is, stricly speaking, not defined for them. But since this formulation of representing sparticles in a chiarlity basis is adopted for SUSY models from the SM the subscripts L and R are to be taken as simple labels.
For a fixed value of the $\tilde{\tau}_1$ mass ($m(\tilde{\tau}_1) = 150\,\text{GeV}$) this hidden parameter is varied over its full range $[0 \ldots \frac{\pi}{2}]$ to study a possible influence on further analyses.
On the one hand effects of the variation of the stau mixing angle are expected to be visible in variables that are sensitive to changes in the angular distributions of the events. Since chirality is passed on from the stau mother particle to the daughter tau lepton—for which it is a well-defined quantum number since the tau is a fermion—effects on angular distributions of the tau decay products are expected to be seen due effects on the particles' helicity for conserving three-momenta and spin.
On the other hand effects on kinematic observables of the tau leptons and the event's missing energy are expected (c. f. section 6.1).
By probing the influence of the stau mixing on such variables an important question can be answered: Is the stau mixing angle truly hidden parameter which does not influence the sensitivity of an analysis? The answer to this question is given ibid..

5.3 Electroweak Direct Chargino Pair Production

As already seen in section 5.1 for lower values of Λ the process $\tilde{\chi}_1^\pm \to \tilde{\tau}_1^\pm \to \tilde{G}$ is favoured in production with respect to the direct production of stau sleptons. In addition to this argument the possibility to study hidden parameters of the charged gaugino sector motivates the design of such a simplified model.
The hidden parameter studied in this simplified model is the mixing angle of the 2×2 matrix composing the mass eigenstates of the electroweak eigenstates. This mixing process occurs for positively and negatively charged chargino doublets seperately but not independently (c. f. the following formulae). To clarify this point some notation is introduced [70]:

$$\psi^+ \equiv \begin{pmatrix} \lambda^+ \\ \tilde{h}_2^1 \end{pmatrix}$$

$$\psi^- \equiv \begin{pmatrix} \lambda^- \\ \tilde{h}_1^2 \end{pmatrix}.$$

With $\psi^\pm$ being coloumn vectors each containing a gaugino field component $\lambda^\pm$ and a higgsino field component $\tilde{h}_{2,1}^{1,2}$ the chargino contribution to the Lagrangian can be written in the form

$$-\mathcal{L}_{\text{mass}}^c = (\psi^-)^T X \psi^+ + \text{h.c.} \tag{5.1}$$

with X being a 2×2 matrix providing the sparticle masses:

$$X = \begin{pmatrix} M_2 & \sqrt{2} M_W \sin\beta \\ \sqrt{2} M_W \cos\beta & \mu \end{pmatrix}.$$

The matrix X can be diagonalised by two unitary matrices U and V to form a diagonal matrix M_c^D with real nonnegative values being the chargino masses $\tilde{M}_1$ and $\tilde{M}_2$:

$$U^* X V^{-1} = M_c^D. \tag{5.2}$$

The two chargino mass eigenstate fields can then be written in the form

$$\chi_k^+ = V_{km} \psi_m^+ \tag{5.3}$$

$$\chi_k^- = U_{km} \psi_m^-. \tag{5.4}$$

In this notation $k = 1, 2$ denotes the two chargino mass eigenstates. Depending on X the two mixing matrices have the form

$$U = O_u \tag{5.5}$$

$$V = \begin{cases} O_v \text{ for } \det X > 0, \\ \sigma_3 O_v \text{ for } \det X < 0 \end{cases}$$

$$O_{u,v} = \begin{pmatrix} \cos\phi_{u,v} & \sin\phi_{u,v} \\ -\sin\phi_{u,v} & \cos\phi_{u,v} \end{pmatrix}$$

with σ_3 being a Pauli matrix. As one can see $O_{u,v}$ looks like a classical rotation matrix parametrised only by one angle $\phi_{u,v}$. This angle determines how 'wino-like' and how 'higgsino-like' a physical chargino eigenstate is. Possible consequences of a variation of this parameter could be differences in the production cross sections as the coupling structure at the corresponding vertices changes.
In addition to the chargino mixing angle the mass of the LSP is chosen to be studied as a (more or less) hidden parameter. By varying this parameter the transition between models with a close-to-massless LSP like GMSB and models with a massive LSP like MSUGRA is supposed to be approximated.
As pseudo-observables parametrising the model the masses of the actually decaying sparticles $\tilde{\tau}_1$ and $\tilde{\chi}_1^\pm$ are chosen. To really describe the model with only these two pseudo-observables the t-channel diagram has to be suppressed with respect to the s-channel diagram (c. f. fig. 5.3). For the t-channel diagram an additional dependence of the production cross section on the mass of the exchanged virtual particle (the squark in this case) arises. To be independent of the squark mass as a third parameter it is fixed to a high

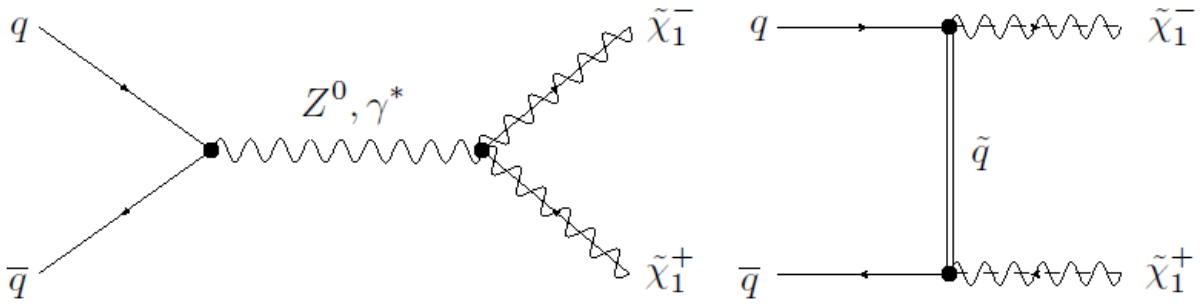

Figure 5.3: s- and t-channel chargino pair production diagrams. While s-channel production happens via annihilation of a $q\bar{q}$-pair into either a Z^0 or a γ^* the t-channel process must contain a virtual squark and is thus senstive to the exchanged sparticle's mass.

value ($m(\tilde{q}) \approx 7\,\text{TeV}$) which is supposed to suppress the t-channel diagram strongly enough to enable production only via the s-channel diagram.
The lower bound of the free parameters of the simplified model is chosen such that the lightest chargino is above the best limit set by LEP2 ($m\tilde{\chi}_1^{\pm} > 103.5\,\text{GeV}$) [71–75] and the stau is always lighter than the chargino to allow the decay at all. The upper bound is set to the arbitrary value of 700 GeV. Within these ranges the sparticle masses are varied in steps of $\approx 100\,\text{GeV}$ to provide a coarse grid structure. In addition to each coarse step on the grid there are two grid points set up around the equality of masses to resolve lower mass differences. The overall structure of the parameter grid for this simplified model is shown in table 5.2. While the values of $m\left(\tilde{\tau}_1^{\pm}\right)$ are chosen to meet above requirements the values of $m\left(\tilde{\chi}_1^{\pm}\right)$ and the mixing angles of the chargino sector are calculated to match the theory of the MSSM. The chargino masses and the mixing angles are connected via the cMSSM parameters M_2, μ and β and the mass of W-Boson [70]:

$$\begin{aligned}
\tilde{M}_{2,1}^2 &= \frac{1}{2}\Bigg[\left|M_2^2\right| + \left|\mu^2\right| + 2M_W^2 \pm \Big\{\left(\left|M_2^2\right| - \left|\mu^2\right|\right)^2 \\
&\qquad + 4M_W^4 \cos^2 2\beta + 4M_W^2\left(\left|M_2^2\right| + \left|\mu^2\right| + 2\Re\left(M_2\mu\right)\sin 2\beta\right)\Big\}^{1/2}\Bigg] \\
\tan 2\phi_u &= \frac{2\sqrt{2}M_W(\mu\sin\beta + M_2\cos\beta)}{M_2^2 - \mu^2 - 2M_W^2\cos 2\beta} \\
\tan 2\phi_v &= \frac{2\sqrt{2}M_W(\mu\cos\beta + M_2\sin\beta)}{M_2^2 - \mu^2 + M_W^2\cos 2\beta}.
\end{aligned} \tag{5.6}$$

Here $\tilde{M}_{2,1}$ denotes the mass of the heavier (lighter) chargino mass eigenstate while $\phi_{u,v}$ denotes the angle of the mixing matrix of the negatively (positively) charged chargino doublet. To account for those correlations between physical masses and mixing angles a set of parameters (M_2, μ, β) (M_W is fixed to the measured SM value [20]) is chosen which yields a value of $\tilde{M}_1$ that is in the desired range to a viable precision while $\tilde{M}_2 > 2000\,\text{GeV}$ is required to ensure $\tilde{\chi}_1^{\pm}$ production only. Since various sets (M_2, μ, β) fulfil those requirements the parameter β is fixed to an arbitrary value and kept constant for all further derivations. For grid points with—according to table 5.2— vanishing mass differences the actual mass difference is $< 0.5\,\text{GeV}$ and thus neglected in the number of displayed digits.
Similar to the simplified model with direct $\tilde{\tau}_1$ pair production one point on the parameter grid is chosen to be varied with respect to the two hidden parameters. As being of average mass difference between

$\tilde{\chi}_1^\pm$-$\tilde{\tau}_1^\pm$ grid point selection, masses in GeV							
$m\left(\tilde{\chi}_1^\pm\right)$	121	221	321	420	520	620	700
$m\left(\tilde{\tau}_1^\pm\right)$	100	100	100	100	100	100	100
	110	200	200	200	200	200	200
	120	210	300	300	300	300	300
		220	310	400	400	400	400
			320	410	500	500	500
				420	510	600	600
					520	610	680
						620	690
							700

Table 5.2: Grid point selection of the $\tilde{\chi}_1^\pm$-$\tilde{\tau}_1^\pm$ grid.

$\tilde{\chi}_1^\pm$ and $\tilde{\tau}_1$ and more or less in the middle of the grid the point $m\left(\tilde{\chi}_1^\pm\right) = 520\,\text{GeV}$, $m\left(\tilde{\tau}_1\right) = 300\,\text{GeV}$ is chosen. The chargino mixing angle ϕ_u[1] is varied within $[1° \ldots 44°]$. This choice is motivated by the fact that fully wino-/higgsino-like charginos are not reasonable since the parameter $\mu = 0$ can be excluded[2]. In addition mixing angles within $[46° \ldots 89°]$ would be redundant to the range chosen above since they correspond to a parameter set (M_2, μ, β) that generates the same mass eigenvalues. This phenomenon is due to the symmetry of the mass eigenvalue formulae under exchange of M_2 and μ.
The mass of the gravitino LSP is varied between $O\,(\text{eV})$ and $O\,(\text{GeV})$ to generate both GMSB-like scenarios with a close-to-massless LSP and MSUGRA-like scenarios with a massive LSP.
With pure s-channel production ensured the topology of events of this simplified model look as depicted in figure 5.4. The signature of such an event in the detector would be characterised by two oppositely

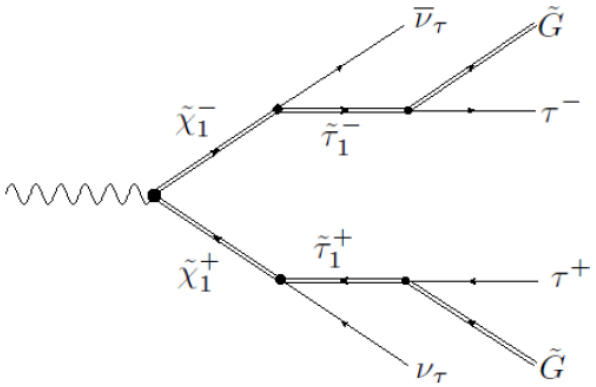

Figure 5.4: Decay topology of the elw. s-channel production chargino-stau grid events. The event topology is characterised by two oppositely charged tau leptons and large amounts of $\not{E}_\text{T}$ due to the two LSPs and the two neutrinos escaping the detector.

charged τ-leptons, absence of jets as no hadronic particles are involved and rather high values of missing transverse energy. The latter is due to the fact that not only the two gravitino LSPs escapte the detector but also two neutrinos from the chargino decay remain undetected.

[1] ϕ_v is calculated according to the parameter set which generated ϕ_u
[2] $\mu = 0$ would prevent the SM process of electroweak symmetry breaking

Since an analysis of a similar grid with the same expected event topology is performed in [15] parts of that analysis are adopted for the studies of this simplified model.

5.4 Strong Direct Squark Production

Having covered the topics of chargino and stau contributions to a strongly produced Simplified Model grid by investigating the influence of potentially hidden parameters the development of the final goal—a strong production Simplified Model—can be pursued. The starting point of developing a strongly produced model with final state tau leptons is again table 5.1. This overview suggests the production of the decay chains $\tilde{g} \to \tilde{q}_{\mathrm{L,R}} \to \tilde{\chi}_1 \to \tilde{\tau}_1 \to \tilde{G}$ or $\to \tilde{q}_{\mathrm{L,R}} \to \tilde{\chi}_1 \to \tilde{\tau}_1 \to \tilde{G}$. In both scenarios electroweak gauginos are involved. Those can be either $\tilde{\chi}_1^0$ or $\tilde{\chi}_1^\pm$. Since charginos are studied in the simplified model of section 5.3, and the hidden parameter sector is much more complicated for neutralinos (c. f. section 5.5) the charged gaugino is chosen to fill the decay chain between the strongly produced sparticle and the obligatory $\tilde{\tau}_1$. An argument for chosing squarks over gluinos as the initial sparticle of the decay chain is the fact that gluinos in GMSB are—by construction—heavier than squarks and that an elongated decay chain ($\tilde{g} \to \tilde{q}$ compared to $\tilde{q}$) would induce at least one additional parameter to the grid namely the gluino mass. Motivated by those arguments of simplicity the decay chain $\tilde{q} \to \tilde{\chi}_1^\pm \to \tilde{\tau}_1 \to \tilde{G}$ is chosen. In this notation $\tilde{\mathrm{q}}$ contains both left- and right-handed chiral eigenstates of the first and second generation squark mutliplets. The third generation squarks are explicitly avoided due to their non-vanishing mass splittings and the corresponding mixing angles as additional hidden parameters. Furthermore the phenomenology of physics involving third generation (s)quarks differs from those involving only (s)quarks of first and second generation. Another more technical aspect regarding this decision is the fact that the presence of third generation quarks introduces new Standard Model backgrounds to an analysis .New hidden parameters beyond the stau and chargino mixing angles are not analysed within this model.
The number of pseudo-observables parametrising this simplified model is relatively high compared to the models described above. Taking the masses of all the particles involved including the LSP mass they sum up to four. Since there is no point in choosing a coarser or finer grid granularity for one or more of these four parameters a total number of four points subdividing each grid point leading to $4^4 = 256$ grid points. The choice of upper and lower boundaries for each parameter is motivated as follows:
For the squark mass the values are chosen to be rather high in order to leave enough freedom to chose the decay particle masses:
$(m(\tilde{q}) \in \{900\,\mathrm{GeV}, 1100\,\mathrm{GeV}, 1300\,\mathrm{GeV}, 1500\,\mathrm{GeV}\})$.
The chargino mass is adjusted for each grid point to match the requirement $m(\tilde{q}) - m\left(\tilde{\chi}_1^\pm\right) = 100\,\mathrm{GeV}$. This ensures that the lowest values are around the LEP2 exclusion limit of $\approx 103\,\mathrm{GeV}$[71–75]. A similar requirement constrains the stau mass: $m\left(\tilde{\chi}_1^\pm\right) - m(\tilde{\tau}_1) = 100\,\mathrm{GeV}$. To cover the spectrum from a close-to-massless LSP scenario to a massive LSP model the gravitino mass is equidistantly spread over four values within $[0 \ldots m(\tilde{\tau}_1)]$. In case of a grid point with zero gravitino mass the mass is fixed to 10 keV. As a last step in the design of this model the gluino mass is set to a high value with respect to the squark mass ($m(\tilde{g}) = 70\,\mathrm{TeV}$). This step is supposed to keep out any influence of the gluino sector on the model. However, what has to be kept in mind is the resulting suppression of two tree-level t-channel diagrams. This aspect is expected to result in a lower production cross section of this Simplified Model grid with respect to similar strong production models that do not control this parameter.
All possible tree-level production diagrams for electroweak and strong production of this model, even the suppressed ones, are depicted in figs. 5.5 to 5.7 while the decay topology of a typical event of this simplified model is illustrated in fig. 5.8.

The expected signature due to the topology in fig. 5.8 involves two tau leptons, large amounts of missing

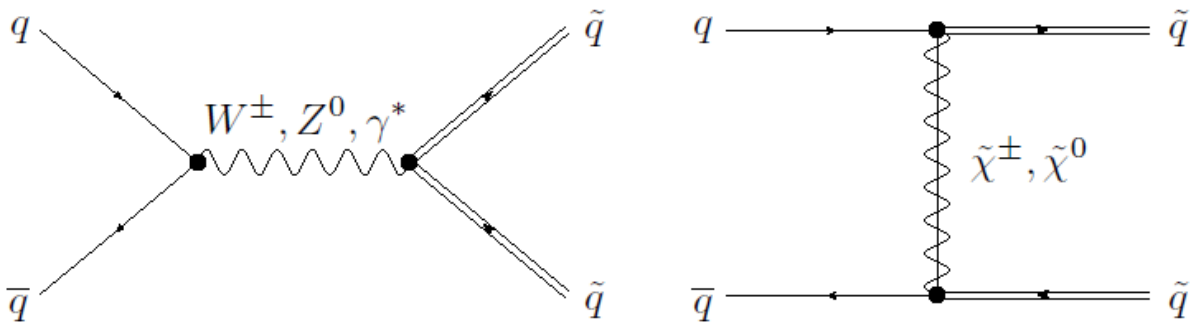

Figure 5.5: *s*- and *t*-channel diagrams for electroweak direct squark pair production. In contrast to the diagrams for elw. direct chargino pair production $W^{\pm}$ bosons are also possible exchanged particles in the *s*-channel due to the fact that the produced squark pair is not required to be electromagnetically neutral. In the *t*-channel all gauginos are possible exchanged particles.

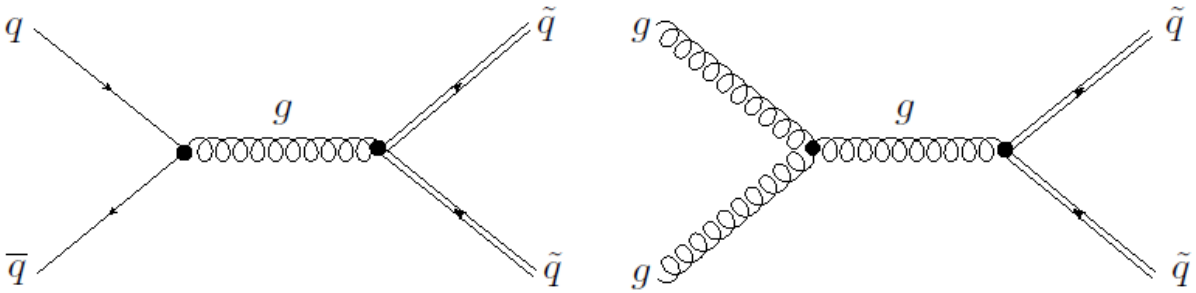

Figure 5.6: *s*-channel diagrams for strong direct squark pair production.

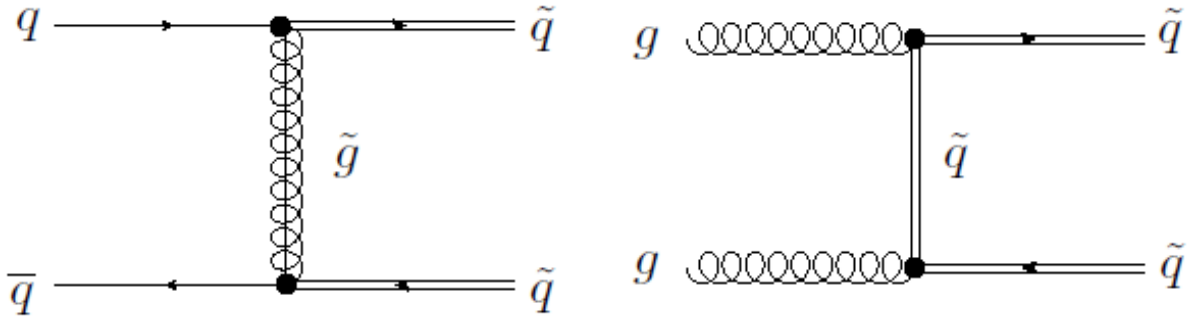

Figure 5.7: *t*-channel diagrams for strong direct squark pair production. Depending on the incoming particles the virtual particle can be either a squark or a gluino. The diagram involving the virtual gluino is strongy suppressed by setting the gluino mass to a very high value $m(\tilde{g}) = 70\,\text{TeV}$.

transverse energy and the presence of two jets from the two quarks involved in the squark decay. Since a similar analyses—the search for SUSY with large missing transverse energy, jets and tau leptons—is pursued within the ATLAS collaboration [14] this analysis adopts part of the analysis strategy presented ibid..

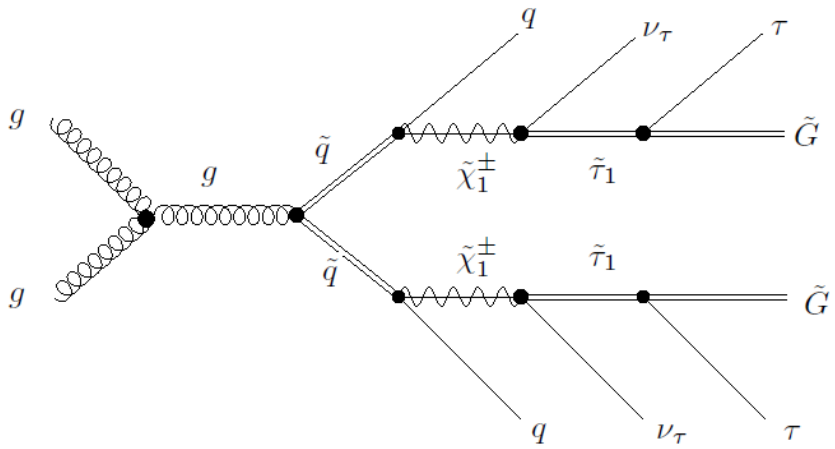

Figure 5.8: *s*-channel diagram for direct $\tilde{q}$ pair production and the corresponding decay.

5.5 Further Ideas and Prospects

As already mentioned in section 5.1 the number of possible Simplified Models is nearly endless and only three have been introduced in the framework of this thesis. The design of the models presented here is a compromise between practicality—i. e. being easily describable—and versatility in terms of covering an parameter space as large as possible. However, certain aspects are not covered by the selection of these Simplified Models and can inspire future developments.

Interesting in addition to the direct electroweak production of charginos is a similar model but with neutralinos as initial sparticles of the supersymmetric decay chain. Since the decay $\tilde{\chi}_1^0 \rightarrow \tilde{\tau}_1^{\pm} + \tau^{\mp} \rightarrow \tau^{\pm} + \tilde{G} + \tau^{\mp}$ would involve a second tau lepton, a total of four tau leptons would be expected in the final state of such an event. Such an event topology would be interesting since the reconstruction of the tau leptons could be performed both in hadronic and leptonic channels. As a result of this versatility in terms of tau reconstruction the expected SM backgrounds would be rather low due to the rareness of such an event topology in the SM. On the downside the parametrisation of the neutral gaugino sector is more complex than the charged sector due to the combination of the chargino mass eigenstate quadruplet from the electroweak quadruplet via a unitary 4×4 matrix (c. f. [70]).

A similar idea could be the substitution of the chargino for the neutralino in the strong production grid described in section 5.4. This would of course come with similar advantages and drawbacks as the direct neutralino grid proposed above.

Staying in the sector of strong production, simplified models including a gluino decaying into the squark into the grid from section 5.4 is worth considering in order to approach nGM-like models[3].

Finally substituting the (first and second generation) squarks for third generation sbottom/stop squarks is interesting in terms of the SUSY breaking mechanism giving rather low masses to the superpartners of the heaviest SM particles which is necessary to solve the hierarchy problem [28]. In addition, a strong production grid with stop squarks being initially produced could be cross-checked fairly well since several other SUSY searches within the ATLAS collaboration are looking explicitly for such scenarios (c. f. [78–80]).

[3] nGM is an abbreviation for 'natural gauge-mediated symmetry breaking' which is similar to GMSB models. nGM is more fine-tuned than GMSB in order to allow Higgs masses which are in agreement with the discovery of Higgs boson-like particle at the LHC[76, 77]

CHAPTER 6

Electroweak direct stau pair production

Studying electroweak direct stau pair production is the first step towards analysing and understanding the strong production grid outlined in section 5.4. The study of this simplified model is not supposed to yield exclusion limits on the mass of the stau slepton but rather to estimate the influence of the stau mixing angle on supersymmetric processes involving stau sleptons as they are part of the two more detailed analyses following. As a consequence this chapter only contains the results of the stau mixing angle study performed with a fixed set of other parameters (c. f. section 5.2). Furthermore this analysis does not apply any selection criteria to suppress background since it analyses only truth-level information.

6.1 Selection and Results

The topology of the events produced within this simplified model is depicted in fig. 5.2. In order to make sure this very event topology is produced by the generator, a loose matching of tau leptons to their mother stau sleptons is performed. Furthermore the tau lepton is required to decay hadronically – however no information on the hadronic final state is accessible. Taus that fulfil these requirements contribute to the following analysis steps.
Since the mixing angle controls how much left- and right-chiral content each component of the stau mass eigenstate doublet contains a study of the polarisation of the final state decay products of the $\tilde{\tau}_1$ sleptons is a good approach. This ansatz is motivated by the fact that particles pass on their chirality to their daughter particles which can be measured in certain angular-sensitive variables by exploiting knowledge about the particles' spin and behaviour under CP-transformation. This can be clarified by a short example illustrated in figure 6.1: For a mixing angle of $\theta_{\tilde{\tau}} = 0°$ the lighter stau becomes purely left-chiral i. e. $\tilde{\tau}_1 \equiv \tilde{\tau}_L$ (keeping in mind that chirality here only refers to a label, not a physical property). When the $\tilde{\tau}_1$ decays it passes its chirality on to its daughter particle τ for which chirality now is a physical property since it has non-zero spin. Without loss of generality the τ shall be a τ^- i. e. a particle not an antiparticle. Since for particles in the ultra-relativistic limit[1] chirality translates into helicity, the τ^- will be left-handed in terms of helicity. When the τ^- decays into its neutrino (which is always left-handed in both chirality and helicity!) and e. g. a charged pion the two daughter particles have designated directions of flight in the τ^- rest frame due to conservation of helicity and three-momentum. The whole process is schematically depicted in figure 6.1 for a left-chiral and thus in terms of helicity left-handed τ^-. Furthermore figure 6.1 shows the same process from a right-chiral τ^+ originating from

[1] the tau leptons here can be considered ultra-relativistic since their momenta are high with respect to their rest mass

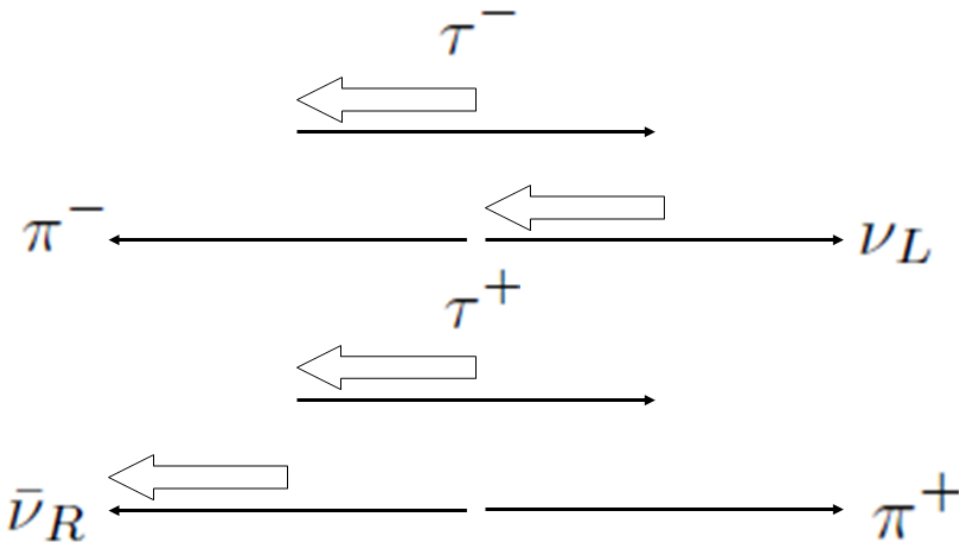

Figure 6.1: Schematic illustration of polarisation effects in tau decays with π-mesons. The thin arrows indicate the particles' three-momenta while the thick arrows indicate the projection of their spin onto their direction of flight. Each process is displayed in the τ rest frame. Thus the three-momentum of the τ lepton should be zero, however, it is chosen to be displayed being non-zero in order to infer the particle's helicity.

a right-chiral $\tilde{\tau}_R^+$[2]. Since in the ultra-relativistic limit the 'handedness' of helicity is the opposite of the 'handesness' of chirality for antiparitcles (behaviour under CP-transformation) the τ^+ is left-handed in helicity. As a consequence the antineutrino from the τ^+ decay has—due to conversation of helicity and three-momentum—a different direction of flight in its mother particles rest frame than the neutrino from the τ^- decay.
A variable which is sensitive to these polarisation effects is for example the angle between the emitted ν_τ or $\bar{\nu}_\tau$, respectively, and the mother τ^- or τ^+, respectively in the mother particle's rest frame. This observable is expected to be rather differently distributed for decays of positively and negatively charged taus.
In order to probe the same physical effect another variable is used in this analysis. Motivated by the fact that a daughter particle emitted in its mother particle's direction of flight has different energy with respect to the case of being emitted in the opposite direction, the ratio of the neutrino energy and the mother τ energy in the lab frame can be used to study the τ polarisation and thus the $\tilde{\tau}$ mixing angle. For neutrinos emitted into the direction of flight of the τ the ratio is expected to be larger than for neutrinos emitted in backward direction of the τ flight path. Since both these variables require explicit information on the neutrino from the tau decay these variables are only accessible on truth-level.
In addition to those two polarisation variables the tau transverse momentum and its pseudo-rapidity distributions are analysed. In contrast to the polarisation variables from above these two observables are accessible both in data and simulation though they strongly depend on the tau reconstruction efficiency. All of those distributions are plotted in figs. 6.2 to 6.5.
Since the study of this simplified model is just an intermediate step towards a better understanding of the strong production simplified model no studies of the production cross section dependence on the stau mixing angle are performed.

[2] For $\theta_{\tilde{\tau}} = 0°$ also the $\tilde{\tau}_1^+$ is left-chiral but since this particle could not decay conserving chirality it will couple to Higgs boson and flip its chirality to right-handed. The right-chiral $\tilde{\tau}_1^+$ now can decay to a right-chiral τ^+

Looking at the charge-sensitive left and centre plots of each distribution row charge-depended changes in the distributions with respect to variation of the mixing angle are clearly visible. Judging from the shape of these distributions the charge-dependent effects seem to cancel out when the analysis is charge-blind. This point is supported by looking at the right figure of each row which shows the charge-independent distributions of the variables – these distributions show no more mixing angle dependence. However, the charge-dependent effects of the mixing angle variation are not the ones expected from the argumentation above. The deviation from the expectation can be explained by considering the branching ratios of the hadronically decaying SM τ leptons. These decay predominantly into ρ-mesons ($\approx$ 25%) and a_1-mesons ($\approx$ 18%) while the basis of argumentation—the τ decay into pions—only occurs in $\approx$ 12% of all cases [81]. As a consequence, an entangled mixture of decays into vector (ρ), pseudo-vector (a_1) and pseudo-scalar mesons (π) makes up the plots discussed above. While the line of argumentation fostering the expectation holds for scalar mesons it is no more valid for (pseudo)vector mesons since these can have more than one designated helicity state. An exemplary configuration of a hadronic tau decay with ρ vector mesons involved is depicted in fig. 6.6. Comparing this configuration to the $\tau \to \pi + \nu$ case from fig. 6.1 leads to the conclusion that both processes would more or less cancel each other out with respect to their charge-dependent effects when varying the stau mixing angle.

As a consequence the observed phenomena of charge-dependent tau polarisation effects as a probe for the stau mixing angle cannot be explained with this set of truth-level events.

6.2 Summary

For a fixed value of the stau mass $m(\tilde{\tau}_1) = 150\,\text{GeV}$ the influence of the stau mixing angle on several variables has been studied. Since the stau mixing angle controls the chirality of the stau sparticles which is closely related to the kinematic observable helicity the mixing angle dependence of helicity-sensitive observables has been investigated. Considering the different hadronic decay modes of tau leptons a dependence of the polarisation-sensitive distributions of $\angle(\tau, \nu)$ and E_ν/E_τ on the mixing angle was expected. Dependencies are visible when distinguishing positively and negatively charged tau leptons and vanish when being insensitive to the tau charge. However, the observed dependencies cannot be fully explained by studying the helicity configurations of the different decay products since no information on the hadronic decay products of the tau lepton is available.

Nevertheless a charge-sensitive dependence of the tau transverse momentum on the stau mixing angle is observed. This dependence can be of non-negligable importance since the transverse momentum is a crucial variable in both the reconstruction/identification of tau leptons and analyses themselves. Once the efficiency of an analysis is affected by the tau transverse momentum and a charge sensitivity is present the stau mixing angle is not necessarily a hidden parameter any more – though no quantitative statements can be made so far.

However, the stau mixing angle will remain a hidden parameter for further analyses within the framework of this thesis since no polarisation effects of tau leptons are to be investigated and the charge dependence is confined to requiring an opposite-charge tau pair in the Chargino-Stau analysis.

A future prospect for a similar analysis like this one would be a more detailed study of the final state tau lepton polarisation by utilising information on the hadronic decay particles and thus enabling explanations of the here observed phenomena.

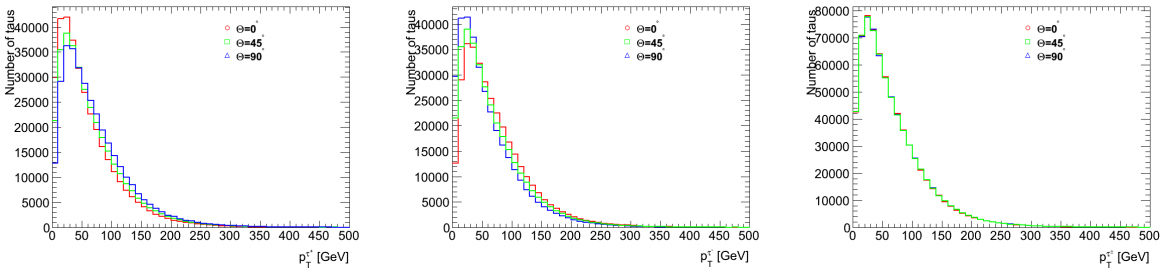

Figure 6.2: True tau p_{T} distributions for τ^+ (left), τ^- (centre) and independent of the tau charge (right) for varying stau mixing angles ($\theta_{\tilde{\tau}} = 0°$ red, $\theta_{\tilde{\tau}} = 45°$ green and $\theta_{\tilde{\tau}} = 90°$ blue)

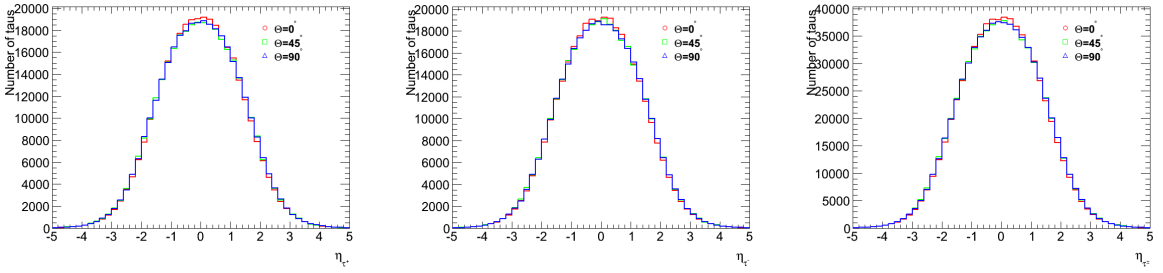

Figure 6.3: True tau η distributions for τ^+ (left), τ^- (centre) and independent of the tau charge (right) for varying stau mixing angles ($\theta_{\tilde{\tau}} = 0°$ red, $\theta_{\tilde{\tau}} = 45°$ green and $\theta_{\tilde{\tau}} = 90°$ blue)

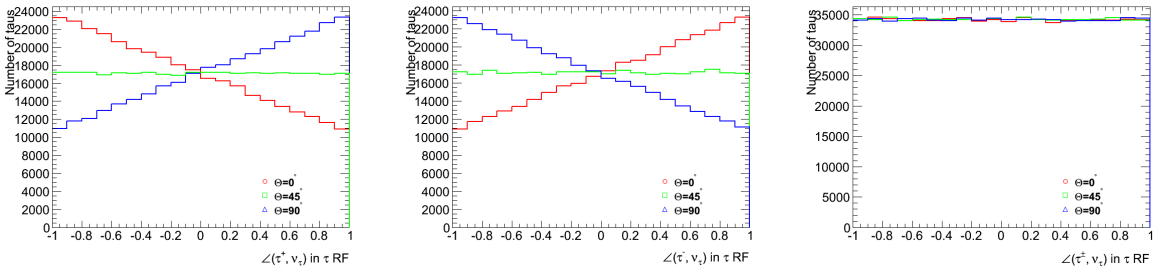

Figure 6.4: True $\angle(\tau, \nu_\tau)$ distributions in the τ RF for τ^+ (left), τ^- (centre) and independent of the tau charge (right) for varying stau mixing angles ($\theta_{\tilde{\tau}} = 0°$ red, $\theta_{\tilde{\tau}} = 45°$ green and $\theta_{\tilde{\tau}} = 90°$ blue)

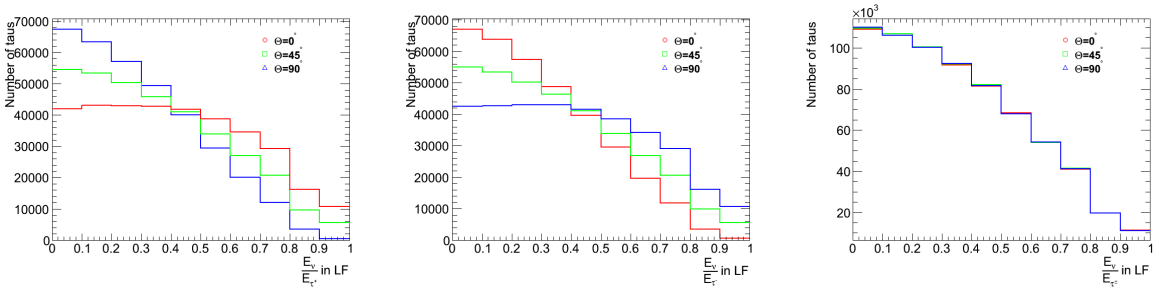

Figure 6.5: True $\frac{E_\nu}{E_\tau}$ distributions in the LF for τ^+ (left), τ^- (centre) and independent of the tau charge (right) for varying stau mixing angles ($\theta_{\tilde{\tau}} = 0°$ red, $\theta_{\tilde{\tau}} = 45°$ green and $\theta_{\tilde{\tau}} = 90°$ blue)

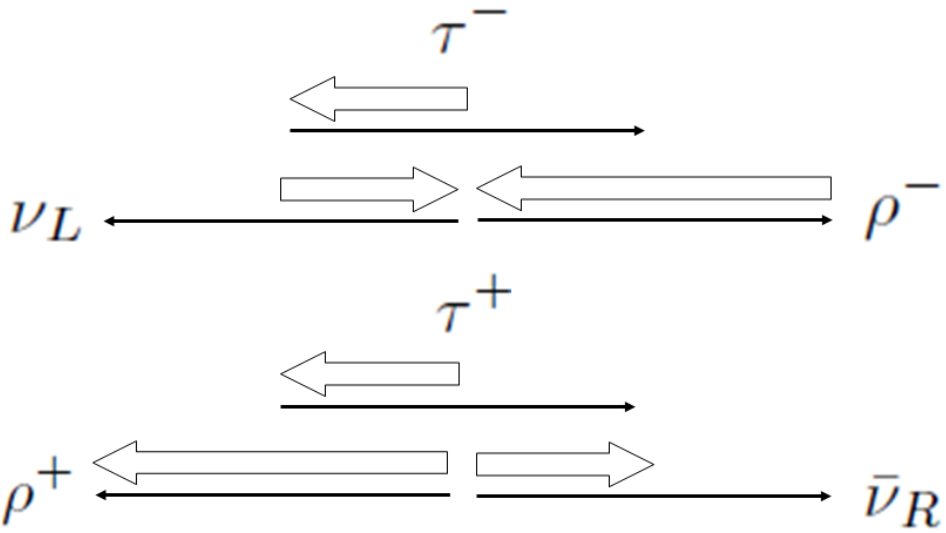

Figure 6.6: Schematic illustration of polarisation effects in tau decays with *rho*-mesons. The thin arrows indicate the particles' three-momenta while the thick arrows indicate the projection of their spin onto their direction of flight. Each process is displayed in the τ rest frame. Thus the three-momentum of the τ lepton should be zero, however, it is chosen to be displayed being non-zero in order to infer the particle's helicity.

CHAPTER 7

Electroweak Direct Chargino Pair Production

This chapter describes the analysis of the Simplified Model of direct electroweak chargino production. It is subdivided into setions explaining the event selection, listing the Standard Model backgrounds of the analysis and the systematic uncertainties considered. It finishes with a section presenting and explaining the obtained results of the studies on the hidden parameters ϕ_u and $m(\tilde{G})$ and shows to which extend this Simplified Model can exclude certain regions of the SUSY phase space.

7.1 Event Selection

As already mentioned in section 5.3 the setup of this Simplified Model and the corresponding signal grid is very similar to that in [15]. Due to this fact the analysis of the Simplified Model in this thesis adopts the criteria of event selection from [15] and [82], respectively. As a consequence, the following section will describe and summarise the event selection and as it is implemented for this thesis while additional information can be found ibid..
Due to the fact that physics events of this Simplified Model produce an opposite-charged pair of charginos decaying via stau sparticles to tau leptons (c. f. fig. 5.4 in section 5.3), the analysis of this grid requires events to have at least two hadronically decaying tau leptons of which at least two are combinable to an opposite-sign pair. Since neither other leptons nor jets are expected, events with light leptons (i. e. electrons and muons) and/or jets present are rejected. These basic criteria give a first impression of how the event selection will look like motivated by the pure signal topology.
Since different physics objects can be reconstructed with different efficiencies a procedure called 'overlap removal' is applied (c. f. section 7.1.2) before the actual event selection. During overlap removal objects which can look similar to the detector and are reconstructed close to each other and thus tend to be mixed up in identification are removed from the event. The input for the overlap removal procedure are objects referred to as baseline objects while objects surviving overlap removal and fulfilling tighter quality criteria are referred to as signal objects.
Before the actual event selection can start, more basic requirements to the event have to be accounted for. At the very beginning basic event quality criteria are summed up in an selection step referred to as 'event cleaning' (c. f. section 7.1.3). This step contains requirements which are so rudimentary that every event has to fulfil them independently of the actual analysis requirements.
After overlap removal is applied and events surviving the 'event cleaning' step become subject to the actual event selection in form of a 'cut-flow'. Due to several effects listed in section 7.1.5, reweighting

and scaling factors are applied to the signal samples and their events.

7.1.1 Object Definitions

In this section the physics objects required for this analysis and their way of reconstruction in the ALTAS detector are briefly summarised.

Jets

Jets are reconstructed using the anti-k_t jet algorithm seeded with topological clusters and a distance parameter $R = 0.4$ as already described in section 3.3.1. Baseline jets are required to have $p_T > 20\,\text{GeV}$ and $|\eta| < 4.5$

Tau Leptons

The reconstruction of hadronically decaying tau leptons is performed as described in section 3.3.3 using the BDT method to compute the 'tauID'. Baseline tau objects are required to have $p_\text{T} > 20\,\text{GeV}$ and to lie within $|\eta| < 2.5$. Furthermore only taus being reconstructed in 1-prong or 3-prong mode and having a combined charge of their tracks of $\pm 1e$ are considered. For signal taus it is required that at least one fulfils the 'tight' BDT requirement as descried ibid..

Missing Transverse Energy and Light Leptons

The reconstruction of $\not{E}_\text{T}$ is performed as described in section 3.3.2 with specifications listed in [82]. Since events with light leptons present are vetoed, the reconstruction of electrons and muons is not described here. Information on this can be found ibid..

7.1.2 Overlap Removal

The procedure of overlap removal is supposed to make sure that physics objects in an event are correctly and clearly identified by removing close-by objects which are likely to be reconstructed from the same input but are of the wrong type. An example for such a case is a jet reconstructed near an electron. Since electron and jet reconstruction are both seeded from calorimeter clusters but electron reconstruction is easier and more efficient, the jet is rejected due to a higher probability of being a fake. The steps of overlap removal are applied consecutively in the order given below:

1. If any two baseline electrons lie with $\Delta R < 0.1$ the electron with the lower energy E_T is rejected. This prevents double counting of electrons due to using the same ECAL cluster twice as a seed.

2. Baseline jets overlapping with baseline electrons within $\Delta R < 0.2$ are rejected since jet reconstruction is seeded with the same topological cluster as electron reconstruction while the fake rate for the latter is much lower.

3. Baseline electrons which are within $\Delta R < 0.4$ of baseline jets that survived the step before are rejected. Since constituents of jets—especially of b-jets—can decay (semi-)leptonically electrons near 'good' jets are rejected since they belong to the jet.

4. Baseline muons lying within $\Delta R < 0.4$ of baseline jets are removed for the same reason as baseline electrons in the point above.

5. Baseline electrons and muons overlapping within $\Delta R < 0.1$ are both removed.

6. Baseline muons overlapping within $\Delta R < 0.05$ are both rejected.

7. If the invariant mass of any two opposite-sign baseline electrons is less than 12 GeV then both electrons are rejected. This step is performed to suppress electrons originating from leptonic decays of neutral mesons like the $\Upsilon(4s)$.

8. If the invariant mass of any two opposite-sign baseline muons is less than 12 GeV then both muons are rejected for the same reason as baseline electrons from above.

9. If the distance between a baseline electron and a baseline tau is $\Delta R < 0.2$ the tau is rejected which is due to the fact that taus are seeded from the same clusters as electrons and are likely to look like electrons. Since the fake rate for electrons is much lower than for taus the taus are rejected.

10. If the distance between a baseline muon and a baseline tau is $\Delta R < 0.2$ the tau is rejected. This point is fostered by the same argument as in the electron case.

11. If the distance between a baseline jet and a baseline tau is $\Delta R < 0.2$ the jet is rejected. Since jets can look like hadronically decaying taus but a positively identified tau is less likely to a be a fake than a jet, the jet is rejected.

12. If the invariant mass of any two opposite-sign baseline taus is less than 12 GeV both taus are rejected. Since heavy neutral mesons can decay into a pair of tau leptons as well the same argument as for electrons and muons holds in this case.

After applying all these steps on the list of reconstructed physics objects, the event is ensured to contain as many properly reconstructed and correctly identified objects as possible. With this basis given, the selection of events can begin.

7.1.3 Event Cleaning

The first step in selecting proper events is to sort out events which fail overall event quality criteria beyond the actual selection of events of interest. This step is called 'event cleaning' and consists of several quality requirements which have to be met:

- The primary vertex of the event has to be associated with at least five tracks in order to make sure the event is not a pile-up event.

- A 'bad jet veto' is applied which means the event must not contain a jet failing the minimal jet quality criteria which are described in detail in [82].

- A 'LAr veto' is applied which refers to problems with the liquid argon calorimeter of the detector. The LAr veto is supposed to block events which contain tracks pointing towards damaged or noisy regions of the calorimeter. Those regions are determined and marked during the time of operation of the ATLAS experiment. To ensure a proper comparison between data and simulated events this criterion has to be applied to MC samples although the virtual detector is not affected by this technical issue.

- Events containing one or more 'bad muons' are vetoed. A muon is tagged as 'bad' when it fails to fulfil the minimal muon quality criteria described ibid..

- A 'cosmic veto' is applied to suppress events containing objects which are not associated to the primary vertex but are of cosmic origin like cosmic muons. Such events can be identified by tracks not pointing towards the centre of the ATLAS detector but anywhere else.

7.1.4 Triggers and Trigger Strategy

As already mentioned in the introductory part of this section, this analysis requires a signal event to contain at least two (hadronically decaying) tau leptons. Since a SUSY signal event like the ones studied here is further characterised by large amounts of missing energy due to two neutrinos and two undetected LSPs a combination of a di-tau trigger and a $\not{E}_{\mathrm{T}}$-trigger is chosen to select events. While the di-tau trigger is fired when detecting at least two taus with minimum transverse momenta of 29 GeV and 20 GeV, the $\not{E}_{\mathrm{T}}$-trigger needs at least 80 GeV to fire. For both triggers higher offline thresholds have to be exceeded in order for them to be in their plateau of efficiency (c. f. [82]). The trigger requirements are summarised in table 7.1. To achieve a wider coverage of parameter space both triggers are combined

Trigger object	Trigger item	Offline thresholds
2 taus	EF_tau29Ti_medium1_tau20Ti_medium1	$p_{\mathrm{T}}^{\mathrm{leading}} > 40\,\mathrm{GeV}$, $p_{\mathrm{T}}^{\mathrm{subleading}} > 25\,\mathrm{GeV}$
$\not{E}_{\mathrm{T}}$	EF_xe80tc1cw	$\not{E}_{\mathrm{T}} > 150\,\mathrm{GeV}$

Table 7.1: Overview of the triggers implemented in the analysis of the Chargino-Stau grid. For both triggers the corresponding physics objects, the ATLAS-internal nomenclature and the necessary offline threshold criteria are listed.

via a logical OR. This means events which fired the $\not{E}_{\mathrm{T}}$-trigger and fulfil its offline threshold condition only need at least two taus with $p_T > 20\,\mathrm{GeV}$ (i. e. the taus fulfil the baseline selection criteria) and not necessarily the fired di-tau trigger and the corresponding harder threshold cuts to be selected.
A matching of online taus from the trigger to offline tau objects is performed according to [82].

7.1.5 Reweighting and Scaling

Several effects require scaling of full MC samples or reweighting of single events. In this section reweighting refers to event specific weights applied due to certain event characteristics. Scaling refers to the application of a scale factor to all events of a MC sample due to a certain MC sample characteristic.

Pile-Up Reweighting

The Monte Carlo samples produced as signal events for this analysis are generated with an average number of proton-proton interactions per bunch crossing $\langle\mu\rangle$. Since for data samples this number varies for each period of data taking the pile-up effects in MC are reweighted such that their pile-up distributions match the pile-up observed in data. In order to achieve this the combined pile-up distribution of the data taking periods to which the produced MC is supposed to match is compared to the pile-up distribution in MC. According to the differences the MC events are reweighted.

TauID and Trigger Reweighting

In principle the way the tauID is generated from the BDT method described in section 3.3.3 can differ for MC events and data due to imperfect modelling of the MC truth-level physics and the virtual detector with respect to reality. In a similar way the trigger system is not equally described in data and MC. To

account for these deviations reweighting procedures are developed by the corresponding working groups of the ATLAS collaboration.
Since the MC signal samples of this analysis are generated with the fast simulation tool AFII (c. f. section 4.1.2) for which neither of these reweighting factors are available yet, no reweighting for tauID or trigger effects is applied.

Luminosity Scaling

All MC samples used in this analysis just contain 20,000 events. Since they are assumed to be recorded as a pure set of events of the full ATLAS data set of size $\mathcal{L} = 20.68\,\text{fb}^{-1}$ in integrated luminosity—which is orders of magnitude larger—scaling is necessary. By dividing the number of events in each produced MC sample by the production cross section it is produced with[1] the integrated luminosity the sample corresponds to can be derived. Scaling this sample luminosity to the target luminosity of $\mathcal{L} = 20.68\,\text{fb}^{-1}$ yields the scaling factor for the MC sample which is applied to all of the sample's events. A short example for the grid point $m\left(\tilde{\chi}_1^{\pm}\right) = 520\,\text{GeV}$, $m\left(\tilde{\tau}_1\right) = 300\,\text{GeV}$ can clarify this procedure:

$$\mathcal{L}_{\text{target}} = 20.68\,\text{fb}^{-1} \tag{7.1}$$

$$n_{\text{events}} = 20000 \tag{7.2}$$

$$\sigma_{\text{prod.}} = 3.44\,\text{fb} \tag{7.3}$$

$$\Rightarrow \mathcal{L}_{\text{sample}} = \frac{n_{\text{events}}}{\sigma_{\text{prod.}}} = 5813.95\,\text{fb}^{-1} \tag{7.4}$$

$$\Rightarrow a = \frac{\mathcal{L}_{\text{target}}}{\mathcal{L}_{\text{sample}}} = 3.56 \times 10^{-3}. \tag{7.5}$$

7.1.6 Signal Region Definition

After pre-selecting the physics objects and performing overlap removal, each event is required to contain at least two baseline taus and no further light leptons (so-called 'lepton veto'). At least one of the taus has to fulfil the 'tight' reconstruction requirement of the BDT method (c. f. section 3.3.3). Furthermore two of the present taus have to form an opposite-charge-sign pair. The applied trigger strategy is described in section 7.1.4 while the corresponding offline thresholds are displayed in table 7.1. For the case of event selection by the di-tau trigger, matching of the offline taus to the online trigger tau objects is performed. In addition to these criteria, further event requirements are part of the cut flow which are summarised as 'Signal definition':

- **Jet veto:** The event is required to have no signal jets. This criterion is expected to suppress large amounts of $t\bar{t}$ and single-top background events due to those backgrounds being the ones with highest jet production (with respect to e. g. the DiBoson background).

- Z **veto:** The event is rejected if the invariant mass of the signal tau pair is within 10 GeV of the Z^0 mass: $|m_{\tau^+\tau^-} - 81\,\text{GeV}| < 10\,\text{GeV}$. Since in $Z^0 \rightarrow \tau^+\tau^-$ decays the neutrinos from the tau decays prohibit an exact reconstruction of the Z^0 mass, the value deviates from the true value. The value used here is adopted from [82] where it is obtained by fitting a Gaussian distribution to the invariant mass distribution.

[1] the production cross section is derived by the MC generator

- $\not{E}_{\mathrm{T}}$ **cut:** An explicit requirement on the missing transverse energy is made to account for a minimal amount of $\not{E}_T$ in events that where selected by the di-tau trigger. For $\not{E}_T$-triggered events this cut is redundant: $\not{E}_T > 40\,\mathrm{GeV}$.

- **'Stransverse' mass cut:** The 'stransverse' mass m_{T2} (c. f. the next paragraph of this section) is to be $> 90\,\mathrm{GeV}$. In the case of more than two signal taus present in an event, m_{T2} is calculated for all possible pairs of taus and the largest value is chosen.

The 'Stransverse' Mass Variable

The so-called 'stransverse' mass[2] is a variable developed for searches of new physics like SUSY in 1999 by Lester and Summers [83]. It is designed in analogy to the transverse mass variable but with more specialised features. The following passage briefly summarises the basic concept of the stransverse mass M_{T2}.
The transverse mass variable developed by the UA1 collaboration can provide a lower bound for the mass of a heavy particle that decays into a massive visible and massless invisible particle e. g. the W boson in a $W \to e + \nu_e$ leptonic decay. It is defined as

$$m_{\mathrm{T}}^2 = 2(E_{\mathrm{T}}^e \not{E}_{\mathrm{T}} - \mathbf{p}_{\mathrm{T}}^e \cdot \not{\mathbf{p}}_{\mathrm{T}}) \tag{7.6}$$

with $\not{E}_{\mathrm{T}}^2 \equiv \not{\mathbf{p}}_{\mathrm{T}}^2$ and the superscript e denoting the properties of an electron (without loss of generality). Measuring m_{T}^2 for many $W \to e + \nu_e$ decays yields a lower bound for the W mass: $m_{\mathrm{T}}^2 \leq m_W^2$.
Inspired by such a variable the design of m_{T2} is supposed to yield a similar lower bound for the mass of particles that are pair-produced and decay via a massive detectable particle and a potentially massive invisible particle. The challenge lies within the fact that for decays of such particles only the vector sum of the missing momenta of the two invisible particles can be calculated and not each contribution on its own (for the reconstruction/calculation of the missing momentum or energy, respectively, at the ATLAS experiment c. f. 3.3.2). As a consequence the transverse mass of such a particle cannot be calculated. Without loss of generality the considered decay is $\tilde{\tau}_1^{\pm} \to \tau^{\pm} + \tilde{G}$ with the gravitino being invisible to the detector and of kinematically allowed mass. The stau mass can be calculated from the known momenta via

$$m_{\tilde{\tau}}^2 = m_{\tau}^2 + m_{\tilde{G}}^2 + 2(E_{\mathrm{T}\tau} E_{\mathrm{T}\tilde{G}} \cosh \Delta\eta - \mathbf{p}_{\mathrm{T}\tau} \cdot \mathbf{p}_{\mathrm{T}\tilde{G}}), \tag{7.7}$$

with $E_{\mathrm{T}} = \sqrt{\mathbf{p}_{\mathrm{T}}^2 + m^2}$ and $\Delta\eta$ the difference in rapidity[3] between the tau and the gravitino. Taking $\cosh \Delta\eta \geq 1$ this equation can be rewritten with the transverse mass definition:

$$m_{\tilde{\tau}}^2 \geq m_{\mathrm{T}}^2(\mathbf{p}_{\mathrm{T}\tau}, \mathbf{p}_{\mathrm{T}\tilde{G}}) \equiv m_{\tau}^2 + m_{\tilde{G}}^2 + 2(E_{\mathrm{T}\tau} E_{\mathrm{T}\tilde{G}} - \mathbf{p}_{\mathrm{T}\tau} \cdot \mathbf{p}_{\mathrm{T}\tilde{G}}). \tag{7.8}$$

This expression now is a transverse mass definition valid for arbitrary masses of the invisible particle. However, the exact calculation of eq. (7.8) for an event containing two $\tilde{\tau}_1^{\pm}$ decays requires information on the momenta of both invisible gravitinos $\tilde{G}_a$ and $\tilde{G}_b$ which is not accessible since the experiment can only determine the total missing momentum vector:

$$\not{\mathbf{p}}_{\mathrm{T}} = \mathbf{p}_{\mathrm{T}\tilde{G}_a} + \mathbf{p}_{\mathrm{T}\tilde{G}_b}. \tag{7.9}$$

[2] 'Stransverse' is a neologism formed from 'transverse' which is extended by the Supersymmetry prefix 's' to indicate the variable's original purpose of detecting SUSY sparticles
[3] $\eta = \frac{1}{2} \ln [(E+p_z)/(E-p_z)]$

Under the assumption that both gravitino momenta are measurable eq. (7.8) could be used to estimate both stau masses via

$$m_{\tilde{\tau}}^2 \geq \max\left\{m_{\mathrm{T}}^2(\mathbf{p}_{\mathrm{T}\tau^+}, \mathbf{p}_{\mathrm{T}\tilde{G}_a}),\ m_{\mathrm{T}}^2(\mathbf{p}_{\mathrm{T}\tau^-}, \mathbf{p}_{\mathrm{T}\tilde{G}_b})\right\}. \tag{7.10}$$

However, due to the fact that the exact splitting in eq. (7.9) remains unknown, the strongest possible statement is

$$m_{\tilde{\tau}}^2 \geq M_{\mathrm{T2}}^2 \equiv \min_{\not{\mathbf{p}}_1+\not{\mathbf{p}}_2=\not{\mathbf{p}}_{\mathrm{T}}}\left[\max\left\{m_{\mathrm{T}}^2(\mathbf{p}_{\mathrm{T}\tau^+}, \not{\mathbf{p}}_{\mathrm{T}}),\ m_{\mathrm{T}}^2(\mathbf{p}_{\mathrm{T}\tau^-}, \not{\mathbf{p}}_{\mathrm{T}})\right\}\right]. \tag{7.11}$$

The minimisation is performed over all possible 2-momenta, $\not{\mathbf{p}}_{1,2}$, such that they sum gives the observed missing transverse momentum $\not{\mathbf{p}}_{\mathrm{T}}$. The lower bound becomes an exact equality when in both decays the tau and the gravitino are produced at the same rapidity η (the stau sleptons can differ in rapidity) and further the following condition is fulfilled:

$$\left(\frac{\mathbf{p}_{\mathrm{T}\tau^+}}{E_{\mathrm{T}\tau^+}} - \frac{\mathbf{p}_{\mathrm{T}\tilde{G}_a}}{E_{\mathrm{T}\tilde{G}_a}}\right) \propto \left(\frac{\mathbf{p}_{\mathrm{T}\tau^-}}{E_{\mathrm{T}\tau^-}} - \frac{\mathbf{p}_{\mathrm{T}\tilde{G}_b}}{E_{\mathrm{T}\tilde{G}_b}}\right). \tag{7.12}$$

In order for M_{T2} to well approximate the true particle mass, a reasonable number of events close to its maximum value are required. Given enough statistics this requirement should be fulfilled in most analyses.
In this analysis M_{T2} is calculated for the opposite-sign tau pair in order to ensure that they have arisen from the stau sleptons which have been produced in the chargino decays. Hence, the M_{T2} criterion is expected to suppress large amounts of SM background but keep most SUSY events.
Additional information on the properties of M_{T2} can be found in [83] while [84] provides information on how to utilise this variable in less constrained ways than the two-body decays described here.

7.1.7 Cut Flow Results

By consecutively applying all the selection criteria mentioned above, a cut flow arises for which some exemplary results are displayed in table 7.2. In this notation 'Event Cleaning' refers to the steps described in section 7.1.3 while 'Trigger' denotes the applied trigger strategy from section 7.1.4. The '2 taus' step simply requires the event to have at least two signal taus. 'Trigger matching' and 'Trigger plateaus' refer to the corresponding procedure described in section 7.1.4 and the threshold requirements for the triggers that fired, respectively. The 'Lepton veto' requires the event to contain neither signal electrons nor signal muons while '1 tau' requires the leading tau—i. e. the signal tau with the highest value of p_{T}—to fulfil the 'tight' quality criterion of the tau identification algorithm. Finally 'OS' requires the event to have a pair of opposite-sign signal taus. The last cut flow step defines the signal region as described in section 7.1.6. Since all events are scaled and/or reweighted, respectively, the given numbers of events surviving the selection steps is no more of integer type. In order to better understand the results of the cut flow three exemplary steps are discussed in more detail. The line of argumentation is supported by plots of the crucial variables which are responsible for the results and a brief qualitative discussion. Since this analysis heavily relies on the abundance and properties of tau leptons the selected variables are the leading tau transverse momentum $p_{\mathrm{T}}^{\tau_1}$, the amount of missing transverse energy $E_{\mathrm{T}}^{\mathrm{miss}}(\equiv \not{E}_{\mathrm{T}})$, the maximum value of all possible combinations to form m_{T2} from a pair of taus $m_{\mathrm{T2}}^{\tau\tau}$ and the tau multiplicity.
To be able to compare one selection step to another the first set of presented distributions is after the step of 'event cleaning':

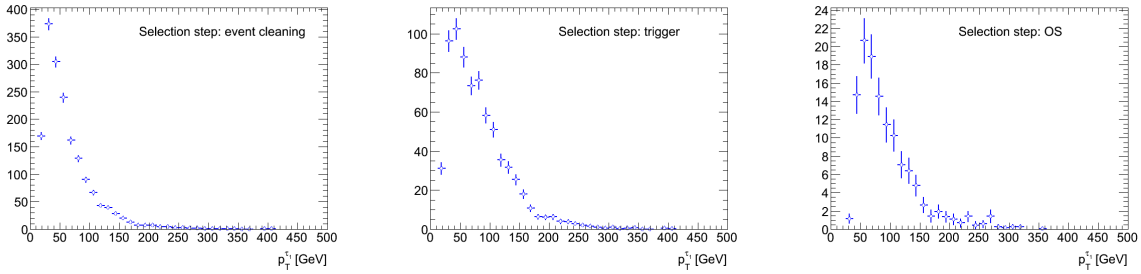

Figure 7.1: Chargino-Stau grid cutflow diagrams, grid point 100/221, $p_{\mathrm{T}}^{\tau_1}$

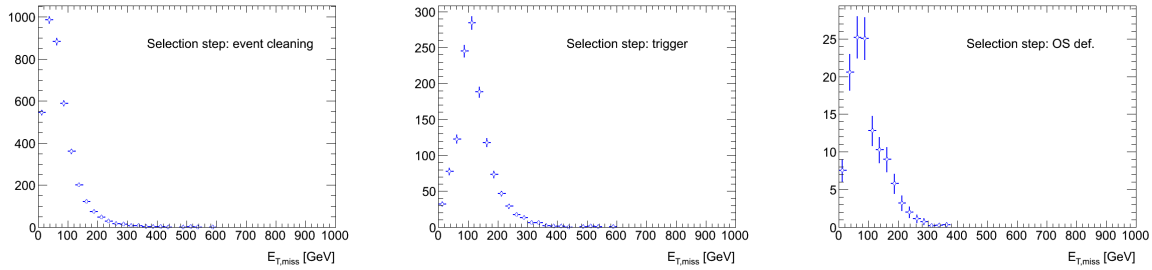

Figure 7.2: Chargino-Stau grid cutflow diagrams, grid point 100/221, $E_{\mathrm{T,\,miss}}$

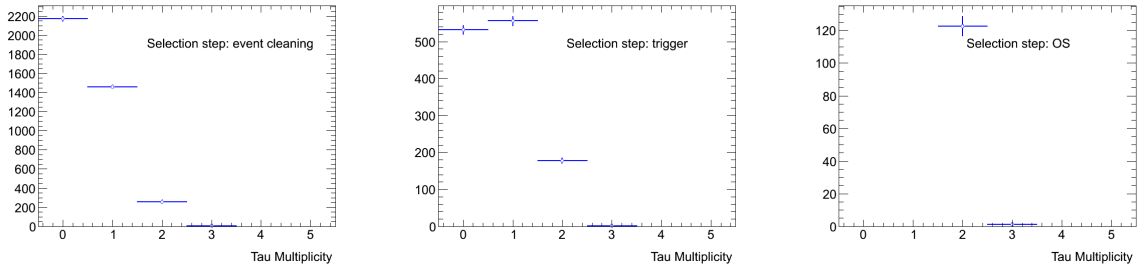

Figure 7.3: Chargino-Stau grid cutflow diagrams, grid point 100/221, tau multiplicity

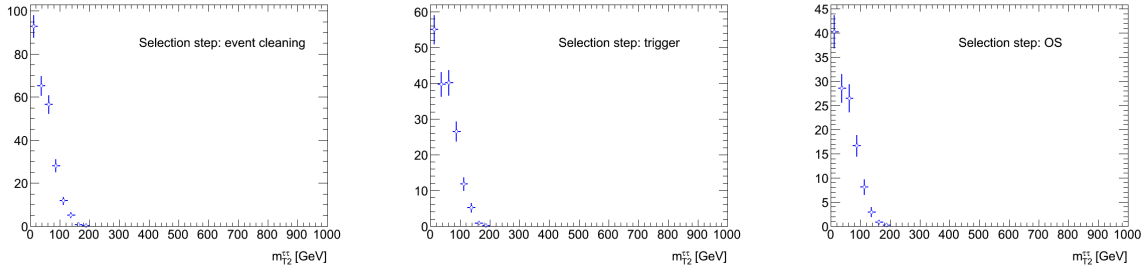

Figure 7.4: Chargino-Stau grid cutflow diagrams, grid point 100/221, $m_{\mathrm{T2}}^{\tau\tau}$

grid point	$m(\tilde{\tau}_1) = 100\,\text{GeV}$ $m(\tilde{\chi}_1^{\pm}) = 221\,\text{GeV}$	$m(\tilde{\tau}_1) = 300\,\text{GeV}$ $m(\tilde{\chi}_1^{\pm}) = 520\,\text{GeV}$	$m(\tilde{\tau}_1) = 690\,\text{GeV}$ $m(\tilde{\chi}_1^{\pm}) = 700\,\text{GeV}$
Cut	# surviving events (scaled)		
No cut	3994.13	71.1908	11.91
Event cleaning	3889.3	68.8239	11.5119
Trigger	1266.66	50.747	10.3507
2 taus	179.192	7.46082	1.35343
Trigger matching	178.395	7.34976	1.30903
Trigger plateaus	134.711	6.39589	1.22951
Lepton veto	134.231	6.35533	1.21568
1 tau tight	125.07	5.82552	1.10363
OS	765.53	5,69917	1.08233
Signal definition	12.018	1.71184	0.458819

Table 7.2: For three different points on the Chargino-Stau signal grid the number of events after each step of the cut flow is listed. Due to the application of several scaling and reweighting factors (c. f. section 7.1.5) the event numbers are no more of integer type.

As one can see in table 7.2 for all three grid points only very few events are lost in the selection step of 'event cleaning'. Since the next step requires the event to fulfil the trigger logic implemented, it is helpful to look at variables which are probed by the trigger system. The two triggers which are used in this analysis require an event to have two tau leptons with certain transverse momentum ($p_{\text{T}}^{\tau_1} > 29\,\text{GeV}$, $p_{\text{T}}^{\tau_2} > 20\,\text{GeV}$) or a certain amount of missing transverse energy ($\not{E}_{\text{T}} > 80\,\text{GeV}$).
In case of the 100/221 grid point only $\approx 33\%$ of all events survive the 'Trigger' requirement while for the other two grid points $\approx 97\%$ of the events survive both selection steps. This observation can be explained by looking at the distributions that describe the parameters that are probed by the triggers. While for all three grid points both the $\not{E}_{\text{T}}$ and the $p_{\text{T}}^{\tau_1}$ distributions do not change much in shape—the majority of events always fulfils both requirements—this is not the case the distribution of the tau multiplicity. Here the number of events having one (zero) tau lepton is decreased to $\approx 25\%$ ($\approx 39\%$) of the selection step before for the 100/221 grid point while for 300/520 it is still $\approx 66\%$ ($\approx 78\%$) or $\approx 88\%$ ($\approx 92\%$) for 690/700, respectively. These numbers suggest that more events fail to fire the di-tau trigger for the 100/221 grid point than for the other two.

In order to understand the high losses from the second-to-last to the last selection step ($\approx 1.7\%$ surviving events for the grid point 100/221, $\approx 30\%$ for 300/520 and $\approx 42.4\%$ for 690/700) a look at certain distributions after the step 'OS' is helpful. Among the requirements the last step in the selection chain,the definition of the signal region, makes to an event is $\not{E}_{\text{T}} > 40\,\text{GeV}$ and $m_{\text{T2}}^{\tau\tau} > 90\,\text{GeV}$. The distributions before the last step in the cut flow are depicted in figs. 7.2, 7.6 and 7.10 and figs. 7.4, 7.8 and 7.12, respectively.

When looking at those distributions it is clearly observable that there are still some events which do not pass the $\not{E}_{\text{T}} > 40\,\text{GeV}$ criterion. Since only events that fired the $\not{E}_{\text{T}}$-trigger require a certain amount of $\not{E}_{\text{T}}$ at this point of the selection it is likely that those events were triggered by the di-tau trigger. The $\not{E}_{\text{T}}$ and $m_{\text{T2}}^{\tau\tau}$ distributions give the impression that most events do not fulfil the $\not{E}_{\text{T}}$ and $m_{\text{T2}}^{\tau\tau} > 90\,\text{GeV}$ requirement and that the latter is the most radical criterion.
After this short explanation of the event selection of this analysis the study of its results can be approached. However, before an introduction to the SM background physics processes is given followed

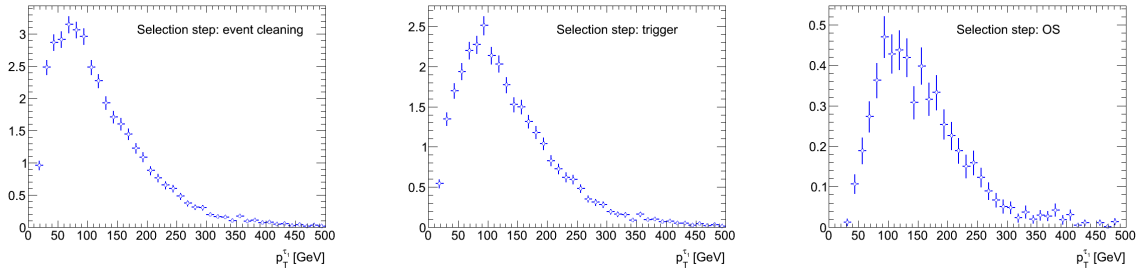

Figure 7.5: Chargino-Stau grid cutflow diagrams, grid point 300/520, $p_{\mathrm{T}}^{\tau_1}$

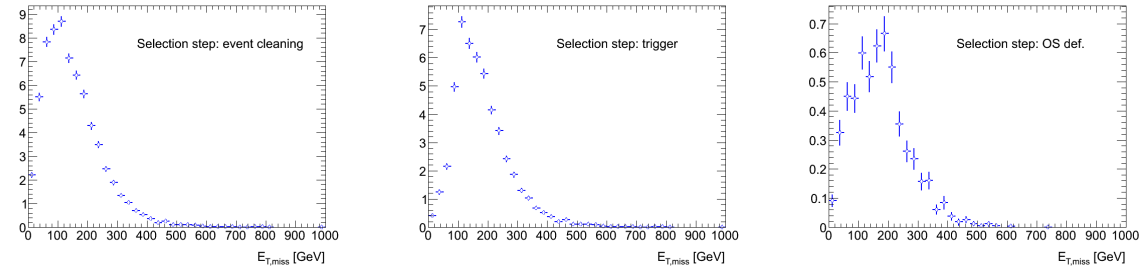

Figure 7.6: Chargino-Stau grid cutflow diagrams, grid point 300/520, $E_{\mathrm{T,\,miss}}$

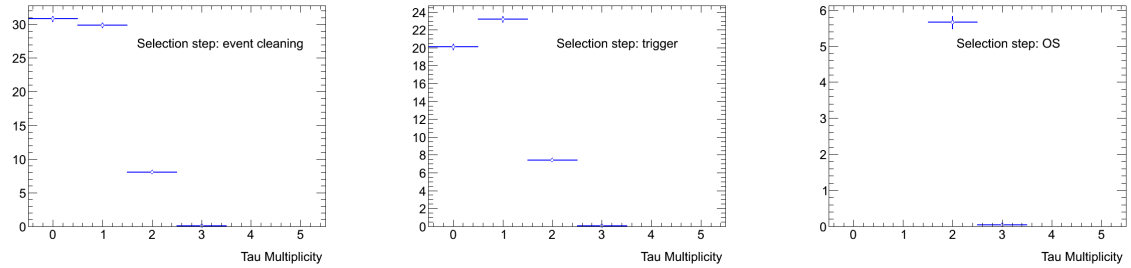

Figure 7.7: Chargino-Stau grid cutflow diagrams, grid point 300/520, tau multiplicity

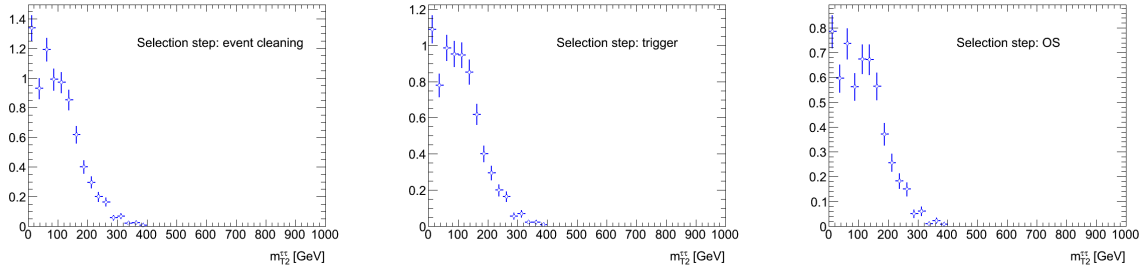

Figure 7.8: Chargino-Stau grid cutflow diagrams, grid point 300/520, $m_{\mathrm{T2}}^{\tau\tau}$

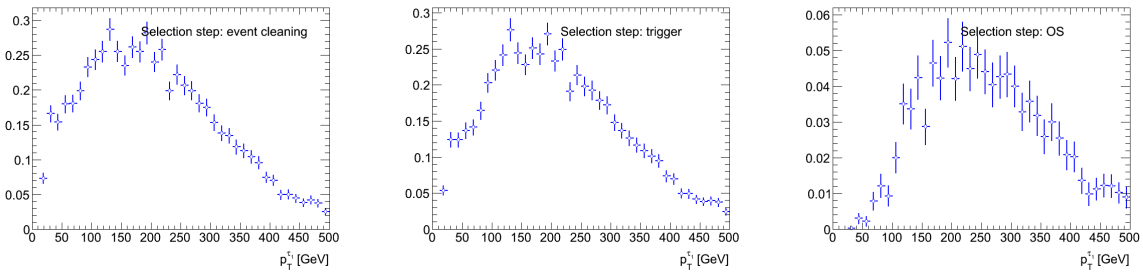

Figure 7.9: Chargino-Stau grid cutflow diagrams, grid point 690/700, $p_{\mathrm{T}}^{\tau_1}$

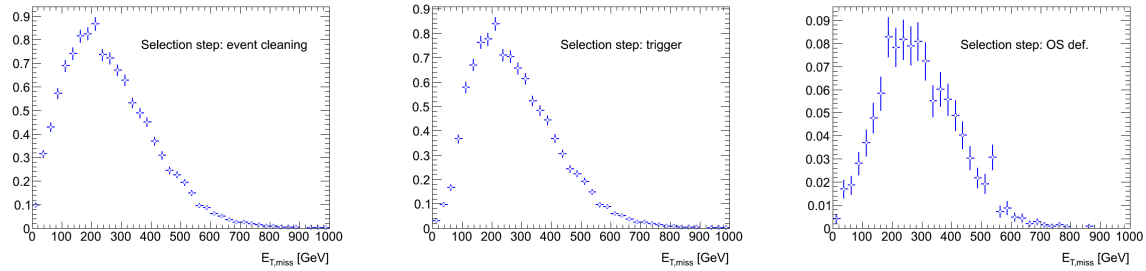

Figure 7.10: Chargino-Stau grid cutflow diagrams, grid point 690/700, $E_{\mathrm{T,\,miss}}$

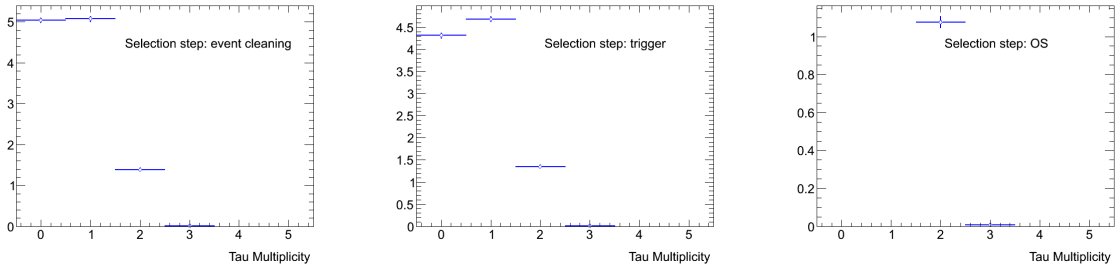

Figure 7.11: Chargino-Stau grid cutflow diagrams, grid point 690/700, tau multiplicity

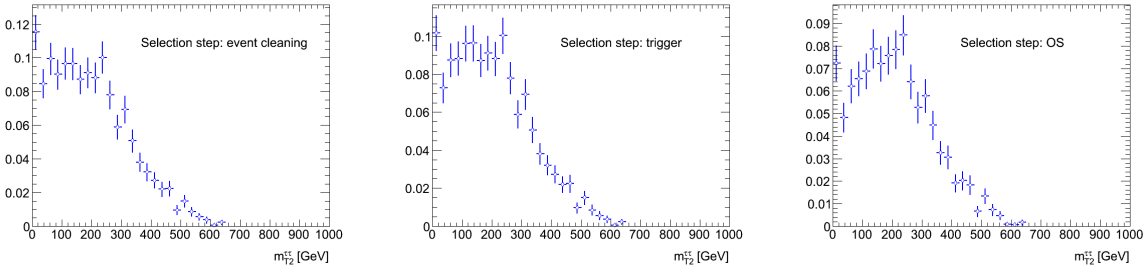

Figure 7.12: Chargino-Stau grid cutflow diagrams, grid point 690/700, $m_{\mathrm{T2}}^{\tau\tau}$

by a short summary of the systematic uncertainties considered in this analysis.

7.2 Standard Model Backgrounds and Systematic Uncertainties

Most search for BSM physics suffers from huge SM backgrounds which strongly dominate both data and MC samples. Since every analysis is sensitive to different SM backgrounds, this section will introduce and describe the backgrounds considered in this analysis. Furthermore several sources of systematic uncertainties will be introduced and discussed.
Both the selection of background categories and the considered systematic uncertainties are taken from [82] whereas for the latter only those that are applicable to this analysis are considered.

7.2.1 Standard Model Background Sources

For a di-tau analysis like this, one of the most dominant background contributions (around 75% to 80% [82]) arises from events with fake taus. In those cases, one or more jets are misidentified as tau leptons and thus introduce background events. The largest contribution in terms of events with fake taus stems from QCD multi-jet events and W+Jets events. In the first case both jets from the hard process—the primary interaction—are misidentified as tau leptons while the required amount of $\not{E}_{\mathrm{T}}$ originates from instrumental effects. Although the QCD multi-jet events with two fake taus and a lot of $\not{E}_{\mathrm{T}}$ are rather rare the large production cross section makes them a huge source of background.
The other primary source of fake tau background events are W+Jets events. In this case one tau is a real tau originating from the W decay while the other tau is a misidentified jet. Furthermore the missing transverse energy of W+Jets events faking real di-tau events is real in contrast to the QCD multi-jet case. Here the $\not{E}_{\mathrm{T}}$ originates from both the W decay and the τ decay due to the undetected neutrinos which are involved.
Since fake taus are badly modelled in MC, both fake tau background sources are not estimated from simulation but from data using the $ABCD$-method where the background contribution in the signal region is extrapolated from signal-free control regions. Due to their very similar signatures both backgrounds are combined into one estimated background further referred to as 'fake taus'. Additional details on the calculation method and its statistical and systematic uncertainties can be found in [82].
Further sources of background events are Z+Jets, $t\bar{t}$, single top and di-boson events. The sources Z+Jets, $t\bar{t}$ and single top are estimated by applying a similar $ABCD$-method as for the fake tau background but on MC level. Furthermore both top-quark backgrounds are combined into one background source referred to as 'top'. The di-boson background contribution is fully estimated from MC.
Again more detailed information on the various background sources, their way of estimation and validation can be found ibid..
The total contribution of all background sources in units of scaled events together with their statistical (first uncertainty number) and systematical (second uncertainty number) uncertainties are adopted from [82] and summarised in table 7.3.

7.2.2 Systematic Uncertainties

In general the sources of systematic uncertainties and their correlations can be numerous. Since in the time frame of this thesis only very limited studies of systematic uncertainties are possible this section will introduce and describe the few which are considered in this analysis and how they are derived. All systematic uncertainties taken into account in this analysis are so-called first order uncertainties which

SM process	# events
top	$0.2 \pm 0.5 \pm 0.1$
Z+Jets	$0.28 \pm 0.26 \pm 0.23$
di-boson	$2.2 \pm 0.5 \pm 0.5$
fake tau	$8.4 \pm 2.6 \pm 1.4$
SM total	$11.0 \pm 2.7 \pm 1.5$
data	6

Table 7.3: Summary of the Standard Model background contributions and their statistical and systematic uncertainties. Due to the applied scaling and reweighting factors the given numbers are no more of integer type. Furthermore the number of measured events in data is provided. All numbers are adopted from [82].

means they are assumed to be uncorrelated among each other. Uncertainties of higher order taking possible correlations into account (e. g. a variation of the jet energy scale would in general influence the tau reconstruction efficiency) are neglected.
The general procedure of deriving the contribution of a systematic uncertainty is simple: the source of uncertainty, e. g. the jet energy resolution, is varied within its determined uncertainty which is provided by the corresponding subgroup of the ATLAS collaboration, the analysis is performed again with this one changed parameter and the number of events surviving this analysis is compared to the output of the default analysis. The difference in events surviving the selection with and without the variation of the systematic uncertainty source is the contribution of that particular source. This procedure can be applied to derive the systematic uncertainties of all sources which are due to detector effects. When not described explicitly, the contributions of the systematic uncertainty sources described in the following are derived in this way.
Jet energy resolution – JER: How jets are reconstructed at ATLAS is described in section 3.3.1. This procedure relies on the measurement of energy deposition in the cells of the calorimeter system of the detector. Since the granularity of the cells is finite this energy deposition can only be measured with a finite resolution. By allowing the clusters to fluctuate within this resolution the effect of the JER as a systematic uncertainty can be estimated.
Jet energy scale – JES: Along with the procedure of reconstruction also the recalibration of jets at ATLAS and how this method introduces a systematic uncertainty is described ibid..
$\not{E}_{\mathrm{T}}$ **resolution**: How the 'CellOut' term contributes to the calculation of the missing transverse energy is described in section 3.3.2. Since this term is calculated from calorimeter cell entries it is subject to the finite calorimeter resolution due its finite granularity.
$\not{E}_{\mathrm{T}}$ **scale**: Similar to the JES recalibration the $\not{E}_{\mathrm{T}}$ scale is recalibrated to yield proper values. How this becomes a source of systematic uncertainty is described ibid..
tauID: Why reweighting due to the tauID is necessary and how it is applied is described in section 7.1.5. Since the applied scaling factors come with an uncertainty the application of the reweighting procedure introduces a systematic uncertainty. This uncertainty is only relevant for the background samples since on the signal samples no tauID reweighting is applied.
Tau energy scale – TES: Similar to the systematic uncertainty arising from the recalibration of the energies of jets (JES) and $\not{E}_{\mathrm{T}}$ the tau energy recalibration is another source of systematic uncertainty treated in the same way.
Generator uncertainties: For all MC simulated events uncertainties due to the used generator can be estimated. Since there are several different generators available for different steps of simulating

the physics processes studied (e. g. for calculating the matrix elements, modelling the hadronisation of coloured particles or the shower shape of electromagnetically interacting particles) the systematic uncertainties arising here can be estimated by comparing the same physics processes modelled by different generators. Again this is a systematic uncertainty which is considered only for the backgrounds.
Cross section uncertainties: Since the generated signal samples of this analysis are scaled with respect to their production cross section and the integrated luminosity considered in this analysis (c. f. 7.1.5) uncertainties on the derived production cross sections are relevant. These uncertainties take into account that on generator level the cross section is only derived in leading order of the participating Feynman diagrams while designated tools can account for higher order corrections. Due to time constraints the higher order corrections of the production cross sections are not calculated and the corresponding uncertainties remain zero.
Pile-up: In order do account for pile-up effects which are modelled differently in MC with respect to data reweightings are applied (c. f. section 7.1.5). This reweighting is done by matching the $\langle\mu\rangle$ distribution of MC to that of data without considering the N_{vtx} distributions. To consider possible effects on the $\langle\mu\rangle$ distributions when matching the N_{vtx} distributions and thus effects on the pile-up weights a systematic uncertainty is introduced.
Luminosity: Finally the luminosity measured by the ATLAS experiment is not free of an uncertainty. To account for a possible mis-measurement of the integrated luminosity the ATLAS experiment collected, a fixed uncertainty of 3.9% is assumed and applied to the integrated luminosity used in an analysis to normalise the number of simulated events [82].

7.3 Results

After introducing the structure of the event selection in section 7.1 and the SM backgrounds/systematic uncertainties in section 7.2 the obtained results are presented here. This section is subdivided into parts containing the results for the studies on the two hidden parameters and the results of the full grid study. The latter will be compared to the results obtained in [15, 82].

7.3.1 Hidden Parameter Studies: Chargino Mixing

How mixing in the charged gaugino sector occurs and why it is an intereseting phenomenon to investigate is described in section 5.3. Now that the steps of selecting the final set of events described in section 7.1 are applied to the MC samples produced with varying chargino mixing angles. These samples are produced for fixed values of $m(\tilde{\tau}_1) = 300\,\text{GeV}$ and $m(\tilde{\chi}_1^{\pm}) = 520\,\text{GeV}$ with different values for ϕ_U and ϕ_V, respectively. When referring to the chargino mixing angle from now on the angle ϕ_U is considered. Since both angles are coupled (c. f. section 5.3) ϕ_V takes the values listed in table 7.4 and is not further mentioned.
This part of the analysis is supposed to study the influence of a 'hidden' parameter and decide whether it is truly 'hidden' or rather 'visible' i. e. of any visible influence in other analyses. As a consequence it is useful to have a look at variables that every analysis is sensitive to. Since this thesis studies physics with tau leptons, crucial variables which the experiment can probe are kinematic observables of tau leptons. The two variables selected here are the tau transverse momentum p_{T}^{τ} and the tau pseudo rapidity η_{τ} which are both measurable by the detector itself. If those observables depend on the chargino mixing angle it would have an influence on the efficiencies[4] of analyses involving tau leptons arising

[4] Ehen refering to an analysis's efficiency the ratio of reconstructed events and truth-level events after the full selection is meant. THe efficiency describes how efficient with respect to the true physics happening the reconstruction works.

ϕ_U [°]	ϕ_V [°]
1	3.137
12	6.765
23	12.78
34	36.75
44	44.01

Table 7.4: Due to the correlations between the two mixing angles of the chargino sector of the MSSM, ϕ_V can be calculated according to ϕ_U. This table lists the values ϕ_V takes when varying ϕ_U.

from charged gaugino interactions and would be no more hidden. Figure 7.13 shows the dependencies of the acceptance[5] and efficiency of the different MC samples on the variation of the chargino mixing angle.

As one can see both the distributions of the acceptance and the efficiency are flat within their 1σ-uncertainties. These observations suggest that the chargino mixing angle does neither affect the truth-level physics (described by the acceptance) nor the experimental part of the analysis (described by the efficiency). The fact that both distributions show a constant behaviour under variation of the chargino mixing angle can be understood by looking at the MC generator input:
The generator that is used to simulate the truth-level physics of the events is made subject to several constraints. First of all it is forced to produce pairs of $\tilde{\chi}_1^+ - \tilde{\chi}_1^-$ arising from the primary proton-proton interaction only. Along with the high mass of the $\tilde{\chi}_2^\pm$ this constraint prevents the event from containing the other halves of the chargino doublets and thus from showing possible possible contamination by $\tilde{\chi}_2^\pm$ contributions. Furthermore the $\tilde{\chi}_1^\pm$ is restricted to one decay mode only – the decay $\tilde{\chi}_1^\pm \rightarrow \tilde{\tau}_1^\pm + \nu_\tau$. This constraint prevents effects of the chargino mixing angle on branching ratios and partial decay widths. In summation all these restrictions allow only one particular supersymmetric decay chain which can only change its kinematics due to different sparticle masses while its topology stays invariant.
Things would look rather different if more than one decay mode would be allowed since then the mixing angle would influence the coupling to the different decay products and thus modify the branching ratios and partial decay widths. As a consequence the participating particles would depend on the chargino mixing and thus the overall event topology which is probed by the acceptance.
Besides acceptance and efficiency a variable worth looking at in terms of being influenced by the chargino mixing angle is the production cross section. Although this observable is hard to measure experimentally it is in principle accessible. Since the production cross section of a particular physics process determines how frequently it is produced, it strongly influences the chance of detecting such an event. As a consequence, BSM physics processes with higher production cross sections are more likely to be discovered than those with lower production cross sections. Figure 7.14 shows the dependence of the production cross section for the grid point 300/520 on the chargino mixing angle.
As one can see the production cross section decreases towards higher chargino mixing angles. Since no uncertainties on the cross section are provided by the generator, no error bars are shown to better quantify this statement. The so-called visible cross section—the product of production cross section, acceptance and efficiency—in principle shows a similar behaviour though the statement of a decrease towards higher mixing angles cannot be supported due to the large error bars. However, the observation in the cross section dependence can be explained qualitatively: the chargino mixing controls how

[5] When refering to an analysis' acceptance the ratio of truth-level events before the selection to the truth-level events after all selection steps is meant. The acceptance describes how sensitive an investigated model is towards the selection criteria applied for background suppression

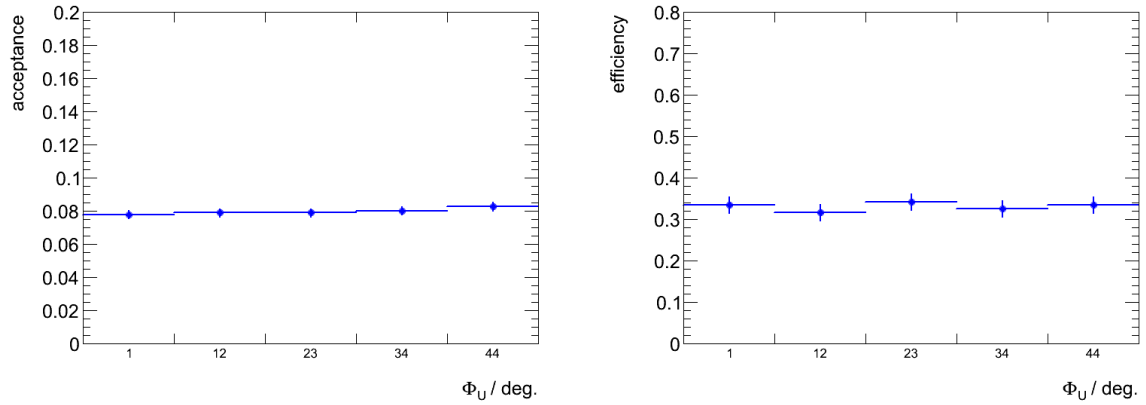

Figure 7.13: Acceptance a (left) and efficiency ϵ (right) under variation of the chargino mixing angle. A small angle corresponds to a 'wino-like' $\tilde{\chi}_1^\pm$ while a higher value of the angle corresponds to high mixing of the wino and higgsino components in the $\tilde{\chi}_1^\pm$. A dependence of either variable with respect to variation of the mixing angle is not visible within the (magnified) error bars.

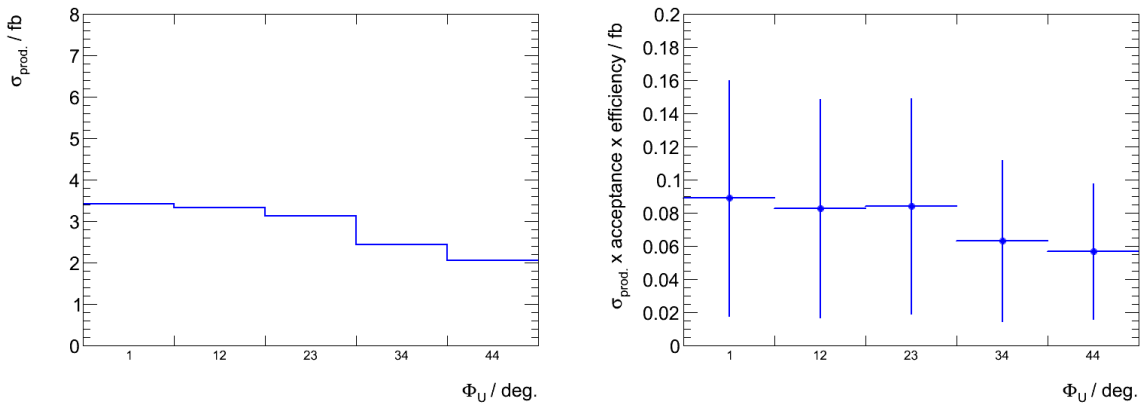

Figure 7.14: $\sigma_{\text{prod.}}$ (left) and $\sigma_{\text{vis.}} = \sigma_{\text{prod.}} \times a \times \epsilon$ (right) under variation of the chargino mixing angle. A small angle corresponds to a 'wino-like' $\tilde{\chi}_1^\pm$ while a higher value of the angle corresponds to high mixing of the wino and higgsino components in the $\tilde{\chi}_1^\pm$. A dependence of the production cross section with respect to variation of the mixing angle is visible while a possible effect on $\sigma_{\text{vis.}}$ is not visible due to the error bars.

'wino-like' or 'higgsino-like' the chargino is. While the wino component of the chargino couples to other particles via an electroweak gauge coupling the higgsino component will couple via a Yukawa coupling – which means its coupling strength is sensitive to the interacting particles' masses. Since the proton's valence quarks u and d are rather low in mass and the chargino mass is not varied for this hidden parameter study it is more likely to produce a pair of charginos when their wino component is higher. As a result the production cross section is slightly higher for lower values of the chargino mixing angle ($\phi_V = 1°$ corresponds to an almost purely 'wino-like' chargino while $\phi_V = 44°$ provides almost maximal mixing of wino and higgsino components).
In a similar way adding the $\tilde{\chi}_2^{\pm}$ to the list of particles produced at the primary vertex is expetected to show some effect on both acceptance and efficiency. Since for $\phi_V = 1°$ the $\tilde{\chi}_1^{\pm}$ is very 'wino-like' the $\tilde{\chi}_2^{\pm}$ is 'higgsino-like'. This would result in the lighter chargino coupling to electroweak gauge bosons preferably while the heavier chargino would prefer Yukawa interactions via a Higgs boson. Since interactions via a Higgs boson can result in chirality flips which would influence the particle's angular behaviour via changes in its helicity, effects on both acceptance and efficiency are to be expected.

7.3.2 Hidden Parameter studies: LSP Mass

In order to get an impression on how a massive LSP would influence the simplified model studied in this chapter, the variation of the gravitino mass as a hidden parameter—though a sparticle mass is more of a pseudo-observable—of the grid is looked into more detailledly. In analogy to section 7.3.1 the observables acceptance, efficiency, prodcution and visible cross section are shown in figs. 7.15 and 7.16.
All four figures do not show any visible dependence on the gravitino mass within their 1σ-error bars (if accessible). For the production cross section this behaviour is expected since this quantity only depends on the chargino coupling and the chargino mass, not on any property of particles further down the decay chain. Since acceptance and efficiency depend on quantities like the amount of missing transverse energy and the tau leptons' momenta the, observation is not as clearly understandable as for the cross sections. Due to conservation of energy and momentum a higher gravitino mass is expected to yield lower momentum tau leptons (from the stau decay) and lower values of $\not{E}_{\mathrm{T}}$ both due to the fact that less energy of the stau is needed to produce the mass of the gravitino. These expectations can be supported by the diagrams shown in figs. 7.17 and 7.18. Here the expected shifts, though only slightly present, in $\not{E}_{\mathrm{T}}$ and p_{T}^{τ} are visible.
However, a possible explanation of the observation in the acceptance and efficiency distributions exists: considering the relatively high mass of the stau slepton at the studied grid point ($m(\tilde{\tau}_1) = 300\,\mathrm{GeV}$) with respect to both the highest value of the gravitino mass ($m(\tilde{G}) = 100\,\mathrm{GeV}$) and the mass of the tau lepton $m(\tau) = 1.777\,\mathrm{GeV}$, the energy passed on to the tau and the gravitino in the decay of the stau is still high enough to produce tau leptons and values of $\not{E}_{\mathrm{T}}$ surviving all selection steps. As a consequence, the expected (and visible) changes in p_{T}^{τ} and $\not{E}_{\mathrm{T}}$ do not affect the distributions of acceptance and efficiency. For observing possible influences on acceptance and efficiency the gravitino mass needs to be closer to the mass of the stau slepton which is a prospect for future studies on this topic.

7.3.3 Full Grid Study

This section presents the results obtained from applying the selection criteria described in section 7.1 on the full signal point grid of this Simplified Model. The results are shown in form of exclusion limits derived by the procedure described in section 4.2. The systematic uncertainties for the SM backgrounds taken into account are adopted from [82] and listed in section 7.2.2. The systematic uncertainties for the signal grid are calculated for each grid point individually and described ibid..

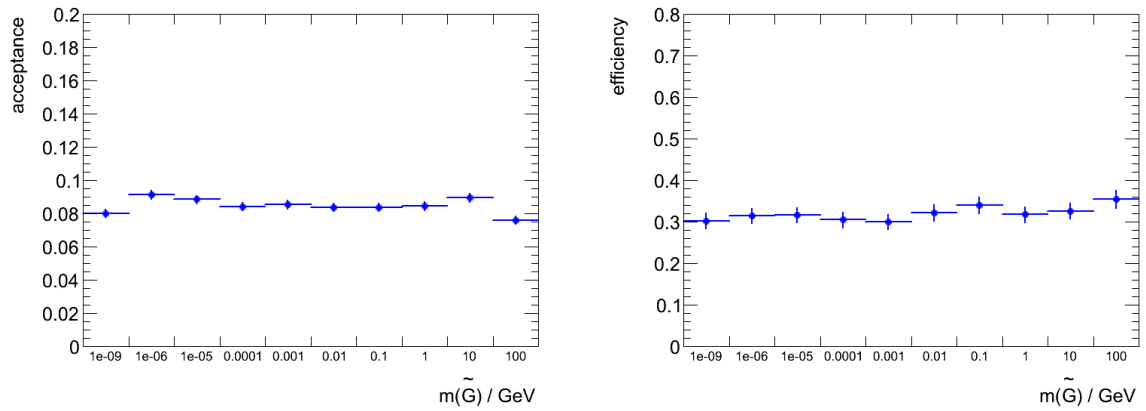

Figure 7.15: Acceptance a (left) and efficiency ϵ (right) under variation of the gravitino mass. A dependence of either variable with respect to variation of the gravitino mass is not visible within the error bars.

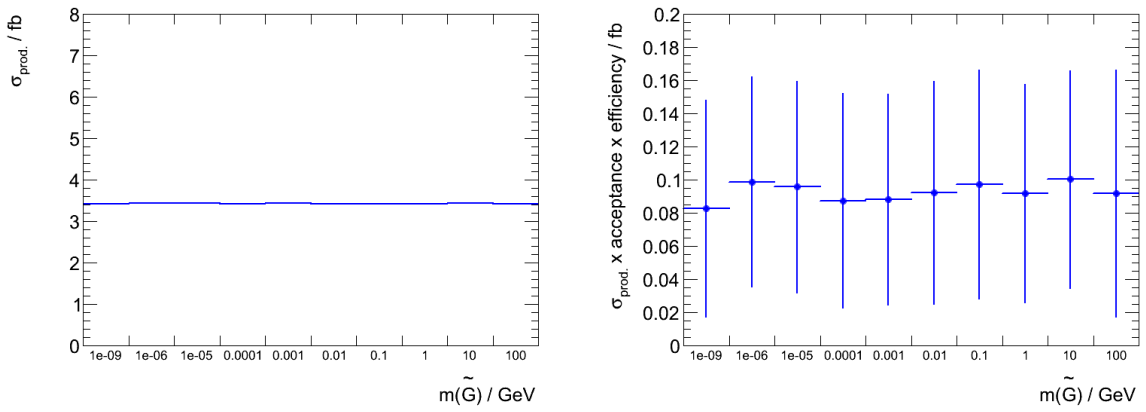

Figure 7.16: $\sigma_{\text{prod.}}$ (left) and $\sigma_{\text{vis.}} = \sigma_{\text{prod.}} \times a \times \epsilon$ (right) under variation of the gravitino mass. A dependence of either variable with respect to variation of the gravitino mass is not visible within the errorbars (if present).

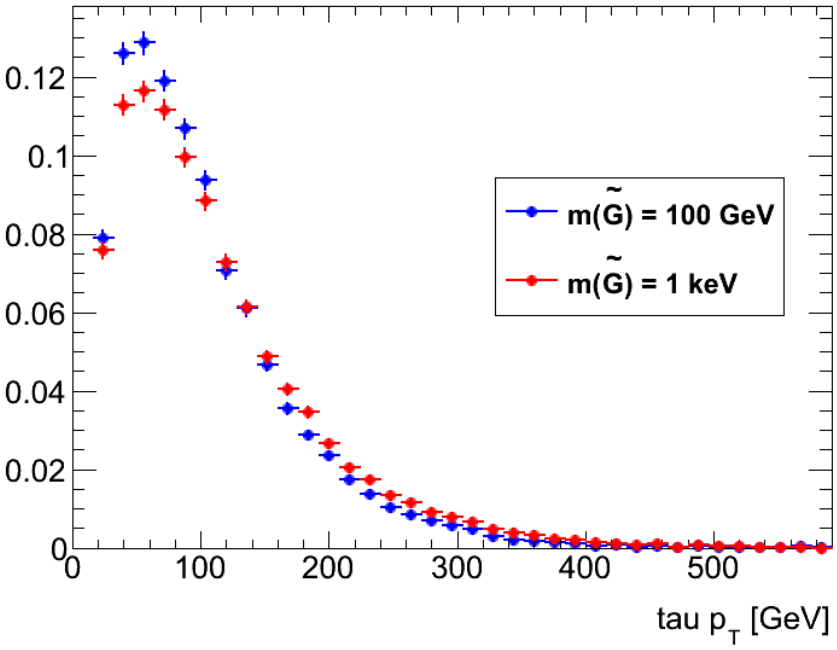

Figure 7.17: Truth level p_{T}^{τ} for different gravitino masses (red: $m\left(\tilde{G}\right) = 1\,\mathrm{keV}$, blue: $m\left(\tilde{G}\right) = 100\,\mathrm{GeV}$). The histograms are normalised. Slightly visible is a trend towards higher values of p_{T}^{τ} for the light gravitino as it is expected.

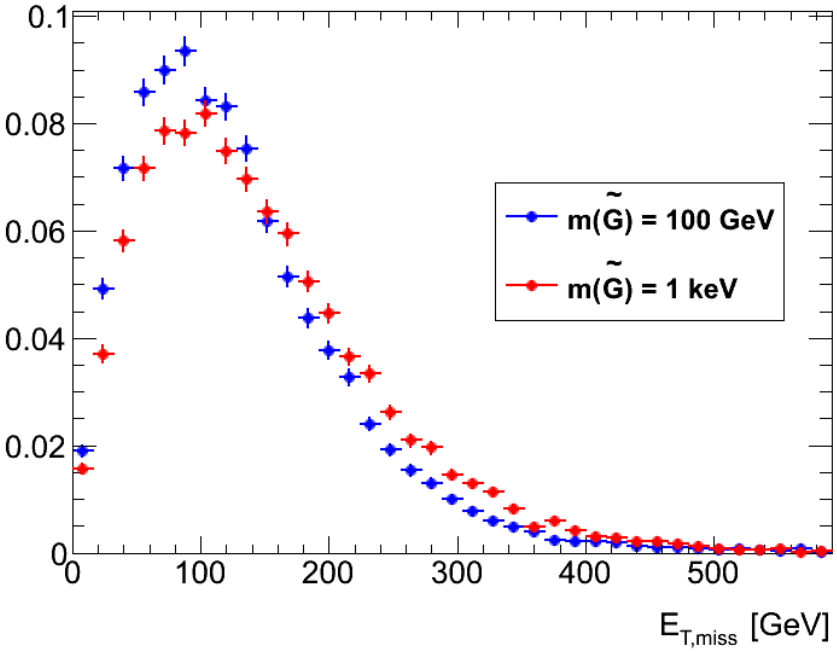

Figure 7.18: Truth level $\not{E}_{\mathrm{T}}$ for different gravitino masses (red: $m\left(\tilde{G}\right) = 1\,\mathrm{keV}$, blue: $m\left(\tilde{G}\right) = 100\,\mathrm{GeV}$). The histograms are normalised. Slightly visible is a trend towards higher values of $\not{E}_{\mathrm{T}}$ for the light gravitino as it is expected.

For every grid point the limit setting procedure is applied calculating a 95% CL exclusion on the number of expected signal events. For sake of diagram readability the grid points with low mass difference between the chargino and the stau are dropped to form an equidistantly spaced grid. Furthermore a so-called model independent (MI) limit on the visible cross section for the full grid is derived. This is achieved by applying the same limit setting procedure on an input that is a dummy grid point with exactly one signal event, no signal systematics but the full background, its systematics and the observed events in data. By providing this input a 95% CL limit on the number of signal events that are in agreement with the given background to sum up to the observed number of events in data is derived. This model independent limit is computed in two ways: one method is the toy MC procedure sampling the test statistic pdf with 1500 toy experiments that is described in section 4.2, the other the asymptotic Asimov procedure (ibid.). Table 7.5 summarises the MI limit results of this analysis and provides the results obtained in [15] as a comparison.

Considering table 7.5 differences between the two methods applied in this analysis and the reference

MI Limit Category	$\langle\epsilon\sigma\rangle^{95}_{\text{obs}}$ [fb]	$S^{95}_{\text{obs.}}$	$S^{95}_{\text{exp.}}$	CL_B	$p(s=0)$
Reference analysis [15]	0.27	5.6	$8.9^{+2.7}_{-3.2}$	0.14	0.42
Asimov asymptotic	0.32	6.7	$8.2^{+3.6}_{-2.4}$	0.28	0.50
MC Toys (1500)	0.45	9.3	$11.4^{+5.0}_{-3.2}$	0.39	0.50

Table 7.5: Left to right: 95% CL upper limits on the visible cross section ($\langle\epsilon\sigma\rangle^{95}_{\text{obs}}$) and on the number of signal events (S^{95}_{obs}). The third column (S^{95}_{exp}) shows the 95% CL upper limit on the number of signal events, given the expected number (and $\pm1\sigma$ excursions on the expectation) of background events. The last two columns indicate the CL_B value, i.e. the confidence level observed for the background-only hypothesis, and the discovery p-value ($p(s=0)$).

analysis are visible. The fact that the toy MC result calculated in this analysis differ from the asymptotic Asimov result is comprehensible: the asymptotic method yields results that are estimates of the limit of sampling the test statistic pdf with infinitely many toy experiments. How good or bad the estimate of the asymptotic Asimov method is, cannot be quantified. Differences with respect to the result in [15] can only be explained by speculation: it is neither known which limit setting procedure (toy MC or asymptotic Asimov) has been applied nor how the systematic uncertainties were assumed to be correlated in [15]. The way the uncertainties are assumed to be correlated within this analysis is not necessarily the same as in [15] since no documentation on this is available.

Starting from the MI limit derived with the asymptotic Asimov method it is possible to calculate 95% CL exclusion limits on both the production cross section and the production cross section times the acceptance for all grid points. Since these quantities are accessible also for theoreticians studying other SUSY models they are of high interest (c. f. section 2.2.2). This is achieved by taking the excluded MI visible cross section $\langle\epsilon\sigma\rangle^{95}_{\text{obs}}$ (which is derived by dividing the excluded number of signal events S^{95}_{obs} by the integrated luminosity of $\mathcal{L} = 20.7\,\text{fb}^{-1}$) and dividing it by the acceptance and efficiency calculated for every grid point or the efficiency only, respectively. Diagrams showing the derived exclusion limits in the $m(\tilde{\chi}^{\pm}_1) - m(\tilde{\tau}^{\pm}_1)$-plane and the corresponding values of excluded $\sigma_{\text{prod.}}$ and $\sigma_{\text{prod.}} \times a$, respectively, are shown in figs. 7.19 and 7.20.

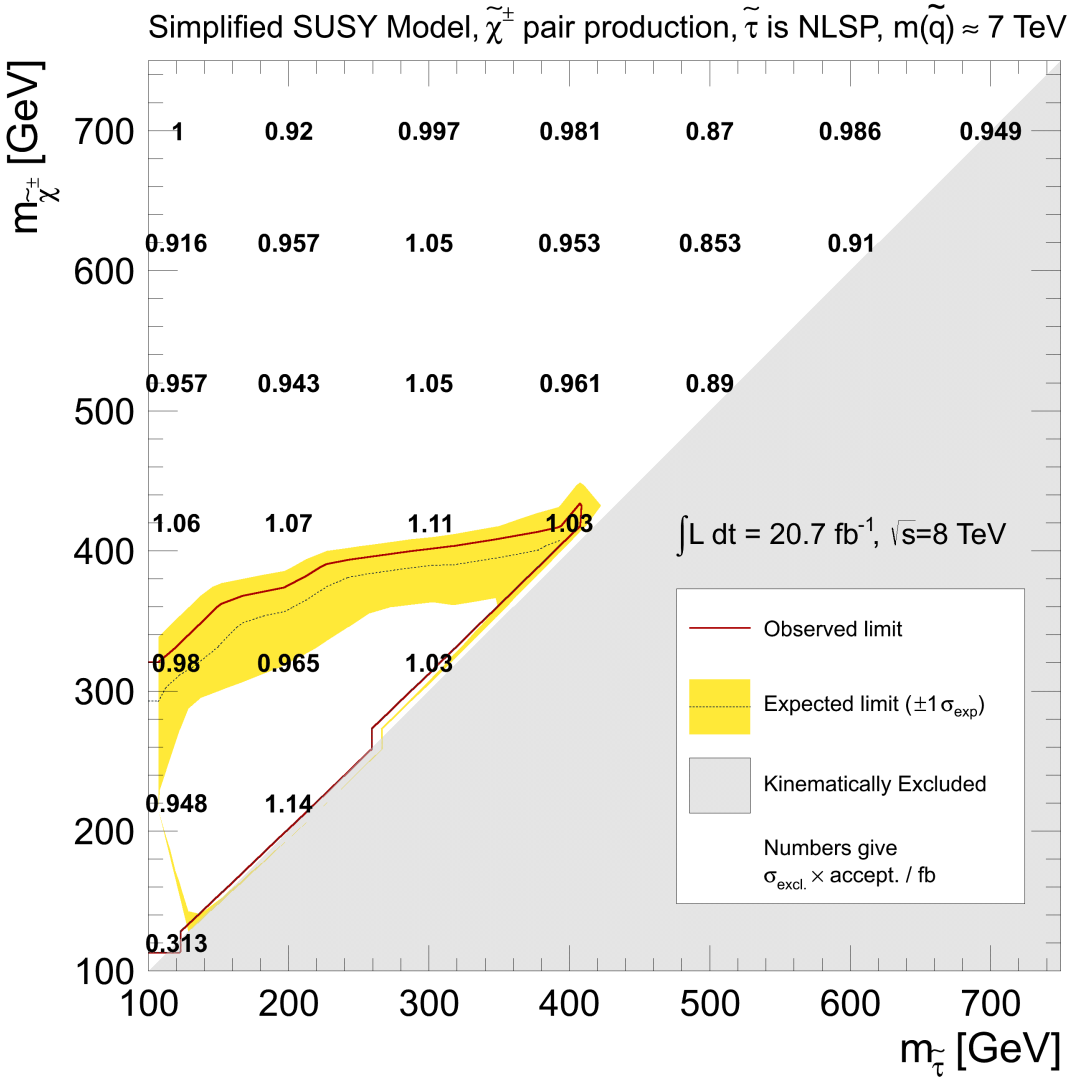

Figure 7.19: Chargino-Stau grid – excl. $\sigma_{\text{prod.}} \times a$. The numbers are derived by dividing the MI limit on $\sigma_{\text{vis.}}$ by the efficiency ϵ for every grid point. The red line illustrates the observed limit as described in section 4.2 but without theoretical uncertainties due to the lack of information on the cross section uncertainties. The grey line illustrates the expected limit as described ibid. with the corresponding 1σ errors in form of an uncertainty band. The grey area is kinematically excluded due to $m\left(\tilde{\chi}_1^{\pm}\right) < m\left(\tilde{\tau}_1^{\pm}\right)$.

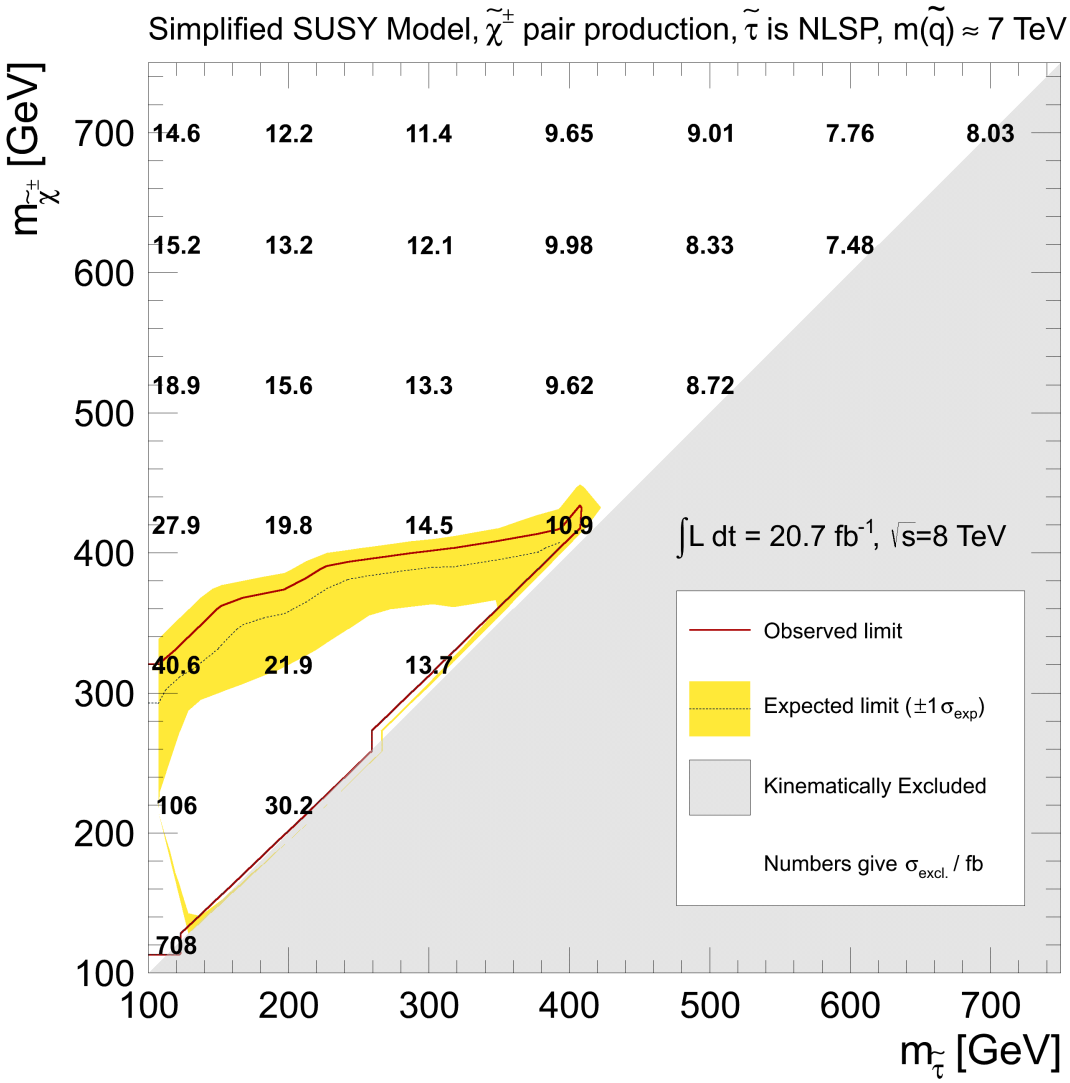

Figure 7.20: Chargino-Stau grid – excl. $\sigma_{\text{prod.}}$. The numbers are derived by dividing the MI limit on $\sigma_{\text{vis.}}$ by the efficiency ϵ and the acceptance a for every grid point. The red line illustrates the observed limit as described in section 4.2 but without theoretical uncertainties due to the lack of information on the cross section uncertainties. The grey line illustrates the expected limit as described ibid. with the corresponding 1σ errors in form of an uncertainty band. The grey area is kinematically excluded due to $m\left(\tilde{\chi}_1^{\pm}\right) < m\left(\tilde{\tau}_1^{\pm}\right)$.

7.4 Summary

The results obtained in the analysis of the full signal grid of this Simplified Model can be further compared to those provided in [15]. Comparing fig. 7.21 to fig. 7.20 or fig. 7.19 displays both similarities and differences: while the reference analysis chose to vary the chargino and the LSP mass, the analysis performed in the framework of this thesis varies the chargino and the stau (NLSP) mass. However, the regions excluded along the $m(\tilde{\chi}_1^{\pm})$-axes are of comparable size and shape. Hence, the conclusion can be drawn, that the study of this Simplified Model has been performed properly and has lead to reasonable results.

A feature that is neglected in [15] is the investigation of possible hidden parameters. It could be shown

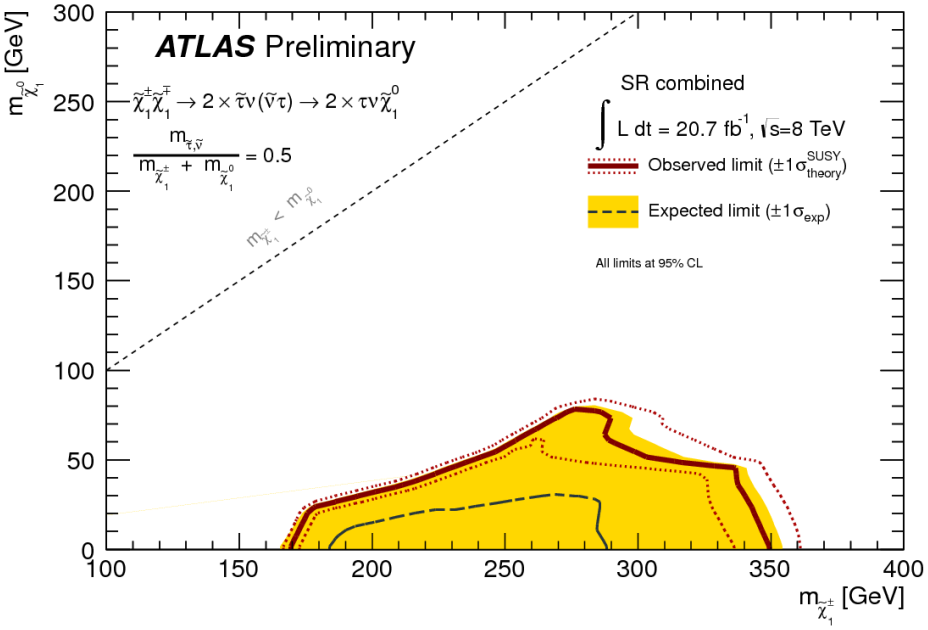

Figure 7.21: Exclusion diagram for the electroweak direct chargino pair production Simplified Model study in the reference analysis [15]. While this analysis chooses to display its results in the $\tilde{\chi}_1^{\pm}$-LSP plane, the analysis performed for this thesis varies the NLSP mass instead of the LSP mass. However, the excluded regions along the $\tilde{\chi}_1^{\pm}$ axes in both analyses are comparable and of similar shape.

that the chargino mixing angle only influences the production characteristics of a Simplified Model and neither an analysis's acceptance nor its efficiency. From an experimentalist's point of view, this variable can remain hidden. However, the observed influence on the production cross section can be of interest for theoreticians re-interpreting this Simplified Model and designing new models of SUSY. Furthermore the influence of the LSP mass has been investigated and proven to be visible. This results has been expected and is supported by the visible dependence of the excluded area in the chargino-LSP plane on the LSP mass in fig. 7.21.

In total the results of this analysis support the results obtained in [15] and are able to answer some of the questions such a Simplified Model raises regarding hidden parameters.

CHAPTER 8

Strong Direct Squark Production

After presenting the results of the pre-studies performed on the auxiliary models, the road towards a strongly produced Simplified Model is paved. The motivation for this model and its design have already been described in section 5.4. This chapter now provides information on the event selection, the considered Standard Model backgrounds and the systematic uncertainties. Furthermore it presents and interprets the obtained results. Similar to the analysis in chapter 7 the event selection strategy of the simplified strong production model is adopted from a similar ATLAS analysis. [14] and [85], respectively, describe the search for Supersymmetry in GMSB and nGM scenarios which share a event topological characteristics with the Simplified Model studies here.
Since the basic analysis procedure is similar to that presented in chapter 7 this chapter is constrained to a brief description of redundant topics emphasising the presentation and interpretation of the obtained results.

8.1 Event Selection

The first section of this chapter describes the event selection applied to the Simplified Model signal samples and the background samples. As usual the goals of the applied criteria are ensuring that only properly reconstructed physics events and objects enter the analysis and to suppress the arising SM background with respect to the SUSY signal of interest. The applied steps of event selection are adopted from [14, 85].

8.1.1 Object Definitions

Similar to section 7.1.1 the definitions of the used baseline objects are provided:
Jets are reconstructed with the anti-k_T algorithm seeded by topological clusters with a distance parameter $\Delta R = 0.4$ and recalibrated using the LC+JES calibration (c. f. section 3.3.1). Baseline jets are required to have $p_T > 20\,\text{GeV}$ and lie within $|\eta| < 2.8$. Jets surviving overlap removal ('signal jets') are further required to fulfil $p_T > 30\,\text{GeV}$ and lie within $|\eta| < 2.0$.
Tau leptons are reconstructed from calorimeter jets with $E_T \geq 10\,\text{GeV}$ as they are described above. Only 1-prong and 3-prong taus with a charge sum equal to +1 or -1 for the latter are considered. The tauID used is the BDT-based ID described in section 3.3.3. Baseline taus are required to fulfil $p_T > 20\,\text{GeV}$ and lie within $|\eta| < 2.5$.
Missing transverse energy is reconstructed as described in 3.3.2 using the specifications given in [85].

The reconstruction of light leptons is not described here since events containing electrons or muons are vetoed. Details on the reconstruction of jets originating from bottom quarks (b-jets) can be found ibid..

8.1.2 Overlap Removal

To ensure that all objects are clearly identified and reconstructed, the procedure of overlap removal is applied in the same way as in the analysis of the Chargino-Stau Simplified Model (c. f. section 7.1.2):

1. Taus overlapping with either an electron or a muon within $\Delta R < 0.2$ are removed.
2. A jet is removed if it overlaps with a tau or an electron within $\Delta R < 0.2$
3. Muons overlapping with jets within $\Delta R < 0.2$ are removed.
4. As a last step electrons or muons overlapping with a jet within $0.2 < \Delta R < 0.4$ are removed for they are assumed to originate from secondary decays within the jet.

8.1.3 Trigger

Before the trigger strategy of this analysis is applied to an event it has to pass the very same 'event cleaning' step as described in section 7.1.3.
The topology of the events of this Simplified Model is characterised by the presence of jets, two tau leptons and missing transverse energy. Hence, triggering on one or more of these objects is a prosperous strategy. For this analysis a combined jet-$\not{E}_{\mathrm{T}}$-trigger is chosen[1]. The selected trigger requires the presence of an online jet of at least 80 GeV in p_{T} and fulfilling the 'very loose' quality criteria along with at least 100 GeV of missing transverse energy.
For this trigger, offline thresholds have to be exceeded in order for the trigger to be in its plateau of response. These offline criteria are the presence of two jets with high transverse momentum of the leading jet ($p_{\mathrm{T}}^{\mathrm{jet}\,1} > 130\,\mathrm{GeV}$, $p_{\mathrm{T}}^{\mathrm{jet}\,2} > 30\,\mathrm{GeV}$) and a higher amount of $\not{E}_{\mathrm{T}}$ ($\not{E}_{\mathrm{T}} > 150\,\mathrm{GeV}$).

8.1.4 Reweighting and Scaling

8.1.5 Signal Region Definition

Before the actual signal region of this analysis is defined, each event is required to contain at least two hadronically reconstructed tau leptons fulfilling the 'medium' quality criterion of the tauID-BDT algorithm (c. f. section 3.3.3). This criterion covers the last unconsidered aspect of the expected characteristic event topology to which the selected trigger is not sensitive: the presence of tau leptons. Furthermore an additional requirement for rejecting QCD background is imposed on each event. Since QCD background mainly contributes with fake taus (c. f. [14, 85]) where the missing energy is wrongly measured this step requires the two leading jets to have a minimal distance from the missing energy vector in ϕ-direction of $|\Delta\phi| > 0.3$. This criterion accounts for the assumption that high-p_{T} jets close to the $\not{E}_{\mathrm{T}}$-vector are mis-measured (c. f. ibid.).
The actual signal region of this analysis is defined by cuts on two kinematic variables – the sum of the transverse mass of the two tau leptons $m_{\mathrm{T}}^{\tau_1} + m_{\mathrm{T}}^{\tau_2}$[2] and the transverse scalar sum H_{T}[3].

[1] ATLAS trigger item EF_j80_a4tchad_xe100_tclcw_veryloose
[2] The transverse mass is described in more detail together with the stransverse mass in section 7.1.6
[3] The transverse scalar sum is the sum over the transverse momenta of the visible objects in an event i. e. here $H_{\mathrm{T}} = \sum_{i=1,2} p_{\mathrm{T}}^{\tau_i} + \sum_{j=1,2} p_{\mathrm{T}}^{\mathrm{jet}_j}$

grid point	$m(\tilde{q}) = 900\,\text{GeV}$ $m\left(\tilde{\chi}_1^{\pm}\right) = 800\,\text{GeV}$ $m(\tilde{\tau}_1) = 700\,\text{GeV}$ $m\left(\tilde{G}\right) = 350\,\text{GeV}$	$m(\tilde{q}) = 1300\,\text{GeV}$ $m\left(\tilde{\chi}_1^{\pm}\right) = 1100\,\text{GeV}$ $m(\tilde{\tau}_1) = 900\,\text{GeV}$ $m\left(\tilde{G}\right) = 450\,\text{GeV}$	$m(\tilde{q}) = 1500\,\text{GeV}$ $m\left(\tilde{\chi}_1^{\pm}\right) = 1100\,\text{GeV}$ $m(\tilde{\tau}_1) = 1100\,\text{GeV}$ $m\left(\tilde{G}\right) = 0\,\text{GeV}$
Cut	# surviving events (scaled)		
No Cut	170.48	8.03	2.1
Channel Definition	3.58	0.50	0.17
$m_{\text{T}}^{\tau_1} + m_{\text{T}}^{\tau_2} > 150\,\text{GeV}$	3.55	0.50	0.17
$H_{\text{T}} > 900\,\text{GeV}$	0.36	0.10	0.11

Table 8.1: For three different points on the strong squark signal grid the number of events after each step of the cut flow is listed. Due to the application of several scaling and reweighting factors (c. f. section 8.1.4) the event numbers are no more of integer type. The selection step 'Channel Definition' covers the application of all selection criteria but the definition of the signal region.

The cut on the transverse mass of the two tau leptons is supposed to suppress background from $Z \to \tau\tau$ events where rather low values of this variable are expected since the missing energy arises only from the tau neutrinos in the tau decays. By choosing a higher cut value additional background from W+jets and top events can be surpressed. The higher cut value is necessary due to the fact that in such events additional missing energy can be present due to additional neutrinos from decays of W bosons. The relevant SUSY signal events are expected to be only weakly suppressed by this selection criterion since they are supposed to contain rather large amounts of missing energy due to neutrinos and LSPs escaping the detector. The effectiveness of requiring $m_{\text{T}}^{\tau_1} + m_{\text{T}}^{\tau_2} > 150\,\text{GeV}$ for different grid points can be extracted from figs. 8.1 to 8.3: most of the $Z \to \tau\tau$ contribution is rejected leaving top, diboson and W+jets as the dominant backgrounds to the signal. Furthermore figs. 8.1 to 8.3 allow for the statement that an even harder cut on $m_{\text{T}}^{\tau_1} + m_{\text{T}}^{\tau_2}$ would be possible. Since the background studies in [14, 85] are performed with the $m_{\text{T}}^{\tau_1} + m_{\text{T}}^{\tau_2} > 150\,\text{GeV}$ selection, this optimised criterion is not applied but a prosperous future selection step.
The cut on $H_{\text{T}} > 900\,\text{GeV}$ is motivated in [14, 85] where a large surpression of the remaining SM backgrounds is achieved by its application. For practical reasons this selection step is adopted. However, a look at figs. 8.4 to 8.6 reveals that this cut is far less useful for this Simplified Model than for the GMSB signal grid of ibid.. Another possible selection criterion which is of practical use since the corresponding background samples are available from ibid., is a less tight cut on H_{T} ($H_{\text{T}} > 600\,\text{GeV}$) in combination with a cut on the jet multiplicity $n_{\text{jet}} > 4$. However, figs. 8.7 to 8.9 show that—as expected due to this model's event topology with only two quarks participating—cutting on the number of jets is only of little effectiveness as well. As a consequence, the GMSB selection with the hard $H_{\text{T}} > 900\,\text{GeV}$ cut is chosen keeping in mind that a harder $m_{\text{T}}^{\tau_1} + m_{\text{T}}^{\tau_2}$ cut would be more appropriate for this simplified model.

For three exemplary signal grid points the results of event selection chain are summarised in table 8.1. Since the events are scaled and reweighted according to 8.1.4 the numbers of events surviving particular selection steps are not necessarily of integer type.

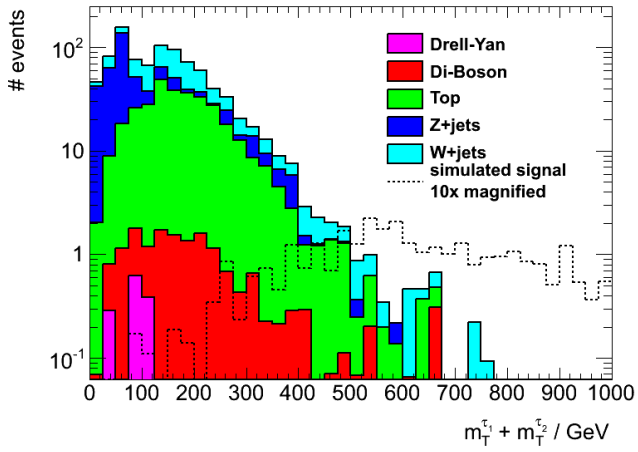

Figure 8.1: $m_T^{\tau_1} + m_T^{\tau_2}$ distribution after the $\Delta\phi(\text{jet}_{1,2}, \not{E}_T)$ cut for the grid point 900/800/700/350.

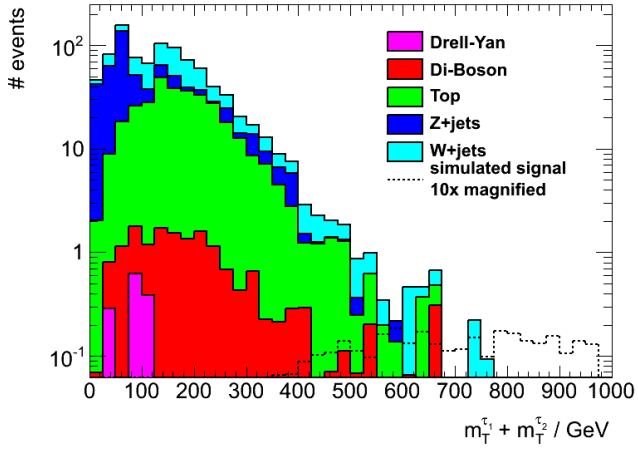

Figure 8.2: $m_T^{\tau_1} + m_T^{\tau_2}$ distribution after the $\Delta\phi(\text{jet}_{1,2}, \not{E}_T)$ cut for the grid point 1300/1100/900/450.

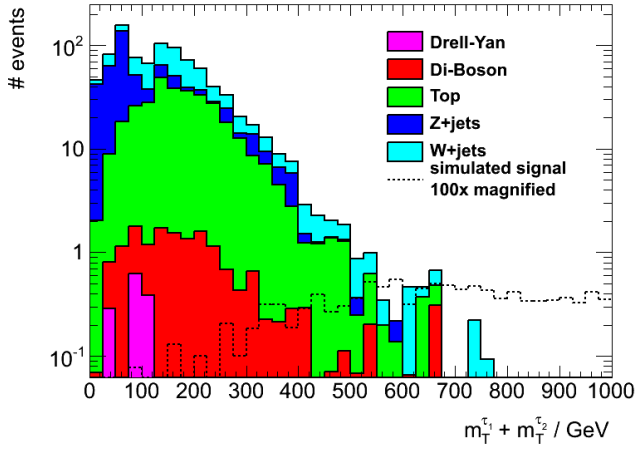

Figure 8.3: $m_T^{\tau_1} + m_T^{\tau_2}$ distribution after the $\Delta\phi(\text{jet}_{1,2}, \not{E}_T)$ cut for the grid point 1500/1100/700/0.

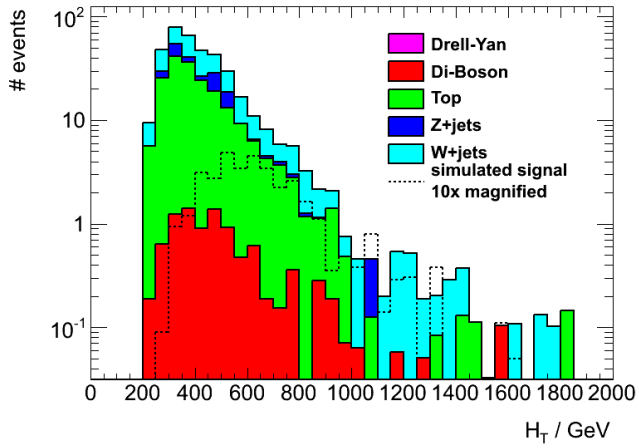

Figure 8.4: H_{T} distribution after the $m_{\mathrm{T}}^{\tau_1} + m_{\mathrm{T}}^{\tau_2}$ cut for the grid point 900/800/700/350.

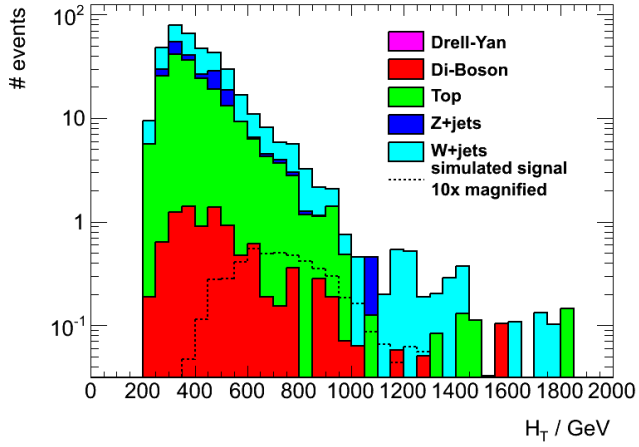

Figure 8.5: H_{T} distribution after the $m_{\mathrm{T}}^{\tau_1} + m_{\mathrm{T}}^{\tau_2}$ cut for the grid point 1300/1100/900/450.

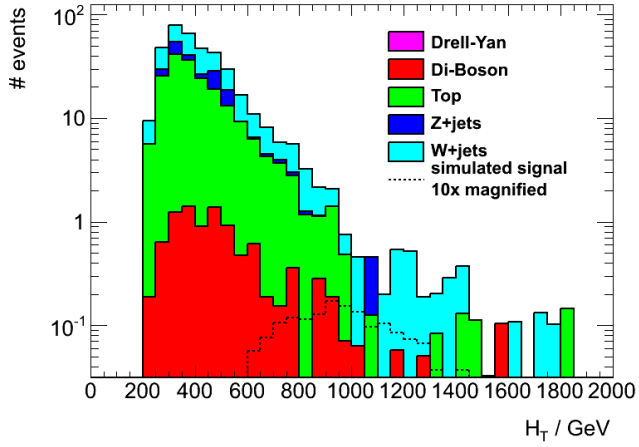

Figure 8.6: H_{T} distribution after the $m_{\mathrm{T}}^{\tau_1} + m_{\mathrm{T}}^{\tau_2}$ cut for the grid point 1500/1100/700/0.

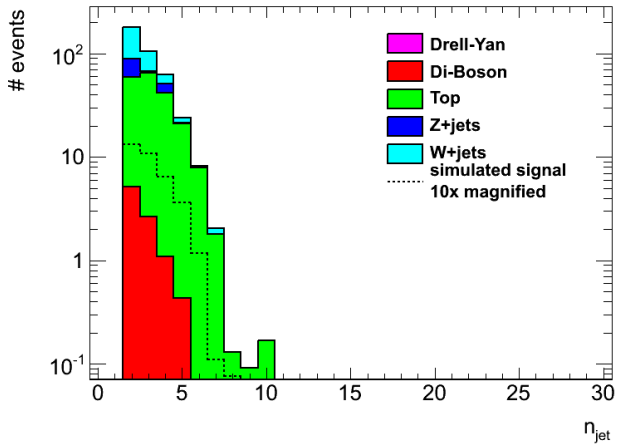

Figure 8.7: n_{jet} distribution after the $m_{\text{T}}^{\tau_1} + m_{\text{T}}^{\tau_2}$ cut for the grid point 900/800/700/350.

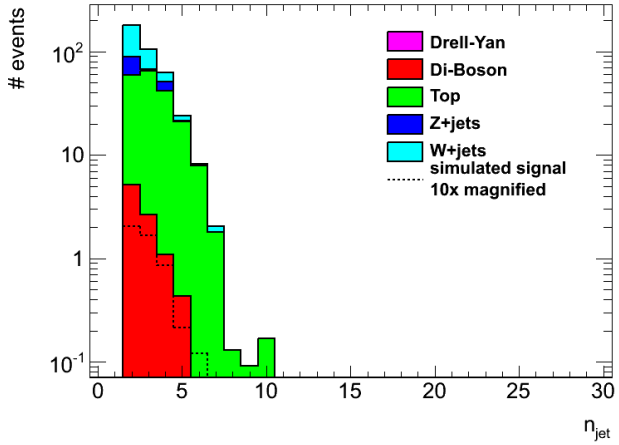

Figure 8.8: n_{jet} distribution after the $m_{\text{T}}^{\tau_1} + m_{\text{T}}^{\tau_2}$ cut for the grid point 1300/1100/900/450.

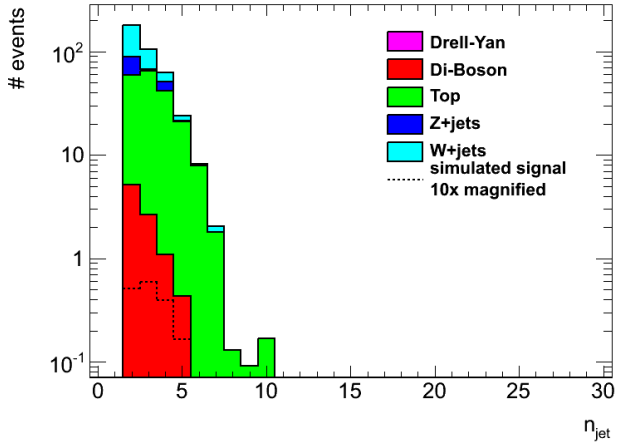

Figure 8.9: n_{jet} distribution after the $m_{\text{T}}^{\tau_1} + m_{\text{T}}^{\tau_2}$ cut for the grid point 1500/1100/700/0.

8.2 Standard Model Backgrounds and Systematic Uncertainties

The SM backgrounds to the analysis of this simplified model are again numerous and similar to the ones already introduced in section 7.2.1. The backgrounds considered here are divided into the following categories:
Di-boson: Similar to ibid., the contribution from WW, ZZ and WZ events is a significant source of background. Such events can produce both real signatures with final state quarks, tau leptons and missing energy and fake signatures where tau leptons are faked by jets and missing energy arises from mismeasurements.
Drell-Yan: This background category covers so-called Drell-Yan processes which are electroweak $q\bar{q}$ annihilation processes occurring via a Z^0 or a γ boson initiated by quarks originating from the colliding hadrons. Drell-Yan processes can mimic basically every event topology that is neutral in terms of its total electric charge (if properly reconstructed) and are hence a source of background to almost every analysis. On the other hand their production cross sections are expected to be rather low since electroweak processes are in general rather suppressed at a proton-proton collider like the LHC.
Top: This category covers both $t\bar{t}$ and single top processes. Due to the large variety of possible decays of the top quark this background can mimic basically any new-physics process with both real and fake signatures. This background contributes the most to the analysis of this Simplified Model (c. f. table 8.2).
W+jets, Z+jets: Similar to the analysis of the electroweak chargino grid, decays of W and Z bosons accompanied by jets make up a source of background contributing with both real and fake signatures (c. f. section 7.2.1).
QCD: QCD multijet events are likely to fake both hadronically decaying tau leptons and missing energy. While strongly collimated jets misidentified as hadronically tau leptons make up the first, mis-measured $\not{E}_{\mathrm{T}}$ due to improper reconstruction of the jets in an event yields the latter effect.
All background contributions are estimated in a semi-data-driven way. By defining so-called control regions (CR)—regions in phase space which are orthogonal to the signal region (SR) determined by inversion of the SR cuts—which are (almost) free of any signal contribution in both data and MC, the contribution of a particular background source is estimated. Comparing MC to data in the CR yields scale factors which match MC to data when being applied to the MC contribution. When assuming no correlation between the signal and the control region, the scale factors can be transferred to the signal region in order to model the corresponding background contribution there.
However, assuming no correlation between signal and control region is too strong of a requirement which is why the influence of contamination of the control regions by signal events and vice versa is accounted for by a systematic uncertainty.
The contribution of QCD and Drell-Yan events to the signal region is so small that is not listed explicitly in table 8.2 which summarises the contributions of all SM backgrounds to the signal region along with their statistical (first uncertainty number) and systematic uncertainties (second uncertainty number).

Detailled information on the calculation and validation of the different background sources to the analysis can be found in [14, 85].

Systematic Uncertainties

The sources of systematic uncertainty considered in the analysis of this simplified model are the same as in the analysis of the electroweak chargino grid: the jet energy scale and resolution, the tau energy scale, the tauID, the scale and resolution of the missing energy, pile-up reweighting, the luminosity and generator and cross section uncertainties. For the same reason as in the analysis of the electroweak chargino grid, no uncertainties on the generator and cross section calculations are considered here.

SM process	# events
di-boson	$0.55 \pm 0.19 \pm 0.19$
top	$2.38 \pm 0.68 \pm 1.43$
W+jets	$0.34 \pm 0.20 \pm 0.41$
Z+jets	$0.33 \pm 0.30 \pm 0.45$
SM total	$3.60 \pm 0.79 \pm 1.57$
data	5

Table 8.2: Summary of the Standard Model background contributions and their statistical and systematic uncertainties. Due to the applied scaling and reweighting factors the given numbers are no more of integer type. Furthermore the number of measured events in data is provided. All numbers are adopted from [14, 85].

Details on how the uncertainties are estimated are provided in [14, 85].

8.3 Results

After introducing the analysis strategy and its resulting event selection steps in section 8.1 and the SM backgrounds of the analysis in section 8.2, this section presents and interprets the results of this analysis. In Addition, the obtained results are briefly compared to those in [14]. However, before results of any kind can be presented, a passage on how to display the four dimensions of the parameter space of this Simplified Model is provided.

8.3.1 The challenge of displaying a four-dimensional parameter space

The Simplified Model grid set up and analysed in this study is embedded into a four-dimensional parameter space which is spanned up by the masses of the four sparticles involved in the model. Since a four-dimensional room is not intuitively accessible and hence not suited for displaying information in it, a way of projecting the four dimensions down to an easily accessible format has to be found. The basic approach performed in this study is to choose the two-dimensional projection which conserves most information on the two dimensions which are not considered and further referred to as 'hidden' dimensions.
In order to estimate the amount of information on a particular variable contained in the two hidden dimensions, the mean and relative standard deviation[4] of that variable averaged over the two hidden dimensions is calculated and displayed for every possible projection.
Since the efficiency of an analysis is the only parameter which is not accessible to theorists (c. f. section 2.2.2) the projection with the least loss of information is chosen to be the one with the least variation in efficiency over the full grid. Figures 8.10 to 8.15 display the means and relative standard deviations of the efficiency for all of the six possible two-dimensional projections of the four-dimensional parameter space averaged over the two hidden dimensions.
In the case that only one grid point is hidden in the two dimensions which are not displayed in a particular projection, the relative standard deviation is not computable since the variance vanishes due to mean and value being the same. For those grid points a blank box is chosen to be displayed instead of the value zero.

[4] the relative standard deviation is the standard deviation normalised to the mean

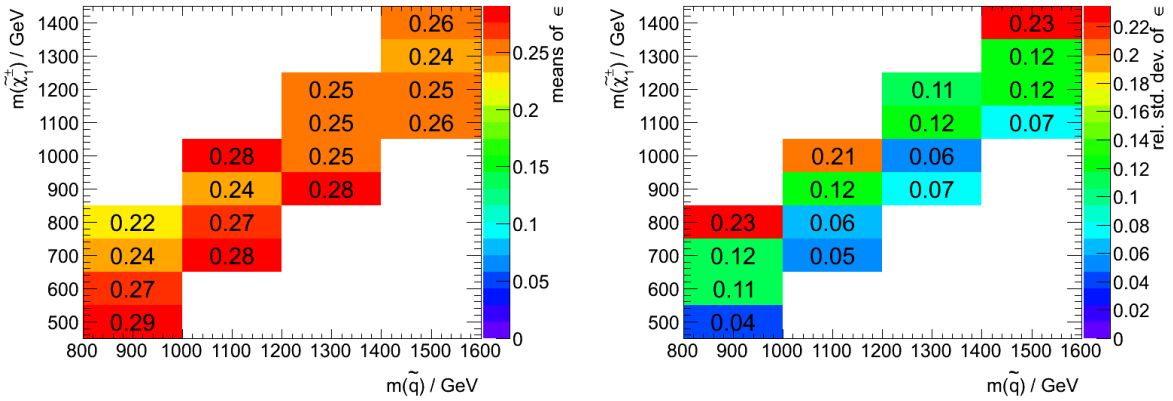

Figure 8.10: The means and relative standard deviations of the analysis's efficiency in the squark-chargino projection averaged over the two hidden dimensions (stau mass and gravitino mass).

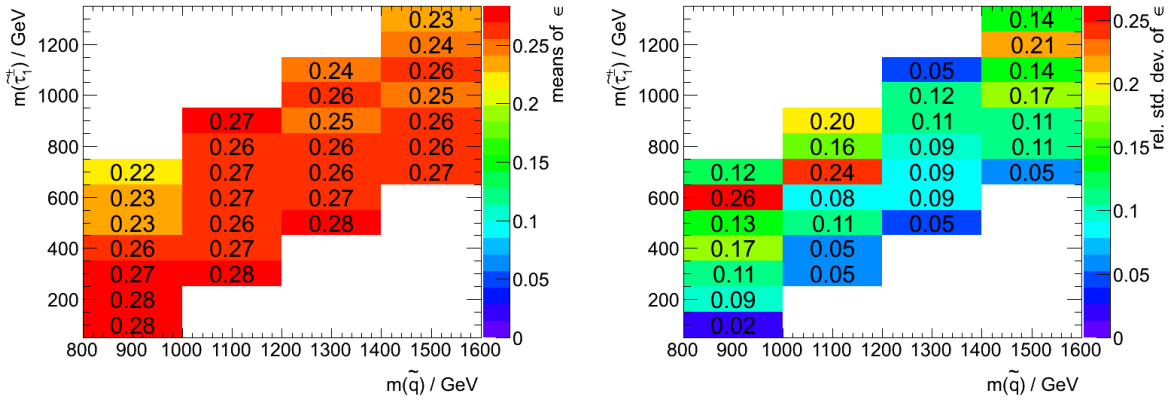

Figure 8.11: The means and relative standard deviations of the analysis's efficiency in the squark-stau projection averaged over the two hidden dimensions (chargino mass and gravitino mass).

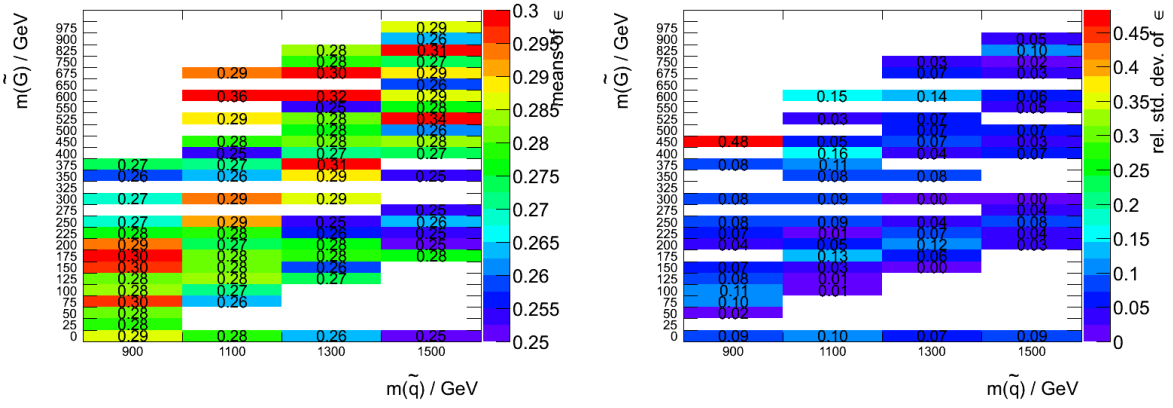

Figure 8.12: The means and relative standard deviations of the analysis's efficiency in the squark-gravitino projection averaged over the two hidden dimensions (chargino mass and stau mass).

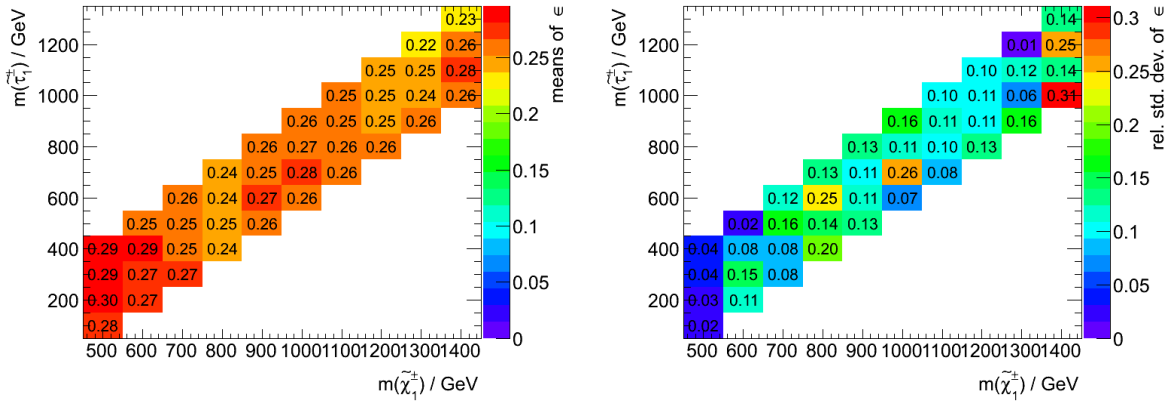

Figure 8.13: The means and relative standard deviations of the analysis's efficiency in the chargino-stau projection averaged over the two hidden dimensions (squark mass and gravitino mass).

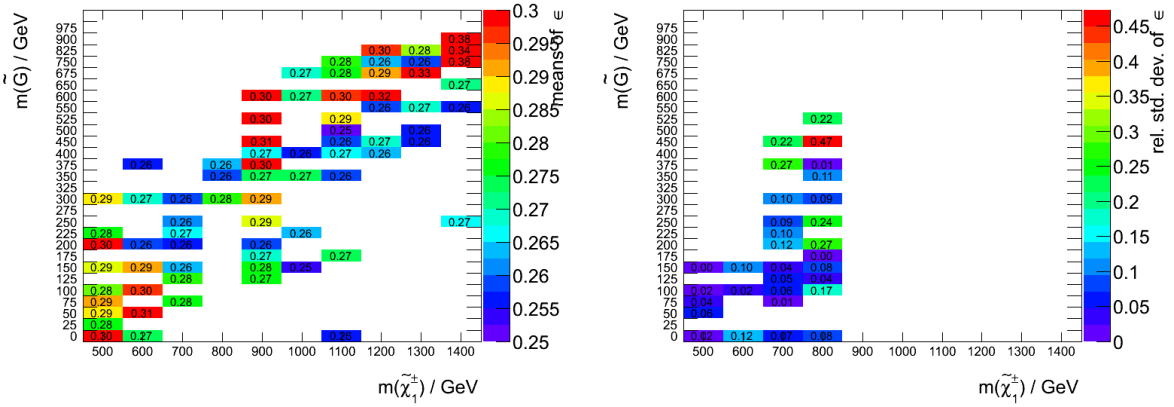

Figure 8.14: The means and relative standard deviations of the analysis's efficiency in the chargino-gravitino projection averaged over the two hidden dimensions (squark mass and stau mass).

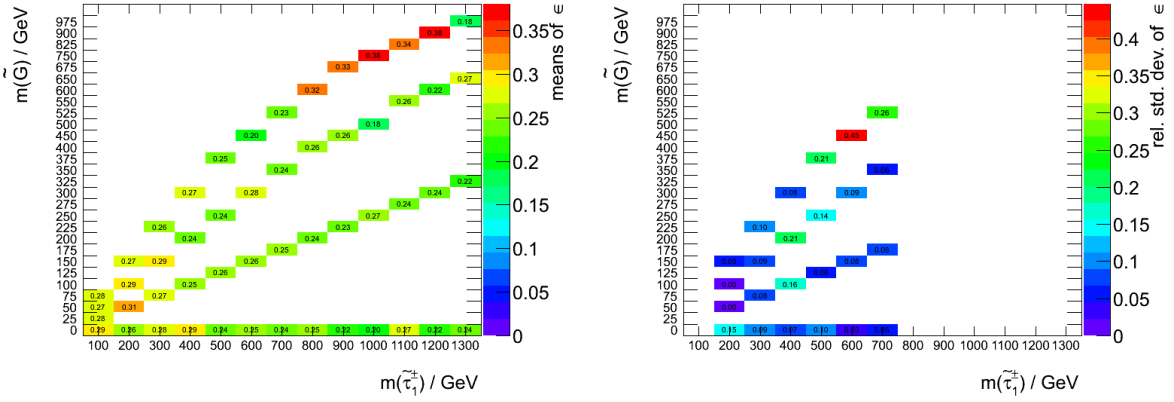

Figure 8.15: The means and relative standard deviations of the analysis's efficiency in the stau-gravitino projection averaged over the two hidden dimensions (squark mass and chargino mass).

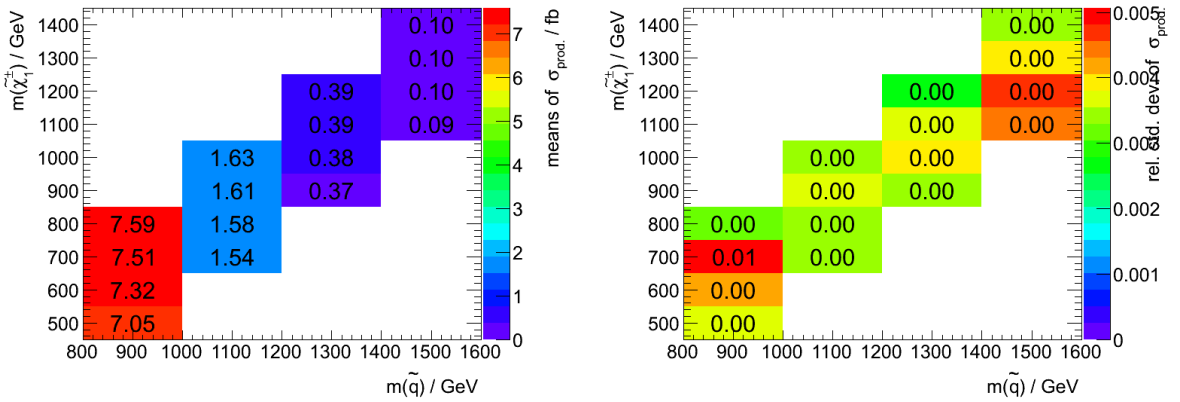

Figure 8.16: The means and relative standard deviations of the grid points' production cross section in the squark-chargino projection averaged over the two hidden dimensions (stau mass and gravitino mass). It is clearly visible that $\sigma_{\text{prod.}}$ only depends on the squark mass.

Looking at figs. 8.10 to 8.15 the projection onto the squark-chargino plane looks most promising in terms of conserving most information on the two hidden dimensions. Hence, this and the corresponding orthogonal projection, i. e. the projection onto the stau-gravitino plane, are chosen for further studies.

8.3.2 Production Cross Section Study

Recalling the studies of the LSP mass variation in section 7.3.2 regarding its influence on the production cross section, a similar cross check can be performed here. Again it is expected that only the initial sparticle mass, i. e. the squark mass, influences the production cross section not the mass of sparticles further down the decay chain. The expectations turns out to be met since fig. 8.16 shows variations only in bins of the squark mass while the relative standard deviations almost vanish.

8.3.3 Limit Setting Results

Now that the best two-dimensional projection of the four-dimensional parameter space and its orthogonal projection are determined, the limit setting procedure as described in section 4.2 can be applied. Since setting limits on averaged means is not providing helpful information, the parameter space has to be separated into slices of interest which contain no more hidden dimensions but are well defined.
While the parametrisation of the slice is fixed to the squark-chargino plane or the stau-gravitino plane, respectively, the question how to chose the values in the two hidden dimensions, arises. The first intuitive approach would be fixing each hidden dimensions to be represented by one value. This approach is impractical for this analysis due to the fact that the parameter grid is chosen such that the ranges of all dimensions but the squark mass depend on each other. As a consequence, it would be impossible to find one value of the stau mass which is present in all points of the squark-chargino plane. However, for the gravitino mass the point of close-to-zero mass would be present for all choices of the other sparticle masses.
Instead of the approach presented above, a different way of selecting values from the two hidden dimensions is chosen. Since for the squark-chargino projection the two hidden dimensions are coupled to the two actual parameters, a dependence of the hidden sector to the visible sector appears to be a viable solution. As a consequence, the mass difference between the chargino and the stau is fixed to be 100 GeV while the gravitino is chosen to be half as heavy as the stau slepton: $m(\tilde{\tau}_1) = m\left(\tilde{\chi}_1^\pm\right) - 100\,\text{GeV}$,

$m\left(\tilde{G}\right) = 1/2 m(\tilde{\tau}_1)$. Hence, the resulting slice through the parameter space is tilted with respect to the stau and gravitino mass axes.
In order to get the same amount of grid points, the slice for the orthogonal projection is chosen in a different way: $m\left(\tilde{\chi}_1^{\pm}\right) = m(\tilde{\tau}_1) + 100\,\text{GeV}$, $m(\tilde{q}) = m\left(\tilde{\chi}_1^{\pm}\right) + 200\,\text{GeV}$. Here the stau and gravitino masses span up the plane while the two hidden dimensions are represented by point-to-point calculated values of the squark and chargino masses.
When applying the limit setting procedure to the parameter slices, point specific limits can be derived. Furthermore, the model independent limits given the observed amount of events in data and the estimated number of background events are derived. Table 8.3 summarises the obtained model indepent 95% CL limits on the visible cross section $\langle\epsilon\sigma\rangle^{95}_{\text{obs}}$, the number of observed events given the estimated background and the observed data $S^{95}_{\text{obs.}}$ and the number of expected events given the estimated background under the background-only hypothesis $S^{95}_{\text{exp.}}$. The numbers are those calculated in the reference analysis [14] which do not change when being recalculated since the background predictions and data observations are equal ibid. and in the analysis performed here.
Based on those model independent results point-specific limits on the production cross section and the

MI Limit Category	$\langle\epsilon\sigma\rangle^{95}_{\text{obs}}$ [fb]	$S^{95}_{\text{obs.}}$	$S^{95}_{\text{exp.}}$	data	total background
Reference analysis [14]	0.42	8.7	$9.6^{+5.2}_{-2.4}$	5	$7.2 \pm 1.3 \pm 1.6$

Table 8.3: Model independent exclusion limits of the strong squark production grid. Left to right: 95% CL upper limits on the visible cross section ($\langle\epsilon\sigma\rangle^{95}_{\text{obs}}$) and on the number of signal events (S^{95}_{obs}). The third column (S^{95}_{exp}) shows the 95% CL upper limit on the number of signal events, given the expected number (and $\pm 1\sigma$ excursions on the expectation) of background events. The last two columns indicate the number of observed events in data and the total amount of estimated background events with its statistical and systematical uncertainties. All numbers are adopted from [14].

product of production cross section and acceptance are calculated and displayed in figs. 8.17 and 8.18 for the squark-chargino projection.
Looking at the point-specific limits in fig. 8.17 and comparing the derived numbers to the production cross sections given in the left diagram of fig. 8.16 and taking into account that the production cross section only depends on the squark mass, it is clearly visible that no point on the signal grid can be excluded with 95% CL. The only available results are the point-specific limits. A possible explanation for the lack of exclusion power of this analysis with respect to [14][5] is due to the gluino mass being extraordinary high (c. f. section 5.4). This step during model development,which is supposed to ensure squark prodcution only, causes the t-channel diagrams in fig. 5.7 in section 5.4 to be strongly suppressed. When less Feynman diagrams contribute to a production process its cross section drops – given that no negative interference of diagrams occurs. Hence, the production cross sections of this simplified model grid are rather low. In addition, the cross section calculation of the used generator only yields leading order results while considering higher order could yield corrections towards higher values.
For the orthogonal projection, i. e. the stau-gravitino plane, the corresponding diagrams are depicted in figs. 8.19 and 8.20.

[5] The nGM analysis in this publication can exclude gluino masses up to 1.14 TeV. Since gluinos and squarks are in a comparable mass range in GMSB (c. f. fig. 2.3 in section 2.2.1), similar squark masses can be excluded which are above the lowest values of this simplified model grid. As a consequence, the exclusion of at least the lowest squark mass points is expected.

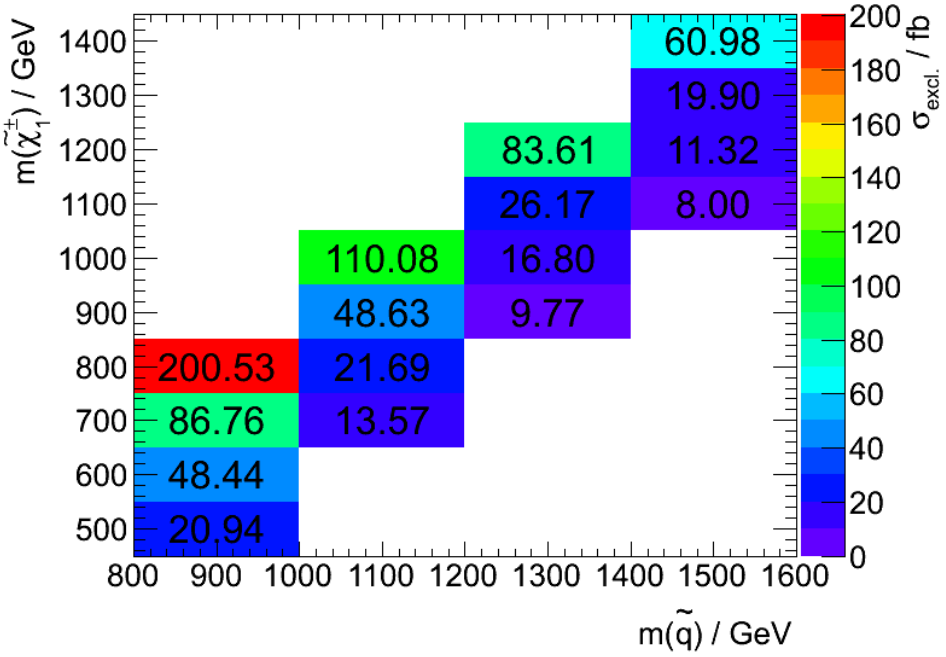

Figure 8.17: Point-specific exclusion limits on the production cross section for a slice through parameter space spanned up by the squark and chargino masses. The hidden dimensions contribute with running values defined via $m(\tilde{\tau}_1) = m\left(\tilde{\chi}_1^{\pm}\right) - 100\,\text{GeV}$, $m\left(\tilde{G}\right) = m(\tilde{\tau}_1)/2$. The excluded cross section is derived by dividing the model independent limit on the visible cross section by the point-specific values of acceptance and efficiency.

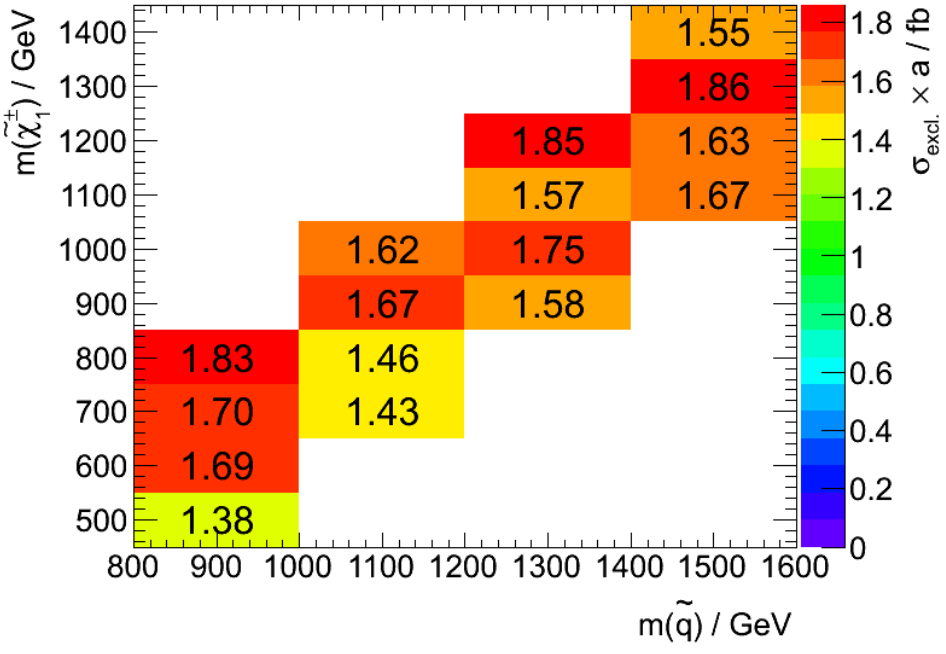

Figure 8.18: Point-specific exclusion limits on the production cross section times the acceptance for a slice through parameter space spanned up by the squark and chargino masses. The hidden dimensions contribute with running values defined via $m(\tilde{\tau}_1) = m\left(\tilde{\chi}_1^{\pm}\right) - 100\,\text{GeV}$, $m\left(\tilde{G}\right) = m(\tilde{\tau}_1)/2$. The excluded values are derived by dividing the model independent limit on the visible cross section by the point-specific values of the efficiency.

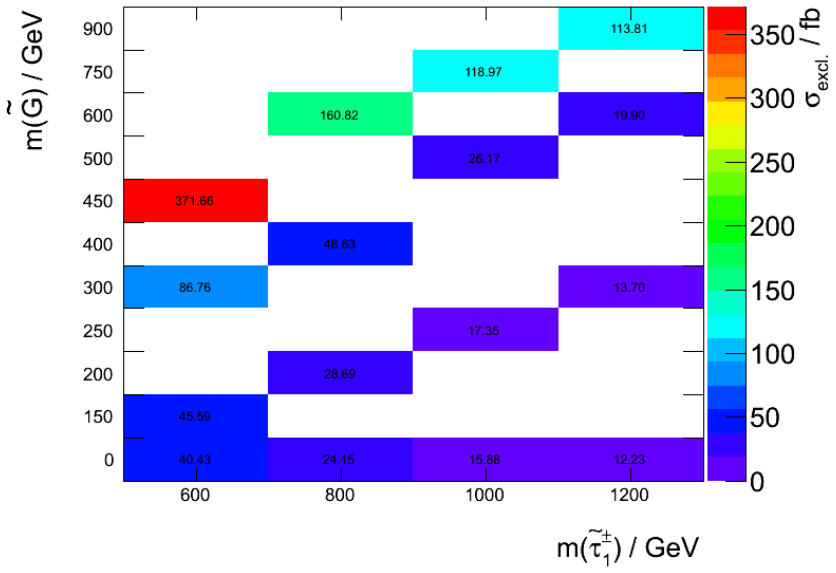

Figure 8.19: Point-specific exclusion limits on the production cross section for a slice through parameter space spanned up by the stau and gravitino masses. The hidden dimensions contribute with running values defined via $m\left(\tilde{\chi}_1^{\pm}\right) = m\left(\tilde{\tau}_1\right) + 100\,\text{GeV}$, $m\left(\tilde{q}\right) = m\left(\tilde{\chi}_1^{\pm}\right) + 200\,\text{GeV}$. The excluded cross section is derived by dividing the model independet limit on the visible cross section by the point-specific values of acceptance and efficiency. For sake of readability, the axes are reduced to the range needed to display all points of the projection.

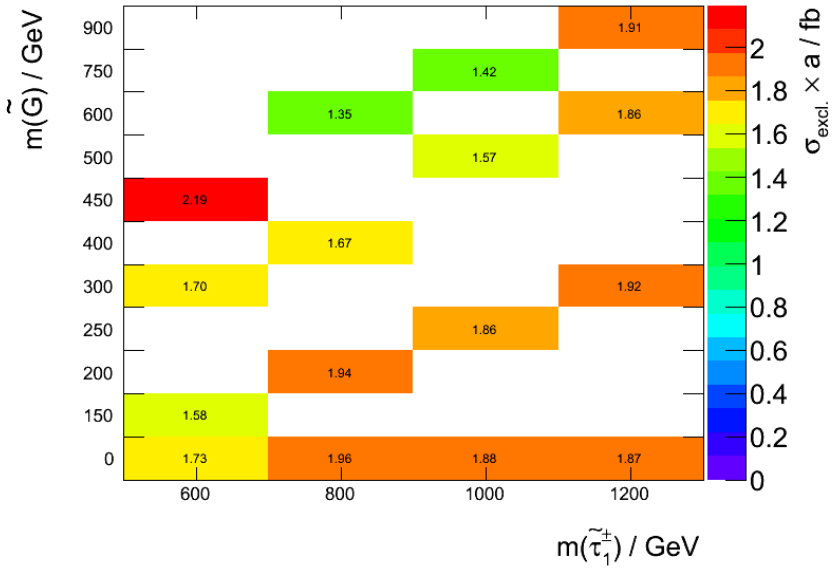

Figure 8.20: Point-specific exclusion limits on the production cross section times the acceptance for a slice through parameter space spanned up by the stau and gravitino masses. The hidden dimensions contribute with running values defined via $m\left(\tilde{\chi}_1^{\pm}\right) = m\left(\tilde{\tau}_1\right) + 100\,\text{GeV}$, $m\left(\tilde{q}\right) = m\left(\tilde{\chi}_1^{\pm}\right) + 200\,\text{GeV}$. The excluded values are derived by dividing the model independent limit on the visible cross section by the point-specific values of the efficiency. For sake of readability, the axes are reduced to the range needed to display all points of the projection.

8.3.4 Closure Test – How hidden are the 'hidden' dimensions?

The goal of developing und studying Simplified Models is to provide model-independent exclusion limits on observables which are of interest to theorists who develop new SUSY scenarios (c. f. section 2.2.2). By setting limits on e. g. sparticle masses in a particular SUSY decay chain independent of any SUSY model a quick and easy access to test a new SUSY scenario is supposed to be provided. Since theorists can only predict truth-level observables like production cross sections or the acceptance of an analysis—given that the event selection is known to them—the efficiency is the crucial experimental observable of interest for them. As already mentioned in section 8.3.1, the change in efficiency also estimates the amount of lost information stored in the hidden dimensions of the simplified model. In order to test how closed this simplified model is a so-called 'closure test' is performed in this section. Within this test it is evaluated how good or bad an extrapolation from one slice through parameter space (for a chosen projection plane) to another can be performed. In detail, it is tried to transfer the efficiency and the efficiency times the acceptance of one slice to another for a given parameter plane spanning up the two dimensional space. If both distributions (ϵ and $a \times \epsilon$) are flatly enough distributed in the hidden dimensions, deviations from the extrapolated visible cross section to the true value—which is the model independent limit derived for this analysis—should be small.
To quantify the results of this test the deviation of the extrapolated visible cross section normalised to the true value is derived. The reference slice from which $a \times \epsilon$ and ϵ are taken is the slice studied in sections 8.3.2 and 8.3.3 while the test slice is characterised by $m(\tilde{\tau}_1) = m\left(\tilde{\chi}_1^{\pm}\right) - 200\,\text{GeV}$ and $m\left(\tilde{G}\right) = 1/2 m(\tilde{\tau}_1)$. Taking the $\sigma_{\text{prod.}}$ from the test slice and multiplying it with $(a \times \epsilon)_{\text{ref.}}$ from the reference slice (or taking $\sigma_{\text{prod.}} \times a$ and multiplying it with $\epsilon_{\text{ref.}}$), subtracting $\sigma_{\text{excl. vis.}} \equiv \langle \epsilon\sigma \rangle_{\text{obs}}^{95}$ and normalising to $\langle \epsilon\sigma \rangle_{\text{obs}}^{95}$, yields figs. 8.21 and 8.22.
By looking at these distributions it becomes obvious that transferring the product $a \times \epsilon$ does not yield results which reproduce the true value – all relative differences are close to 1 and thus maximal. This observation becomes clear when looking at the means and relative standard deviations of the acceptance averaged over the hidden dimensions in the squark-chargino plane depicted in fig. A.4 in appendix A: the acceptance varies much more over the displayed plane than the efficiency. Hence, transferring both acceptance and efficiency is not sufficient for drawing conclusions on other slices through the parameter space than a particular reference slice.
Things look different when only transferring the efficiency which was more flatly distributed in the squark-chargino plane. Figure 8.22 shows much lower deviations from the true value than fig. 8.21. As a consequence, one can conclude that calculating the production cross section and acceptance for a full grid of signal points is enough to draw reasonable conclusions when extrapolating the efficiency from a given reference slice through parameter space in the same projection. The closure test thus is successful and yields the expected results: the acceptance cannot be transferred from one grid slice to another because it changes too much from point to point while the efficiency is well transferable.

8.4 Summary

For the analysis of a Simplified Model of strong direct squark production the best two-dimensional projection of the four-dimensional parameter space has been found. This has been achieved by quantifying the loss of information contained in dimensions not considered in such a projection. For the projection decided on, the projection onto the squark-chargino plane, the limit setting procedure described in section 4.2 has been applied yielding point-specific exclusion limits on $\sigma_{\text{prod.}}$ and $\sigma_{\text{prod.}} \times a$ as well as a model-independent limit on the visible cross section. Induced by the high gluino mass in this Sim-

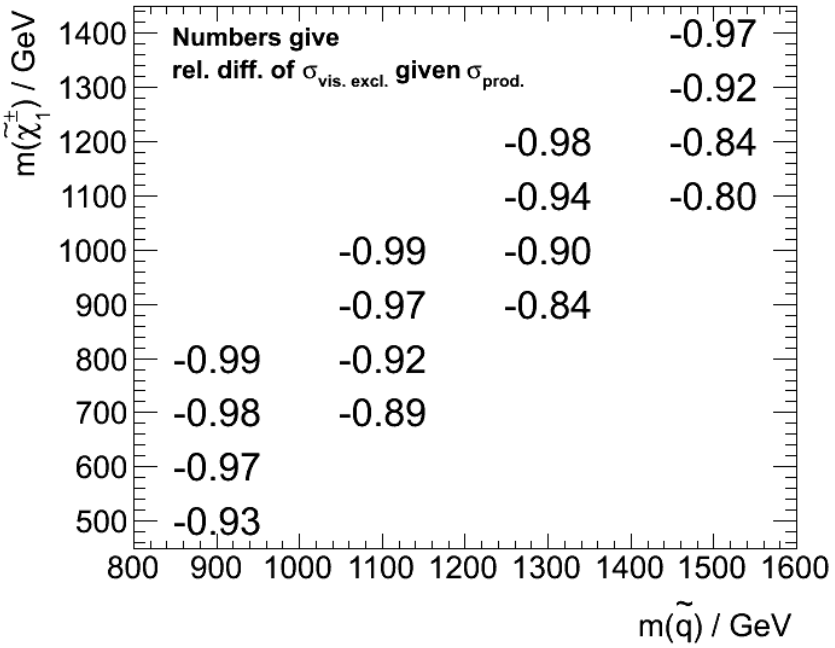

Figure 8.21: Closure test result in the squark-chargino plane transferring $a \times \epsilon$ from the reference slice to the test slice. The numbers give the difference of the extrapolated limit on the visible cross section to the true value normalised to the true value. The true value is the model indepent limit $\langle \epsilon\sigma \rangle^{95}_{\text{obs}}$.

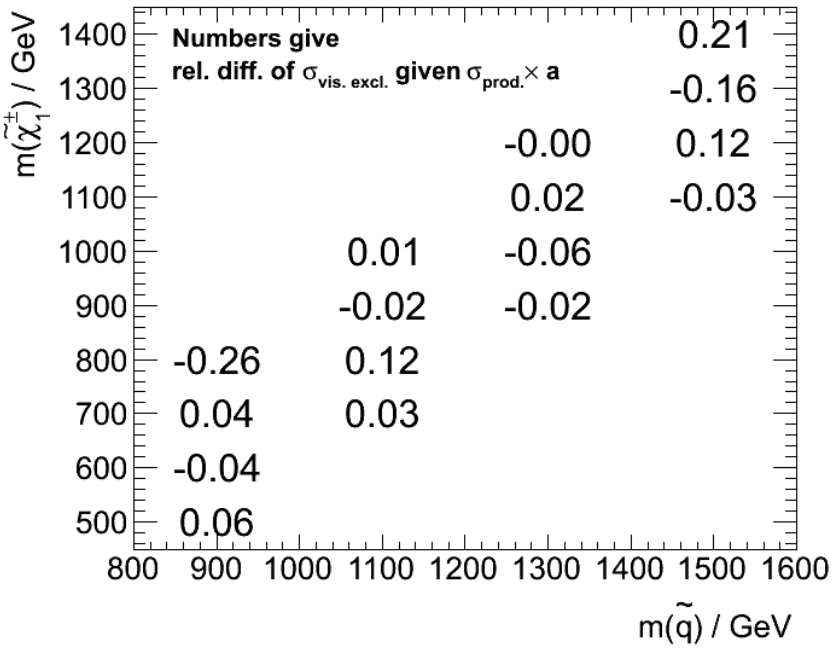

Figure 8.22: Closure test result in the squark-chargino plane transferring ϵ from the reference slice to the test slice. The numbers give the difference of the extrapolated limit on the visible cross section to the true value normalised to the true value. The true value is the model indepent limit $\langle \epsilon\sigma \rangle^{95}_{\text{obs}}$.

plified Model the production cross sections of the signal grid points are very low. This has prevented the analysis of this Simplified Model from excluding parts of the parameter space of SUSY. However, a closure-test has shown that extrapolations from one grid slice to another are well possible as long as only the analysis's efficiency is transferred while the production cross section and analysis's acceptance have to be calculated point-by-point. This result is of interest for theoreticians who want to design new models of SUSY that contain the topology studies here. They can then use the results obtained from this analysis to infer exclusion limits on their models by mapping this analysis's efficiency onto their grid of excluded $\sigma_{\text{prod.}} \times a$.
Considering the event selection criteria which have been adopted from [14] an optimisation is expected to yield results of more exclusion power. In addition to this, the inclusion of the gluino and its mass as an additional parameter are an interesting prospect for future developments regarding strongly produced Simplified Models of this kind.

CHAPTER 9

Conclusions

Studies on Simplified Models of strong production involving final state leptons and the investigation of a sector of hidden model parameters have been successfully performed. An overview of the electroweak Simplified Model studies of the ATLAS collaboration is given in fig. 9.1[1]. Along with [15] this thesis presents the first results of Simplified Model searches with tau leptons in the final state.

In the framework of this thesis three different Simplified Models have been developed and studied. The main goal—the design and analysis of a strongly produced Simplified Model of SUSY with final state tau leptons—has been motivated by the favoured production processes at a proton-proton collider like the LHC and the abundances of different SUSY processes in a tau-rich model like GMSB. The model decided on is a model of direct strong squark production: $\tilde{q} \rightarrow \tilde{\chi}_1^{\pm} \rightarrow \tilde{\tau}_1 \rightarrow \tilde{G}$. The design of this model has lead to a four-dimensional space in which the model has been parametrised by the masses of the four sparticles participating. The challenge of displaying such a complex space has been accomplished by choosing the best—i. e. most information-conserving—two-dimensional projection of the four-dimensional parameter space. The loss of information has been quantified by the mean and relative standard deviation of the analysis efficiency for each point in each two-dimensional projection averaged over the two hidden dimension. The best projection has been decided on by choosing the one with the flattest distribution of efficiency and the smallest relative standard deviations – the squark-chargino projection. For designated slices through the parameter space in this projection and its orthogonal counter part, the stau-gravitino projection, 95% CL limits on the production cross section $\sigma_{\text{prod.}}$ and $\sigma_{\text{prod.}} \times a$ have been calculated. Furthermore a closure test has shown that the transfer of results obtained for one slice to another within the same projection is possible as long only the analysis's efficiency is transferred and not its acceptance as well. In order to re-use the model-independent results obtained in this way both the production cross section and acceptance of a new model have to be provided while the efficiency can be transferred from the studies performed here.

In addition to the analysis of a Simplified Model of strongly produced SUSY events, Simplified Models of the two sub-decay chains of the primary model haven been designed and investigated.

For a model of direct electroweak pair production of charginos parametrised in the masses of the $\tilde{\chi}_1^{\pm}$ and the $\tilde{\tau}_1$ 95% CL exclusion limits on $\sigma_{\text{prod.}}$ and $\sigma_{\text{prod.}} \times a$ have been calculated and compared to the reference analysis [15]. In addition to the studies already performed ibid., the influence of two hidden parameters of this model has been studied. It has been shown that the chargino mixing angle only in-

[1] The number of strong production Simplified Models is much higher and not summarised in one diagram. However, the results are accessible via https://twiki.cern.ch/twiki/bin/view/AtlasPublic/SupersymmetryPublicResults

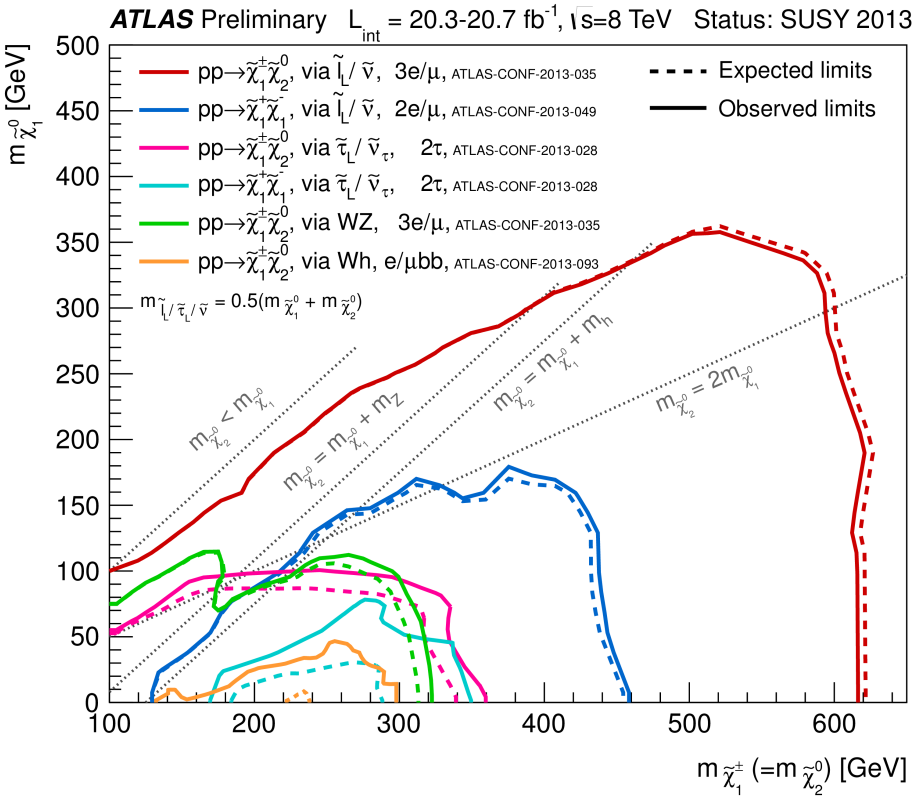

Figure 9.1: Overview of the electroweak Simplified Model studies that have been published by the ATLAS collaboration for SUSY2013. The results of ATLAS-CONF-2013-028 are the the ones obtained from the reference analysis of the electroweak direct chargino pair production Simplified Model. Image taken from https://twiki.cern.ch/twiki/pub/AtlasPublic/CombinedSummaryPlots/ATLAS_SUSY_EW_SUSY2013.pdf, ATLAS Experiment ©2013 CERN

fluences the production cross section once the branching fractions have been fixed and hence can still be considered hidden. The mass of the LSP has proven to be of non-negligible influence. It affects both the final state tau momentum and missing energy distributions which are of huge importance to many analyses and themselves affect an analysis's efficiency. For those reasons the LSP mass is a parameter which has to be considered when designing future models.
The second sub-model studied within the framework of this thesis is a model of electroweak direct stau pair production. This model has served the purpose of investigating the stau mixing angle as a hidden parameter. This observable has proven to be of interest once an analysis is sensitive to the electric charge of the final state tau leptons since the stau mixing angle influences the tau kinematics—e. g. the tau transverse momentum—in a charge-dependent way.
Besides these numerous results this thesis has developed several ideas for future studies of Simplified Models in the search for SUSY. First of all the model of strong production could be expanded by a fifth parameter, the gluino mass, to also describe the superpartner of the gluon which is yet excluded from the model. This step is of particular interest since the production of gluinos makes up a significant contribution to the spectrum of possible primary sparticles produced at the LHC. Furthermore the study of the hidden sector of neutralino physics is expected to yield interesting results since it is more complex than the sector of charginos. Finally a detailed study of the tau polarisation and related effects is expected to yield results of interest. This proposal is motivated by the fact that knowledge of the tau decay products is expected to yield deeper understanding of the observed charge-dependent effects. However, for such an analysis a dedicated tau substructure reconstruction tool is needed which is yet to be tested.
As a final conclusion the results of this thesis can be interpreted as a next step on a new path towards discovering (or excluding) SUSY at the TeV scale. It could be shown that Simplified Models are a prosperous approach in the search for Supersymmetry when they are studied in more detail than they haven treated up to now. It is necessary to put effort into the analysis of hidden parameters. Performing analyses on grids parametrised by sparticle masses and not taking possible hidden parameters into account is not sufficient.

APPENDIX A

Additional Information

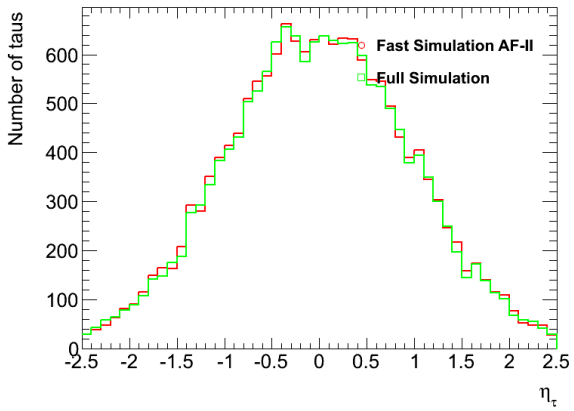

Figure A.1: η_τ distributions for the grid point $m(\tilde{chi}_1^\pm) = 520\,\text{GeV}$, $m(\tilde{tau}_1) = 510\,\text{GeV}$ for comparison of AFII Fast Simulation and the ATLAS Full Simulation. Qualitatively, the agreement between both distributions is good.

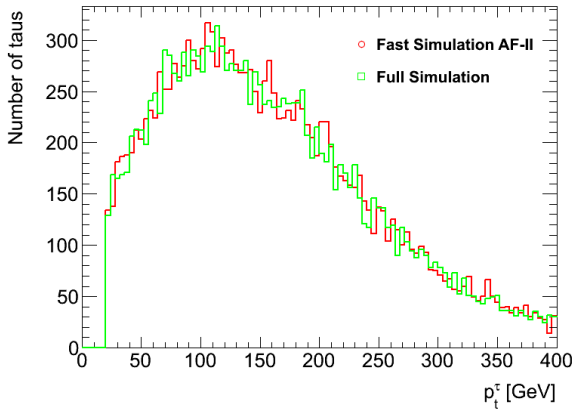

Figure A.2: p_T^τ distributions for the grid point $m(\tilde{chi}_1^\pm) = 520\,\text{GeV}$, $m(\tilde{tau}_1) = 510\,\text{GeV}$ for comparison of AFII Fast Simulation and the ATLAS Full Simulation. Qualitatively, the agreement between both distributions is good.

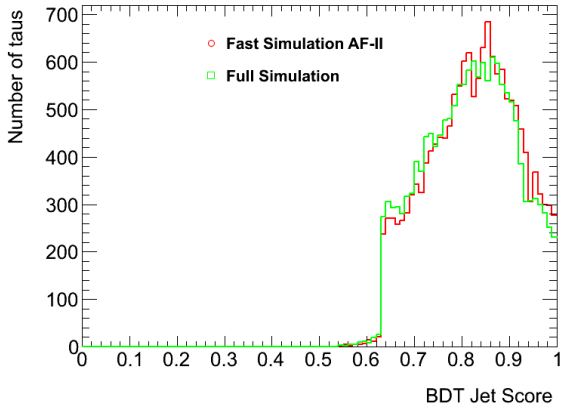

Figure A.3: TauBDTJetScore distributions for the grid point $m(\tilde{chi}_1^\pm) = 520\,\text{GeV}$, $m(\tilde{tau}_1) = 510\,\text{GeV}$ for comparison of AFII Fast Simulation and the ATLAS Full Simulation. Qualitatively, the agreement between both distributions is good.

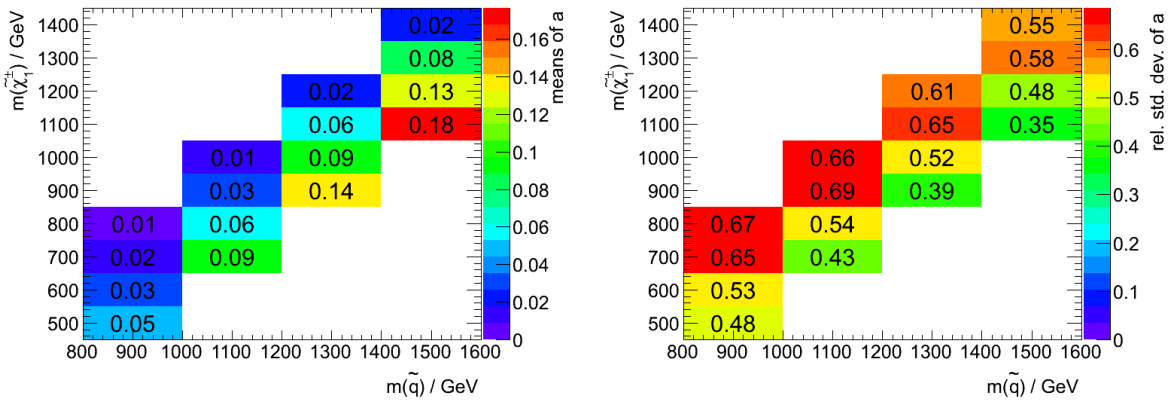

Figure A.4: The means and relative standard deviations of the analysis' acceptance in the squark-chargino projection averaged over the two hidden dimensions (stau mass and gravitino mass).

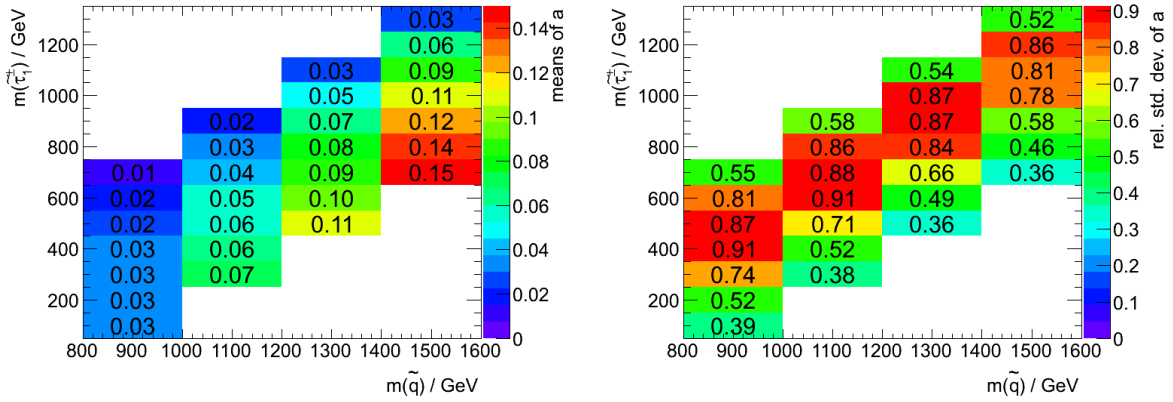

Figure A.5: The means and relative standard deviations of the analysis's acceptance in the squark-stau projection averaged over the two hidden dimensions (chargino mass and gravitino mass).

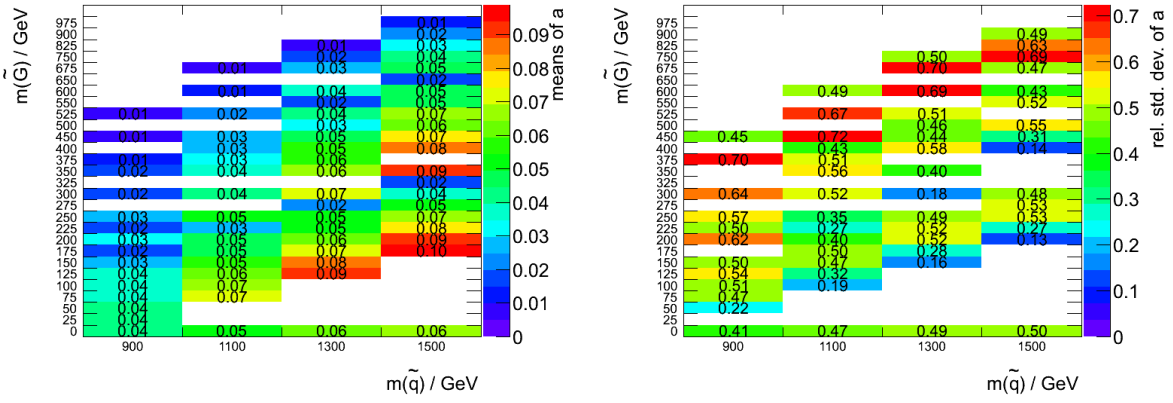

Figure A.6: The means and relative standard deviations of the analysis's acceptance in the squark-gravitino projection averaged over the two hidden dimensions (chargino mass and stau mass).

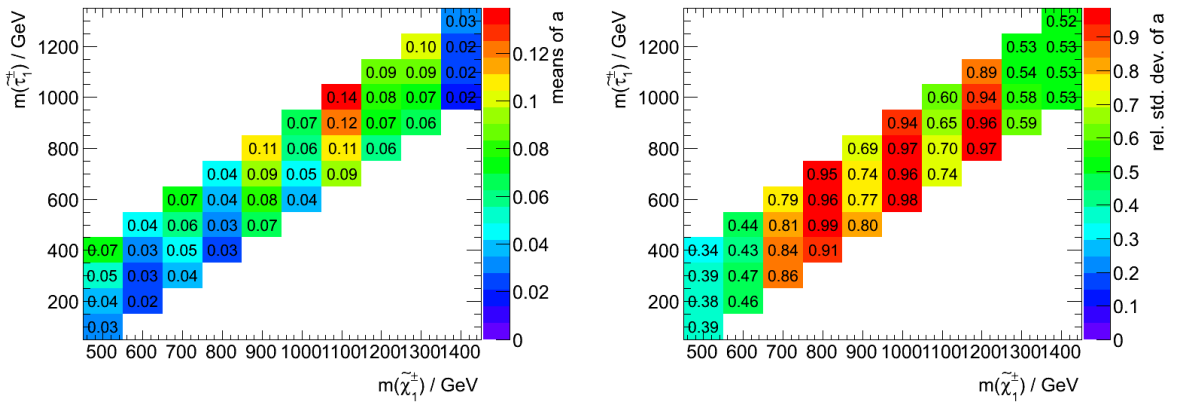

Figure A.7: The means and relative standard deviations of the analysis's acceptance in the chargino-stau projection averaged over the two hidden dimensions (squark mass and gravitino mass).

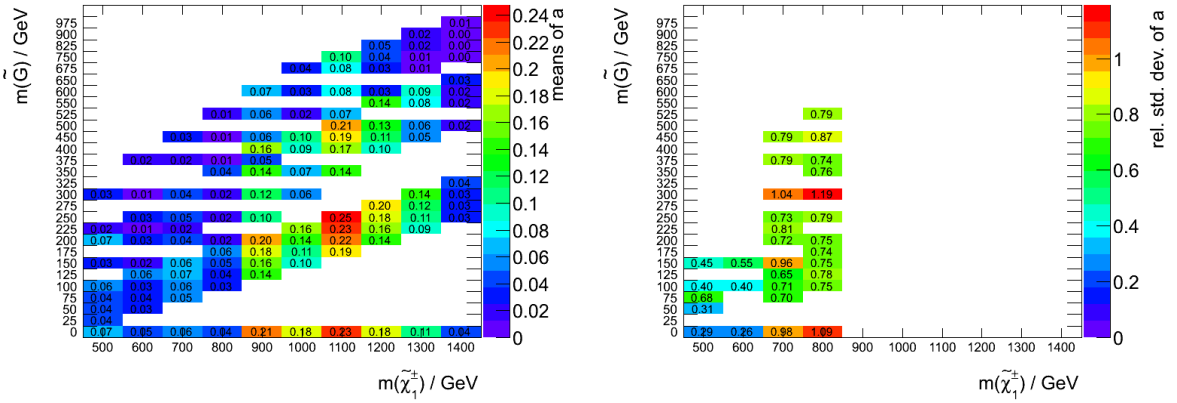

Figure A.8: The means and relative standard deviations of the analysis's acceptance in the chargino-gravitino projection averaged over the two hidden dimensions (squark mass and stau mass).

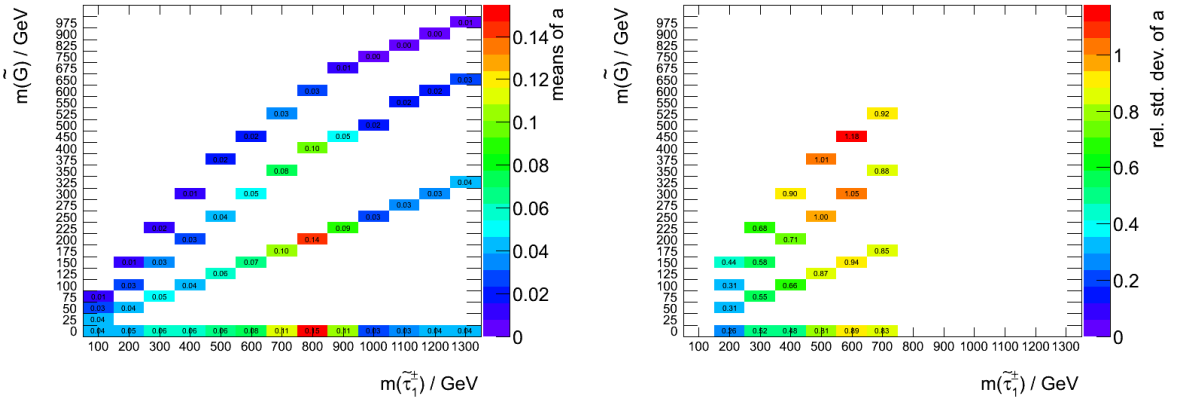

Figure A.9: The means and relative standard deviations of the analysis's acceptance in the stau-gravitino projection averaged over the two hidden dimensions (squark mass and chargino mass).

Bibliography

[1] E. W. Kolb and M. S. Turner, "The Early Universe", *Front.Phys.* 69 (1990) 1–547.

[2] D. Spergel et al., "First year Wilkinson Microwave Anisotropy Probe (WMAP) observations: Determination of cosmological parameters", *Astrophys.J.Suppl.* 148 (2003) 175–194, DOI: 10.1086/377226, arXiv: astro-ph/0302209 [astro-ph].

[3] C. Bambi and A. Dolgov, "Antimatter in the Milky Way", *Nucl.Phys.* B784 (2007) 132–150, DOI: 10.1016/j.nuclphysb.2007.06.010, arXiv: astro-ph/0702350 [astro-ph].

[4] F. Zwicky, "Die Rotverschiebung von extragalaktischen Nebeln", *Helv.Phys.Acta* 6 (1933) 110–127.

[5] H. Miyazawa, "Baryon Number Changing Currents", *Prog. Theor. Phys.* 36 (6) (1966) 1266–1276, DOI: 10.1143/PTP.36.1266.

[6] P. Ramond, "Dual Theory for Free Fermions", *Phys. Rev.* D3 (1971) 2415–2418, DOI: 10.1103/PhysRevD.3.2415.

[7] Y. A. Gol'fand and E. P. Likhtman, "Extension of the Algebra of Poincare Group Generators and Violation of p Invariance", *JETP Lett.* 13 (1971), [Pisma Zh.Eksp.Teor.Fiz.13:452-455,1971] 323–326.

[8] A. Neveu and J. H. Schwarz, "Factorizable dual model of pions", *Nucl. Phys.* B31 (1971) 86–112, DOI: 10.1016/0550-3213(71)90448-2.

[9] A. Neveu and J. H. Schwarz, "Quark Model of Dual Pions", *Phys. Rev.* D4 (1971) 1109–1111, DOI: 10.1103/PhysRevD.4.1109.

[10] J. Gervais and B. Sakita, "Field theory interpretation of supergauges in dual models", *Nucl. Phys.* B34 (1971) 632–639, DOI: 10.1016/0550-3213(71)90351-8.

[11] D. V. Volkov and V. P. Akulov, "Is the Neutrino a Goldstone Particle?", *Phys. Lett.* B46 (1973) 109–110, DOI: 10.1016/0370-2693(73)90490-5.

[12] J. Wess and B. Zumino, "A Lagrangian Model Invariant Under Supergauge Transformations", *Phys. Lett.* B49 (1974) 52, DOI: 10.1016/0370-2693(74)90578-4.

[13] J. Wess and B. Zumino, "Supergauge Transformations in Four-Dimensions", *Nucl. Phys.* B70 (1974) 39–50, DOI: 10.1016/0550-3213(74)90355-1.

[14] "Search for Supersymmetry in Events with Large Missing Transverse Momentum, Jets, and at Least One Tau Lepton in 21 fb^{-1} of $\sqrt{s}$ = 8 TeV Proton-Proton Collision Data with the ATLAS Detector", tech. rep. ATLAS-CONF-2013-026, Geneva: CERN, 2013.

[15] "Search for electroweak production of supersymmetric particles in final states with at least two hadronically decaying taus and missing transverse momentum with the ATLAS detector in proton-proton collisions at $\sqrt{s}$ = 8 TeV", tech. rep. ATLAS-CONF-2013-028, Geneva: CERN, 2013.

[16] S. Glashow, "Partial Symmetries of Weak Interactions", *Nucl.Phys.* 22 (1961) 579–588, DOI: 10.1016/0029-5582(61)90469-2.

[17] S. Weinberg, "Elementary particle theory of composite particles", *Phys.Rev.* 130 (1963) 776–783, DOI: 10.1103/PhysRev.130.776.

[18] S. Weinberg, "A Model of Leptons", *Phys. Rev. Lett.* 19 (21 1967) 1264–1266, DOI: 10.1103/PhysRevLett.19.1264, URL: http://link.aps.org/doi/10.1103/PhysRevLett.19.1264.

[19] M. Boehler, "Exclusive search for supersymmetry with same-flavour di-lepton final states with the ATLAS detector" (2012).

[20] J. Beringer et al., "Review of Particle Physics (RPP)", *Phys.Rev.* D86 (2012) 010001, DOI: 10.1103/PhysRevD.86.010001.

[21] J. S. Schwinger, "On Quantum electrodynamics and the magnetic moment of the electron", *Phys.Rev.* 73 (1948) 416–417, DOI: 10.1103/PhysRev.73.416.

[22] R. Feynman, "Mathematical formulation of the quantum theory of electromagnetic interaction", *Phys.Rev.* 80 (1950) 440–457, DOI: 10.1103/PhysRev.80.440.

[23] A. Salam and J. C. Ward, "Weak and electromagnetic interactions", *Nuovo Cim.* 11 (1959) 568–577, DOI: 10.1007/BF02726525.

[24] S. Weinberg, "Implications of Dynamical Symmetry Breaking", *Phys. Rev.* D13 (1976) 974–996, DOI: 10.1103/PhysRevD.13.974.

[25] E. Gildener, "Gauge Symmetry Hierarchies", *Phys. Rev.* D14 (1976) 1667, DOI: 10.1103/PhysRevD.14.1667.

[26] S. Weinberg, "Implications of Dynamical Symmetry Breaking: An Addendum", *Phys. Rev.* D19 (1979) 1277–1280, DOI: 10.1103/PhysRevD.19.1277.

[27] L. Susskind, "Dynamics of Spontaneous Symmetry Breaking in the Weinberg- Salam Theory", *Phys. Rev.* D20 (1979) 2619–2625, DOI: 10.1103/PhysRevD.20.2619.

[28] S. P. Martin, "A Supersymmetry primer" (1997), arXiv: hep-ph/9709356 [hep-ph].

[29] S. Dimopoulos and H. Georgi, "Softly Broken Supersymmetry and SU(5)", *Nucl. Phys.* B193 (1981) 150, DOI: 10.1016/0550-3213(81)90522-8.

[30] E. Witten, "Dynamical Breaking of Supersymmetry", *Nucl. Phys.* B188 (1981) 513, DOI: 10.1016/0550-3213(81)90006-7.

[31] M. Dine, W. Fischler and M. Srednicki, "Supersymmetric Technicolor", *Nucl. Phys.* B189 (1981) 575–593, DOI: 10.1016/0550-3213(81)90582-4.

[32] S. Dimopoulos and S. Raby, "Supercolor", *Nucl. Phys.* B192 (1981) 353, DOI: 10.1016/0550-3213(81)90430-2.

[33] N. Sakai, "Naturalness in Supersymmetric Guts", *Zeit. Phys.* C11 (1981) 153, DOI: 10.1007/BF01573998.

[34] R. Kaul and P. Majumdar, "Cancellation of Quadratically Divergent Mass Corrections in Globally Supersymmetric Spontaneously Broken Gauge Theories", *Nucl. Phys.* B199 (1982) 36, DOI: 10.1016/0550-3213(82)90565-X.

[35] C. Bennett et al., "First year Wilkinson Microwave Anisotropy Probe (WMAP) observations: Preliminary maps and basic results", *Astrophys.J.Suppl.* 148 (2003) 1, DOI: 10.1086/377253, arXiv: astro-ph/0302207 [astro-ph].

[36] V. Trimble, "Existence and Nature of Dark Matter in the Universe", *Ann.Rev.Astron.Astrophys.* 25 (1987) 425–472, DOI: 10.1146/annurev.aa.25.090187.002233.

[37] H. Goldberg, "Constraint on the photino mass from cosmology", *Phys. Rev. Lett.* 50 (1983) 1419, DOI: 10.1103/PhysRevLett.50.1419.

[38] J. Ellis et al., "Supersymmetric relics from the big bang", *Nucl. Phys.* B238 (1984) 453–476, DOI: 10.1016/0550-3213(84)90461-9.

[39] N. Cabibbo, "Unitary Symmetry and Leptonic Decays", *Phys.Rev.Lett.* 10 (1963) 531–533, DOI: 10.1103/PhysRevLett.10.531.

[40] M. Kobayashi and T. Maskawa, "CP Violation in the Renormalizable Theory of Weak Interaction", *Prog.Theor.Phys.* 49 (1973) 652–657, DOI: 10.1143/PTP.49.652.

[41] H. P. Nilles, "Supersymmetry, Supergravity and Particle Physics", *Phys.Rept.* 110 (1984) 1–162, DOI: 10.1016/0370-1573(84)90008-5.

[42] H. E. Haber and G. L. Kane, "The Search for Supersymmetry: Probing Physics Beyond the Standard Model", *Phys.Rept.* 117 (1985) 75–263, DOI: 10.1016/0370-1573(85)90051-1.

[43] P. Fayet, "Supersymmetry and Weak, Electromagnetic and Strong Interactions", *Phys. Lett.* B64 (1976) 159, DOI: 10.1016/0370-2693(76)90319-1.

[44] P. Fayet, "Spontaneously Broken Supersymmetric Theories of Weak, Electromagnetic and Strong Interactions", *Phys. Lett.* B69 (1977) 489, DOI: 10.1016/0370-2693(77)90852-8.

[45] G. R. Farrar and P. Fayet, "Phenomenology of the Production, Decay, and Detection of New Hadronic States Associated with Supersymmetry", *Phys. Lett.* B76 (1978) 575–579, DOI: 10.1016/0370-2693(78)90858-4.

[46] P. Fayet, "Relations Between the Masses of the Superpartners of Leptons and Quarks, the Goldstino Couplings and the Neutral Currents", *Phys. Lett.* B84 (1979) 416, DOI: 10.1016/0370-2693(79)91229-2.

[47] M. Mazur et al., "Search for supersymmetry with jets, missing transverse momentum, and two or more taus at sqrt(s)=7 TeV : Support note for 2011 analysis", tech. rep. ATL-PHYS-INT-2012-024, Geneva: CERN, 2012.

[48] G. Aad et al., "The ATLAS Experiment at the CERN Large Hadron Collider", *JINST* 3 (2008) S08003, DOI: 10.1088/1748-0221/3/08/S08003.

[49] L. Evans and P. Bryant, "LHC Machine", *JINST* 3 (2008), ed. by L. Evans S08001, DOI: 10.1088/1748-0221/3/08/S08001.

[50] T. A. collaboration, *ATLAS photos*, CTAN: http://www.atlas.ch/photos/, 2013.

[51] M. Aharrouche et al., "Energy linearity and resolution of the ATLAS electromagnetic barrel calorimeter in an electron test-beam", *Nucl.Instrum.Meth.* A568 (2006) 601–623, DOI: 10.1016/j.nima.2006.07.053, arXiv: physics/0608012 [physics].

[52] "ATLAS muon spectrometer: Technical design report" (1997).

[53] "ATLAS first level trigger: Technical design report" (1998).

[54] "ATLAS high-level trigger, data acquisition and controls: Technical design report" (2003).

[55] J. Frost, "Commissioning of ATLAS data quality infrastructure with first collision data", *J.Phys.Conf.Ser.* 331 (2011) 032009, DOI: 10.1088/1742-6596/331/3/032009.

[56] G. Aad et al., "Electron performance measurements with the ATLAS detector using the 2010 LHC proton-proton collision data", *Eur.Phys.J.* C72 (2012) 1909, DOI: 10.1140/epjc/s10052-012-1909-1, arXiv: 1110.3174 [hep-ex].

[57] "Muon reconstruction efficiency in reprocessed 2010 LHC proton-proton collision data recorded with the ATLAS detector" (2011).

[58] W. Lampl et al., "Calorimeter clustering algorithms: Description and performance" (2008).

[59] M. Cacciari, G. P. Salam and G. Soyez, "The Anti-k(t) jet clustering algorithm", *JHEP* 0804 (2008) 063, DOI: 10.1088/1126-6708/2008/04/063, arXiv: 0802.1189 [hep-ph].

[60] G. Aad et al., "Expected Performance of the ATLAS Experiment - Detector, Trigger and Physics" (2009), arXiv: 0901.0512 [hep-ex].

[61] "Jet energy scale and its systematic uncertainty in proton-proton collisions at sqrt(s)=7 TeV in ATLAS 2010 data" (2011).

[62] "Identification of the Hadronic Decays of Tau Leptons in 2012 Data with the ATLAS Detector", tech. rep. ATLAS-CONF-2013-064, Geneva: CERN, 2013.

[63] "Performance of the Reconstruction and Identification of Hadronic Tau Decays in ATLAS with 2011 Data" (2012).

[64] "Determination of the tau energy scale and the associated systematic uncertainty in proton-proton collisions at $\sqrt{s} = 8$ TeV with the ATLAS detector at the LHC in 2012", tech. rep. ATLAS-CONF-2013-044, Geneva: CERN, 2013.

[65] M. Dobbs et al., "Les Houches guidebook to Monte Carlo generators for hadron collider physics" (2004) 411–459, arXiv: hep-ph/0403045 [hep-ph].

[66] G. Corcella et al., "HERWIG 6: An Event generator for hadron emission reactions with interfering gluons (including supersymmetric processes)", *JHEP* 0101 (2001) 010, DOI: 10.1088/1126-6708/2001/01/010, arXiv: hep-ph/0011363 [hep-ph].

[67] M. Asai, "Geant4-a simulation toolkit", *Trans.Amer.Nucl.Soc.* 95 (2006) 757.

[68] G. Cowan et al., "Asymptotic formulae for likelihood-based tests of new physics", *Eur.Phys.J.* C71 (2011) 1554, DOI: 10.1140/epjc/s10052-011-1554-0, arXiv: 1007.1727 [physics.data-an].

[69] J. Neyman and E. S. Pearson,
"On the Problem of the Most Efficient Tests of Statistical Hypotheses", English,
Philosophical Transactions of the Royal Society of London. Series A, Containing Papers of a Mathematical or Physical Character 231 (1933) pp. 289–337, ISSN: 02643952,
URL: http://www.jstor.org/stable/91247.

[70] M. Drees, R. M. Godbole and P. Roy, *Theory and Phenomenology of Sparticles*,
World Scientific Publishing Co, Pre. Ltd., 2004.

[71] LEPSUSYWG, ALEPH, DELPHI, L3 and OPAL experiments, *note LEPSUSYWG/01-03.1* (),
URL: http://lepsusy.web.cern.ch/lepsusy/Welcome.html.

[72] A. Heister et al., "Absolute mass lower limit for the lightest neutralino of the MSSM from e+ e- data at s**(1/2) up to 209-GeV", *Phys.Lett.* B583 (2004) 247–263,
DOI: 10.1016/j.physletb.2003.12.066.

[73] J. Abdallah et al., "Searches for supersymmetric particles in e+ e- collisions up to 208-GeV and interpretation of the results within the MSSM", *Eur.Phys.J.* C31 (2003) 421–479,
DOI: 10.1140/epjc/s2003-01355-5, arXiv: hep-ex/0311019 [hep-ex].

[74] M. Acciarri et al., "Search for charginos and neutralinos in e^+e^- collisions at $\sqrt{S}$ = 189-GeV", *Phys.Lett.* B472 (2000) 420–433, DOI: 10.1016/S0370-2693(99)01388-X,
arXiv: hep-ex/9910007 [hep-ex].

[75] G. Abbiendi et al.,
"Search for chargino and neutralino production at s**(1/2) = 192-GeV to 209 GeV at LEP",
Eur.Phys.J. C35 (2004) 1–20, DOI: 10.1140/epjc/s2004-01758-8,
arXiv: hep-ex/0401026 [hep-ex].

[76] C. Collaboration, "Observation of a new boson with a mass near 125 GeV" (2012).

[77] G. Aad et al., "Observation of a new particle in the search for the Standard Model Higgs boson with the ATLAS detector at the LHC", *Phys.Lett.* B716 (2012) 1–29,
DOI: 10.1016/j.physletb.2012.08.020, arXiv: 1207.7214 [hep-ex].

[78] S Amoroso et al., "Search for direct production of the top squark in the all-hadronic ttbar + etmiss final state in 21 fb-1 of p-pcollisions at sqrt(s)=8 TeV with the ATLAS detector",
tech. rep. ATLAS-COM-CONF-2013-011, Geneva: CERN, 2013.

[79] M Barisonzi et al.,
"Search for direct top squark pair production in final states with one isolated lepton, jets, and missing transverse momentum in $sqrts$ = 8,TeV pp collisions using 21 fb^{-1} of ATLAS data",
tech. rep. ATLAS-COM-CONF-2013-038, Geneva: CERN, 2013.

[80] A. Collaboration,
"Search for direct stop pair production in events with a Z boson, b-jets and missing transverse energy with the ATLAS detector using 21 fb^{-1} from proton-proton collision at $\sqrt{s}$ = 8 TeV",
tech. rep. ATLAS-COM-CONF-2013-021, Geneva: CERN, 2013.

[81] S. Schael et al., "Branching ratios and spectral functions of tau decays: Final ALEPH measurements and physics implications", *Phys.Rept.* 421 (2005) 191–284,
DOI: 10.1016/j.physrep.2005.06.007, arXiv: hep-ex/0506072 [hep-ex].

[82] Y Bai et al., "Searching for direct gaugino production and direct slepton production with two hadronic taus and missing transverse momentum at sqrts=8TeV.",
tech. rep. ATL-COM-PHYS-2012-1809, Geneva: CERN, 2012.

[83] C. Lester and D. Summers,
"Measuring masses of semiinvisibly decaying particles pair produced at hadron colliders",
Phys.Lett. B463 (1999) 99–103, DOI: 10.1016/S0370-2693(99)00945-4,
arXiv: hep-ph/9906349 [hep-ph].

[84] A. Barr, C. Lester and P. Stephens, "m(T2): The Truth behind the glamour",
J.Phys. G29 (2003) 2343–2363, DOI: 10.1088/0954-3899/29/10/304,
arXiv: hep-ph/0304226 [hep-ph].

[85] P. Bechtle et al., "Search for Events with Large Missing Transverse Momentum, Jets, and Leptons (e/mu/tau) in 8 TeV Proton-Proton Collision Data with the ATLAS Detector",
tech. rep. ATL-COM-PHYS-2012-1738, Geneva: CERN, 2012.

List of Figures

List of Tables